STUDY OF THREE DIMENSIONAL GERMANIUM ISLANDS AND ULTRATHIN Si_xGe_{1-x} FILMS GROWN BY CHEMICAL VAPOUR DEPOSITION ON Si(111)-(7×7)

Selvi Gopalakrishnan
M.Sci. Stud. (U. of Newcastle, Aust.), B.Sc. (NUS, Singapore)

A thesis submitted to fulfil the requirements for the award of the degree

Dr. rer. nat.

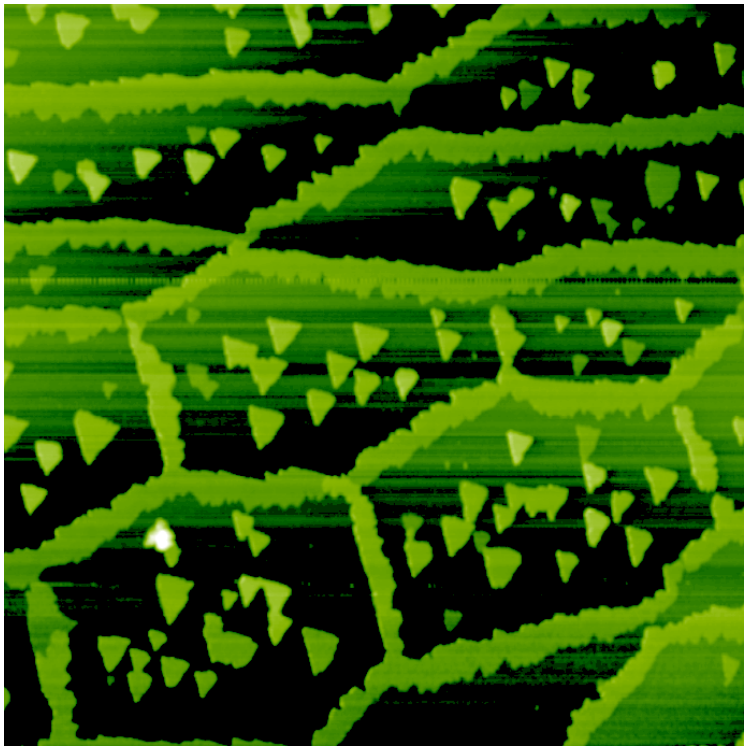

Department of Surface Chemistry and Catalysis
University of Ulm, Germany

July 2005

Fac quod aequum est
non quod facile est

Dean of the Faculty of Science : Prof. Dr. Klaus-Dieter Spindler

1st Examiner : Prof. Dr. R.J. Behm
2nd Examiner : Prof. Dr. N. Hüsing

Date of Submission : July 2005

Declaration

I hereby certify that the work embodied in this thesis is the result of original research and has not been submitted for a higher degree to any other University or Instituition.

Selvi Gopalakrishnan

Acknowledgement

This thesis could not have been completed without the assistance and encouragement of a number of people and I would be forever indebted to them.

Firstly, I would like to thank Prof. Dr. R.J. Behm for giving me the opportunity to carry the research towards my PhD in his department and for his support during my stay in Germany and PD. Dr. H. Rauscher for supervising my research and for all his timely comments with regards to the thesis. I would also like to thank Prof. Dr. N. Hüsing from the Department of Solidstate Chemistry who has kindly consented to be the second examiner of this thesis and Prof. Dr. G. Groß from the Department of Molecular Botanics and Prof. Dr. M. Pietralla from the Department of Experimental Physics for graciously consenting to be members of the panel of examiners for my final examination to fulfil the requirements for the award of the degree Dr. rer. nat.

A special thanks to Dr. Harry Hoster for his help in the setting up and installation of the PCI 6024 E interface card and for writing the labview program for the computer controlled reconstruction program which ensured that I had a nearly perfect Si(111)-(7×7) surface for every experiment .

I would like to say a big thank you to both Thomas Häring from the mechanical workshop and Gerd Braith from the electrical workshop, without whose assistance nothing in the basement laboratory would have worked the way it was supposed to, Verena Botzenhart who is not only an all around good person but also one of the best secretaries whom I had the pleasure of knowing and also to all my co-workers past and present, who have lent a helping hand (or two) whenever I needed it .

I would also like to thank Klaus Seemann, who carried out his Studienarbeit in this department, during which we carried out most of the experiments described in Chapter 5 of this thesis.

I would like to acknowledge the Graduate College GRK 328 at the University of Ulm for providing me with the funds to carry out my research for the first three years of my stay here.

Finally, I would like to acknowledge the friendship and support of friends and former colleagues past and present from Siltronic (formerly Wacker Siltronic), Burghausen, Portland (Oregon) and Singapore.

ABSTRACT

This work probed at the atomic level, processes that occur during the Ge three dimensional island formation and on ultrathin Si_xGe_{1-x} epitaxial growth by chemical vapour deposition on the Si(111)-(7×7) substrate with the aid of surface probe techniques such as STM and AFM, XPS, as well as TEM imaging of any 3D island formation.

This work could essentially be divided into two parts. The first part studied the growth of the strained Ge on Si system with emphasis on the characterisation of the CVD grown three dimensional germanium islands on a standard Si(111)-(7×7) substrate as well as on a surface modified Si(111)-(7×7) substrate. The characterisation was carried out using a combination of techniques. XPS was used to calculate the effective coverages of deposited germanium, the STM was used to image the top most layers whenever possible and AFM, cross-sectional TEM and HRTEM to image the three dimensional islands. The possible causes of the surface modification were also examined.

In the second part of this work the growth morphologies ultrathin Si_xGe_{1-x} layers grown on the Si(111)-(7×7) substrate at 750 K where the hydrogen desorption rate from the Si(111) surface is low and at 850 K which was the temperature at which the rate of hydrogen desorption from the Si(111) surface was a maximum were investigated. In addition modelling of ultrathin layer growth was carried out using two existing growth models.

Table of Contents

Chapter 1 : Introduction **1**

Chapter 2 : Literature Review **6**
2.1 Introduction 6

2.2 Surface Reconstruction 6
2.2.1 Introduction 6
2.2.2 Definitions 6
2.2.3 Principles of Semiconductor Surface Reconstructions 7
2.2.4 Si(111) – (7×7) DAS Structure 7

2.3 Epitaxy 9
2.3.1 Introduction 9
2.3.2 Epitaxial Growth modes 10
2.3.3 Chemical Vapour Deposition 11
2.3.3.1 Introduction 11
2.3.3.2 Mechanism of CVD 11
2.3.3.3 Kinetics of thin layer CVD 12
2.3.4 SiGe Epitaxy 13
2.3.4.1 Ge on Si[100] 13
2.3.4.2 Ge on Si(111) 14
2.3.4.3 Si_xGe_{1-x} epitaxial growth on silicon 15

Chapter 3 : Experimental Procedure **17**
3.1 Introduction 17

3.2 X-Ray Photoelectron Spectroscopy 19
3.2.1 Introduction 19
3.2.2 Theory 19
3.2.2.1 Process of photoelectron and Auger electron emission 19
3.2.2.2 Koopman's Approximation 21
3.2.2.3 Spin Orbit Splitting 21
3.2.2.4 Chemical Shift 21
3.2.3 Instrumentation 22
3.2.3.1 Introduction 22
3.2.3.2 Vacuum Requirements 22
3.2.3.3 X-ray Source 22

3.2.3.4 Electron Energy Analyser 24
3.2.3.5 Detector 25
3.2.4 Data Processing 26

3.3 Scanning Tunnelling Microscopy 27
3.3.1 Introduction 27
3.3.2 Theory of tunnelling 27
3.3.2.1 Time independent elastic tunnelling through a one dimensional rectangular potential barrier 27
3.3.2.2 Perturbation Theory of STM - Tersoff Haman Model 30
3.3.3 Instrumentation 32

3.4 Sample Preparation 33
3.4.1 Storage and Handling 33
3.4.2 Standard Si(111) – (7×7) sample 34
3.4.2.1 Clean Si(111) sample 34
3.4.2.2 Reconstruction from Si(111) – (2×1) to (7×7) 34
3.4.3 Standard Ge(111) – (1×1) sample 35
3.4.3.1 Clean Ge(111) sample 36
3.4.4 Chemical Vapour Deposition 36
3.4.4.1 Preparation of the precursor gas supply lines 36
3.4.4.2 CVD Procedure 36

Chapter 4 : Characterisation of Ge structures grown by CVD on standard and XPS exposed Si(111) – (7×7) surfaces 37

4.1 Introduction 37

4.2 Characterisation of 3D Ge growth by CVD on standard and irradiated Si(111) – (7×7) by STM and AFM 37
4.2.1 Experimental Procedure 37
4.2.2 Results 38
4.2.3 Discussion 44

4.3 TEM Characterisation of 3D Ge growth by CVD Si(111)-(7×7) 45
4.3.1 Introduction 45
4.3.2 Sample Preparation 46
4.3.3 Results 46
4.3.4 Discussion 50

4.4 Summary 51

Chapter 5 : Identification of the causes of XPS induced 3D growth of Ge on Si(111) –(7×7) 53

5.1 Introduction 53

5.2 Photoluminescence Experiments 53
5.2.1 Introduction 53
5.2.2 Preparation of samples for PL measurements 54
5.2.3 Results 54
5.2.4 Discussion 55

5.3 Shielding 55
5.3.1 Introduction 55
5.3.2 Experimental Procedure 55
5.3.3 Results 57
5.3.4 Discussion 57

5.4 Offset Exposure 57
5.4.1 Introduction 57
5.4.2 Experimental Procedure 57
5.4.3 Results 58
5.4.4 Discussion 58

5.5 QMS of the Outgassing from the XPS 58
5.5.1 Introduction 58
5.5.2 Experimental Procedure 59
5.5.3 Results 59
5.5.4 Discussion 59

5.6 GeH_4 CVD at Ambient Temperature 60
5.6.1 Introduction 60
5.6.2 Experimental Procedure 60
5.6.3 Results 60
5.6.4 Discussion 61

5.7 Hydrogen Exposure Prior to GeH_4 CVD 62
5.7.1 Introduction 62
5.7.2 Experimental Procedure 62
5.7.3 Results 62
5.7.4 Discussion 63

5.8 Summary 63

Chapter 6 : STM/XPS studies of ultrathin Si_xGe_{1-x} films grown on Si(111)-(7×7) by CVD **65**

6.1 Introduction 65

6.2 Experimental Procedure 66

6.3 Results and Discussion 66
6.3.1 Calculation of coverage 66
6.3.2 Sticking Coefficients 68
6.3.3 Topography : Effect of Temperature and terrace width 69
6.3.4 Island Growth at 750 K 71
6.3.5 Island growth at 850K 73
6.3.6 Deposition Profiles 76
6.3.7 Description of two models of Si_xGe_{1-x} film growth by CVD 77
6.3.8 Fitting of experimental data to models 83

6.4 Summary 87

Chapter 7 : Summary **88**

References **90**

Appendix 1 : Computer Controlled Reconstruction and STM Data Conversion **97**

Appendix 2 : Vacuum Requirements and Pressure measurements **100**

Chapter 1

Introduction

The age of solid state electronics was ushered in with Bardeen and Brattain's[1] discovery of voltage and power gain in a point contact transistor at Bell Laboratories. Since the first fledging prototype ICs were developed in Fairchild[2] in 1959, the complexity and density of today's semiconductor chip have been increased from SSI (small scale integration) to ULSI (ultra large scale integration), where there are 10^7 or more components per chip. This has been achieved by shrinking the feature size to far less than 1 μm for the ULSI circuits.

The dominant material used for the fabrication of the IC is silicon. Commercial hyperpure monocrystalline silicon for chip manufacturing is grown by either Float-zone (FZ) or Czochralski (CZ) methods. Due to the differences in the growth methods, the FZ silicon crystal has a higher purity than the CZ silicon crystal. Oxygen impurities[3] in CZ crystals were known to be of the order 10^{18} atoms/cm^3 compared to less than 10^{16} atoms/cm^3 for the FZ crystal. Hence, higher resistivities are obtained with the FZ crystal, because of its greater purity. Therefore, the FZ crystals are mostly used in the manufacture of high power devices and infra-red radiation sensors. The higher levels of the oxygen impurity in the CZ crystal gives it more mechanical strength, making it less subject to thermal stresses experienced during wafer processing and hence, it is used for other IC fabrications.

The silicon crystal belongs to the cubic crystal system and has the diamond structure. As electronic, mechanical, as well as chemical and physical properties of crystalline materials depend on the orientation of the crystal[4], the chip fabrication processes are sensitive to the orientation of the crystallographic planes of the substrate. In silicon, the most important of these are the {100}, {110} and the {111}. For most applications, wafers with the {100} orientation are preferred to the other orientations because of various factors such as better crystal growth rates, radial dopant distribution, surface state density and epi-pattern displacement[3]. However, the wafers with the {111} orientation have the best crystallographic quality and mechanical strength among the three orientations, and are traditionally used as substrates in the fabrication of bipolar transistors and as alloy junction devices[3].

Although silicon is now the material of choice in the manufacture of the majority of the devices, germanium was initially utilized in the manufacture of the solid-state electronic devices[5]. However, silicon replaced germanium as the material of choice for two main reasons. The narrow bandgap of 0.66 eV limits the use of germanium devices to temperatures of about 90°C due to large leakage currents at higher temperatures. In contrast, silicon devices can be operated up to 200°C[4] as a result of the wider bandgap (1.12 eV) of silicon. The

second reason for the preference of silicon over germanium is the ability to provide a good passivation layer. Germanium oxide (GeO_2) is water soluble and dissociates at 800^oC[6] whereas silicon dioxide (SiO_2) is a stable oxide which forms a protective coating to the underlying devices. This stability has been used to advantage in current silicon based device fabrications. There are two main disadvantages with using silicon for device fabrication – its low electron hole mobility and its indirect bandgap.

The band gap is the energy difference between the bottom of the conduction band and the top of the valence band. In semiconductors the band gap is either direct or indirect and this depends on the band structure. In a direct band gap the valence band maximum is located directly beneath the conduction band minimum in momentum space (i.e. same k-vector) . An example of a semiconductor with a direct band gap is gallium arsenide. A material where the minimum energy in the conduction band is shifted by a k-vector in the momentum space is said to have an indirect band gap. The k-vector is determined by the crystal structure of the material. In materials with an indirect band gap, the electrons that are present in the conduction band are located in the energy minimum of that band. As the typical incoming photons have insufficient momentum to bridge the offset band and hence enable the electron to fall into the valence band, the electrons are not readily emitted from the conduction band via the mechanism of radiative recombination. These electrons then recombine through other less efficient means and hence the re-combination process is relatively slow.

The above mentioned disadvantages limit the use of silicon in certain applications like optoelectronic devices. However, through band gap engineering Si_xGe_{1-x} layers containing between 4% to 10% of germanium can be epitaxially grown on a silicon substrate whereby increasing the electron hole mobility and tailoring the bandgap as per the requirements of the design of the device. This has opened up new areas of applications for silicon based devices as Hetero Bipolar Transistors (HBTs) , LEDs, lasers and infra-red sensors.

The incorporation of germanium into silicon is carried out by growing a thin film of either germanium or a silicon germanium mixed layer on the crystal structure of the silicon substrate. This process is known as epitaxy. The two most common ways in which epitaxy is carried out are chemical vapour deposition (CVD) and molecular beam epitaxy (MBE). In MBE, this is done by creating localised atomic or molecular beams of the deposition material (Ge or Si and Ge), which impinges onto the heated surface of the crystalline substrate. The heated substrate ensures that there is sufficient thermal energy for the arriving atoms to migrate over the surface to the lattice sites. In CVD, the reactant gases which are often diluted by hydrogen are delivered over the surface of the heated substrate where they simultaneously undergo a number of reactions at the surface, which are more fully described in Chapter 2 of this work. Typical gas pressures used in CVD range from several mbars (high pressure CVD) to 10^{-5} mbars (low pressure CVD)[7].

MBE allows the precise control of the composition during the growth process. This has allowed not only valuable insight about the epitaxial growth process but has also enabled the production of structures such as quantum well devices and superlattices[8]. This in turn has fueled the interest in MBE as a research tool. The other advantage of MBE is that unlike the CVD process, the growth rate and the substrate temperature can mainly be chosen independently. As a result the MBE process can be enabled at a lower temperature regime as compared to the CVD process. The lower temperature growth enables the possibility of growing very thin epitaxial layers, as well as graded profiles with no relaxation and steep doping profiles. In addition, there is no boron (dopant) segregation at the low temperature regime. These advantages translate into a great flexibility in terms of process control as well

as flexibility in the design of the device. The main disadvantages of MBE is that in this process particle densities are much higher and hence, the process needs to be operated under UHV conditions to avoid problems with contamination. In addition, the small throughput of one wafer per run makes the MBE process less attractive among device manufacturers, in comparison to the CVD process.

In CVD, precursor gases such as Si_2H_6 (disilane) and GeH_4 (germane), are delivered into the reaction chamber at ambient temperature. When these precursor gases pass over the heated substrate, adsorption, pyrolysis and desorption processes successively occur, leading to a formation of a thin film. Although the CVD process is more complex as compared to the MBE process and the precursor gases used in the CVD process are either toxic, explosive or both, its attractiveness lies in the fact that epitaxy via CVD produces uniform films over a large surface area. This also enables dopant species to be introduced during epitaxy and thus producing uniformly doped silicon layers[9]. These factors combined with a low production cost and high throughput as well as ease of process scalability of new modules as compared to MBE, has made CVD a great favourite in the industry.

Although CVD is widely used, the process is more complex than that of MBE. Various factors influence the complex growth process, which include the flux of the incoming precursor gas, the type of precursor gas, the deposition temperature and the type of substrate itself[10]. A combination of these processes lead to complexities in the deposition mechanism whereby deposition is often a multi step process involving intermediate reactive species in the gas phase and on the substrate. As the precursor gases used are hydrated species and as hydrogen is often used as a carrier gas, the pyrolysis and the desorption of hydrogen from the substrate surface becomes very important at the low temperature regimes which are used for the growth of very thin epitaxial layers. As the hydrogen desorption rate is a function of the substrate temperature, low growth rates are characteristic for epitaxial growth at the low temperature regime via CVD.

This work probes the atomic level processes occuring at the surface of the Si(111) during Ge or ultrathin SiGe epitaxial growth by CVD, with the aid of surface probe techniques such as STM and AFM, XPS, as well as TEM imaging of any 3D island formation. This work can essentially be divided into two parts. The first part studies the growth of the strained Ge on Si system with emphasis on the characterisation of the CVD grown three dimensional germanium islands on a standard Si(111)-(7×7) substrate as well as on a surface modified Si(111)-(7×7) substrate. The possible causes of the surface modification are also examined. The second part of this work concentrated on the growth kinetics and modelling of ultrathin Si_xGe_{1-x} layers grown on the Si(111)-(7×7) substrate.

In the following chapter, the principles of reconstruction, with emphasis on the reconstruction of the Si(111)-(7×7) are introduced. This is followed by a description of the three different epitaxial growth modes. The principles of chemical vapour deposition are outlined in the next section. This chapter concludes with a review of Ge on Si and SiGe on Si epitaxy.

The next chapter introduces the experimental techniques used in this work. The theory behind the experimental techniques such as the XPS and the STM is discussed followed by a discussion of the equipment used and the operational procedure. This is followed by a discussion of the sample surface preparation which includes the cleaning of the substrate, followed by the reconstruction parameters and concludes with the procedure for the chemical vapour deposition.

In Chapter 4, the results of the characterisation of the germanium 3D islands on the Si(111)-(7×7) surface which had been modified after the exposure to the XPS are presented. These are compared with the Ge 3D islands grown on a standard Si(111)-(7×7) which is a surface without any modification. The surfaces were characterised using the STM, while the structures were characterised by AFM, TEM. In addition, HR-TEM was carried out on the cross-sections of the islands. In the previous work carried out by J. Braun[11,12], it was suggested that the Ge growth on the standard Si(111)-(7×7) surface proceed in a layer by layer growth mode under certain CVD conditions and reaches a saturation point after 2.5 BL, while surface irradiation by X-rays changes the growth mode to a Stranski-Krastanov growth mode under the same CVD conditions, whereby no saturation in the growth is reached. It was hypothesized by J. Braun[11,12] that the difference was due to the formation of C_s/C_i defects on the irradiated substrate, which released the stress arising from the 4% lattice mismatch between Si and Ge, thereby promoting the Ge 3D growth.

In this work the irradiated surface was re-examined for the C_s/C_i defects via Pholuminescence Spectroscopy. However, no evidence of these defects could be found on substrates which had been irradiated by the XPS. Moreover, in continuation to the earlier work by J.Braun, it is found that 3D Ge island formation occurs in the standard Si(111)-(7×7) substrate after the formation of the initial wetting layer (2 to 2.5 BL). However, there were marked differences in the growth morphology of the Ge islands grown on the two different substrates and these were characterised by the methods stated above.

The reason for the difference in growth morphology of the Ge 3D islands grown on the standard and the irradiated Si(111)-(7×7) substrates is examined in Chapter 5. One of the decisive experiments carried out involved irradiating only half of the substrate to XPS by use of a molybdenum shield, followed by chemical vapour deposition of germanium on the whole substrate. The results of this experiment together with the STM investigation of the atomically resolved surfaces of the standard and the irradiated substrates yielded valuable clues to the reasons behind the surface modification of the irradiated substrate. These experiments led to other follow up experiments involving the XPS as well as the QMS, in addition to the AFM which was used to characterise the surface after deposition. These experiments enabled the elucidation of a cause of the surface modification after irradiation of the Si(111)-(7×7) which led to a change in the growth morphology of the Ge 3D islands which were subsequently grown on that surface.

The growth of ultrathin SiGe layers on the Si(111)-(7×7), grown using low gas deposition pressures under UHV conditions, was investigated in Chapter 6. This chapter can be split into two parts. The first part presents the results of the investigation of the growth morphology of the ultrathin Si_xGe_{1-x} layer at two different temperatures. In the earlier work by J. Braun[12,13], where sticking coefficients were investigated at a constant deposition over a range of temperatures (400 K to 760 K) for two different gas mixtures, it was established that there was a low temperature (below 600 K) regime where heteroepitaxial growth was self limiting due to the high surface coverage by the hydrated species and a high temperature regime (above 730 K) where the growth is continuous due to the desorption from hydrogen from the surface of both silicon and germanium. This work attempts to fill in the topographical information gap by investigating the growth morphologies at 750 K where the hydrogen desorption rate from the Si(111) surface is low and at 850 K which is the temperature at which the rate of hydrogen desorption from the Si(111) surface is a maximum.

In the second part of Chapter 6, two existing models for CVD growth of Si_xGe_{1-x} layers are discussed. The data from the above experiments are then used to model the CVD growth

profile of the ultrathin Si_xGe_{1-x} layers using the two models. In addition the data from the previous work by M. Holz[14] was also used to model the CVD growth profiles. As both models use different assumptions in their formulation, the results of the modeling of the experimental data yielded different information on the growth of ultrathin Si_xGe_{1-x} layers via CVD. One model assumes steady state concentrations of the activated silicon and germanium complexes while the other takes into account the interactions of the oncoming reactants with the alloy on the surface. Hence, information on the germane decomposition rate or on the interaction of the activated species with the alloy on the surface is obtained.

The last chapter of this work summarizes the findings from the work carried out on Ge on Si(111) and SiGe on Si(111) epitaxial growth via CVD. There are two appendices included in this dissertation.. The first documents the temperature controlled reconstruction cycle using labview which was newly installed for this work, as well as the STM data processing. The second appendix documents the vacuum and pressure requirements for the work carried out.

Chapter 2

Review of Surface Reconstruction and Epitaxy on silicon surfaces

2.1 Introduction

In this study several terms and concepts are referred to frequently. The definition of frequently used terms as well as a review of the important concepts will be presented in this chapter. This review chapter is essentially divided into two parts. The first part introduces the idea of surfaces, surface reconstruction and the structure of the Si(111)-(7×7). The second part of the review concentrates on epitaxy and highlights the three different types of growth mode and then focuses on CVD and on Si, Ge and SiGe epitaxy.

2.2 Surface Reconstruction

2.2.1 Introduction

The process of reconstruction is mostly prevalent in semiconductors but it also occurs with less stable metal surfaces. The process involves the relativeley large atomic scale displacement of surface atoms which leads to changes in periodicity of the lattice and often also in changes of symmetry. These changes can be detected by in-situ surface diffraction techniques like RHEED, LEED and other techniques like the STM.

2.2.2 Definitions

A surface is defined to be either the topmost (atomic) layer that is in contact with its environment or several atomic layers[15] in the near surface region (or from the topmost layer).
A dangling bond is created when a normal bond containing two spin paired electrons is ‘cut’ during the creation of a surface, leaving a bond which contains less than the two spin paired electrons. Adatoms are atoms deposited at random sites on the surface during epitaxy.

A structure is an arrangement of atoms in space. Structures range from 1 nm to the sub-micrometer range. Morphology is defined to be the form or shape of the surface and hence a macroscopic property. The topography of a surface is its profile is terms of peaks, valleys and planes.

2.2.3 Principles of Semiconductor Surface Reconstruction

A semiconductor surface is usually created by cleaving a single crystal along its natural cleavage plane. Such surfaces are often energetically unfavourable because of positive free energy arising from the dangling bonds which were formed during the creation of the surface. So, in order to minimise this free energy there is a need to reduce the exposed surface area and hence the surface either reconstructs or relaxes. The process surface reconstruction or relaxation in order to achieve a surface with a minimal free energy, can be explained by the principles described by Duke[16].

Principle 1 : *Surfaces are reconstructed by saturating the dangling bonds.*
This occurs when unpaired electrons in neighbouring dangling bonds are paired when one atom donates the electron in its dangling bond to a pair with the electron in the dangling bond of the neighbouring atom. In this process, the first atom which has lost its electron, relaxes towards the bulk, while the second atom which now has fully spin paired electrons is pushed away from the bulk. This may lead to re-hybridisation of the dangling bonds[17].

Principle 2 : *Surface energies (mostly in quasi 1D cases) can be lowered by atomic relaxations leading to semiconducting instead of metallic surface states.*

Principle 3 : *The observed surface structure will have the lowest free energy that is kinetically possible under the preparation conditions.*

Principle 4 : *The reconstructed or relaxed surfaces will be electrically uncharged.*

Principle 5 : *The atomic geometry of a surface for a given (surface) stoichiometry is determined by the lowering of the surface state bands.*

The first three principles are usually useful to explain the surface reconstruction of elemental semiconductors while Principles 4 and 5 are primarily applicable to compound semiconductors. The application of these principles will be demonstrated in the succeeding section on the Si(111) cleavage and reconstruction to the (7×7) DAS structure.

2.2.4 Si(111)-(7×7) DAS Structure

Semiconductors such as Si and Ge have the diamond structure shown in Fig. 2.1. The cleavage of a Si(111) single crystal occurs through the the middle of the covalent bond that points along the [111] direction[17]. The new sp^3 orbital has only one electron per surface atom (dangling bond). The (1×1) structure thus formed has half-occupied surface bands and is metallic in nature. However, rehybridization (Principle 1) of the dangling bonds occurs and with a reduction of symmetry, the surface is converted to the metastable semiconducting (2×1) structure (Principles 2 & 3). Annealing this surface in UHV at a temperature of 603 K causes the surface to reconstruct to a (5×5)[18] structure. Further heating to 873 K converts the surface to a (7×7) DAS structure[18]. Further annealing at a temperature of 1123 K causes surface disorder. Depending on the surface preparation, other surface structures such as the (9×9) and the $(\sqrt{3}\times\sqrt{3})R30^{o}$[18] (which have only be found in patches) are also formed.

The Si(111)-(7×7) has the lowest free energy among the known structures of the Si(111) surface. The generally accepted model of the structure is the Dimer-Adatom-Stacking fault (DAS) model shown in Fig. 2.2. This model was proposed based on the TEM data by Takayanagi et. al.[19] and subsequently verified by other diffraction techniques and by STM. In

comparison to the (2×1) structure, the (7×7) DAS structure is calculated[20,21] to be lower in energy by 0.06 eV per 1×1 unit cell.

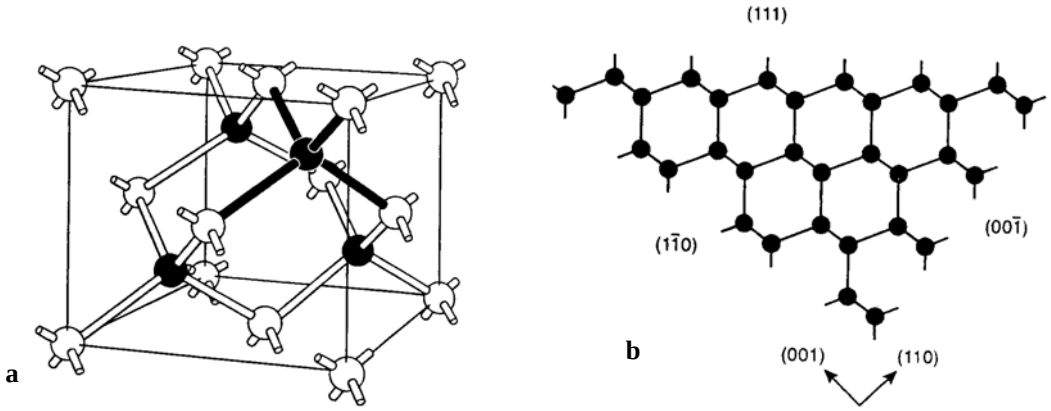

Fig. 2.1: Diamond Structure (a) ball and stick model of diamond atomic gepmetry (b) plane view of diamond structure semiconductor normal to a (111) plane. The lines at the surface (top) indicate the dangling bonds associated with a bulk surface[16]

In the DAS (dimer-adatom-stacking fault) model of the unit cell of the Si(111)-(7×7) structure extends over 4 layers with a stacking fault present on half of unit (faulted half). The 3rd layer from top designated as the dimer layer contains 9 Si dimers on the edges of unit cell halves. In the 2nd layer (rest atom layer) there are 36 dangling bonds saturated by 12 Si adatoms. Each of these adatoms has one dangling (unsaturated) bond. There are 6 dangling bonds in the rest atom layer which are unsaturated. A stacking fault is present between rest atom layer and dimer layer in one half of (7×7) unit (faulted half). The 4th layer has one dangling bond at the bottom of the corner holes. In total the structure has 102 atoms. Each (7×7) unit cell has 12 adatoms in the adatom layer, 42 atoms in the rest atom layer and 48 atoms in the dimer layer. Of these atoms only 19 of them are the most active as they have dangling bonds and they can be divided into 6 different groups of chemically active atoms : 6 corner adatoms in the faulted half and 6 in the unfaulted half nearest to deep corner holes, the 3 centre adatoms in the faulted and unfaulted halves closer to centre, the 6 rest atoms and 1 unsaturated atom in the corner hole (corner hole atom) which is located deeper than other rest atoms.

The surface of the Si(111)-(7×7) structure was found to be metallic[16,17] by surface electronic exitation spectra. Although this appears to contradict Principle 2, in reality this non-conformance of this principle is allowed for non 1D systems. In the DAS model for the (7×7) structure, the driving force of the reconstruction is the reduction of the number of dangling bonds (Principle 1) at the expense of the gain in surface energy through the formation of stacking faults, corner holes and the domains separating the faulted and unfaulted halves. However, for Si(111)-(7×7) this trade-off results in a structure which has the lowest free energy among all the other known structures for the Si(111) surface (Principle 3). As not all the dangling bonds on the Si(111) surface are removed during the reconstruction process, the resulting surface state was found to be metallic.

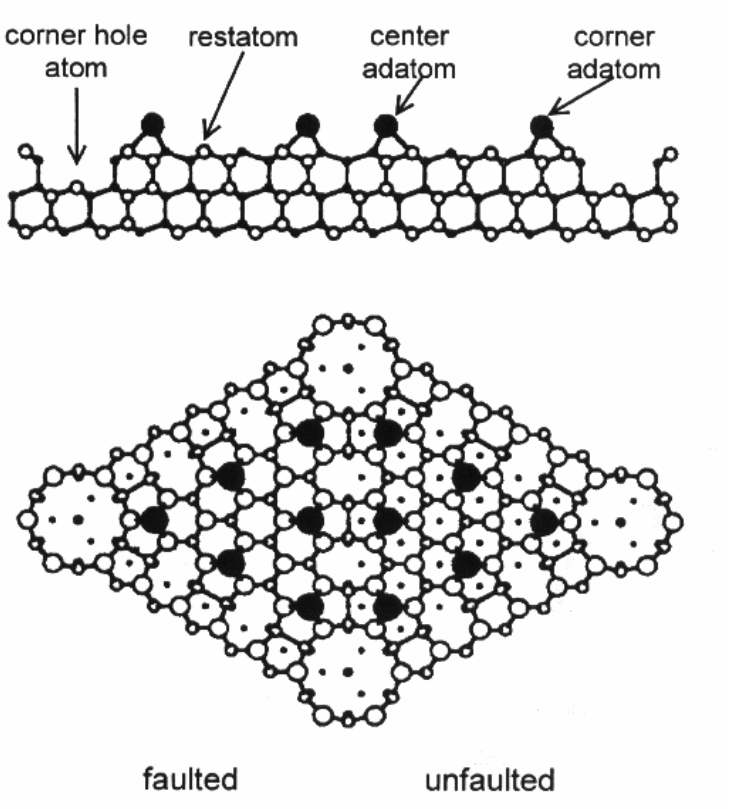

Fig. 2.2 : DAS Structure of Si(111) – (7×7)

For the Ge(111) surface, with a lattice constant which is about 4% larger, the cost in energy by the formation of stacking faults and corner holes becomes too large and instead only the formation of adatoms with the removal of dangling bonds results (Principle 1), leading to the c(2×8) structure. In the case of the formation of Ge or SiGe thin films by epitaxy on the Si(111) surface, strain arising form the lattice mismatch between Si and Ge adds to the cost of the formation of stacking faults and corner holes. This is offset by the gain in energy by the formation of domain walls. Hence, stress induced domains of mixed structures such as (7×7), (5×5) and ($\sqrt{3}\times\sqrt{3}$)R30^{o} are formed[18].

2.3 Epitaxy

2.3.1 Introduction

Thin films are defined to be near surface regions from a few hundred Angstroms up to 1 μm. Thin films have huge technological importance in solid state electronics and a wide variety of preparation techniques are available. These techniques are classified according to film formation environment : Electrolysis, vacuum, plasma, liquid phase epitaxy, solid phase epitaxy and chemical vapour deposition. In this chapter, epitaxial growth and in particular epitaxial growth by chemical vapour deposition will be covered.

2.3.2 Epitaxial Growth modes

In 1985 Ernst Bauer[22] had classified epitaxial film growth into three different growth modes. The Frank-van der Merwe[23] (Fig. 2.3a) or the layer by layer growth where the the atoms of the deposited material are more strongly attracted to the the surface of the substrate than to each other, the Vollmer-Weber growth[24] (Fig. 2.3b), where the atoms of the deposited material are more strongly attracted to each other than to the substrate, which results in discrete island growth and the Stranski-Krastanov growth[25] (Fig 2.3c), an intermediate between the previous two growth modes where the initial growth is layer by layer resulting in a wetting layer and the subsequent growth is via discrete island formation. All three growth modes have been experimentally observed, the Frank-van der Merwe growth mode in Au on Ag[27], the Vollmer-Weber growth mode in Au on molybdenite[28] and the Stranski-Krastanov growth mode in InAs on GaAs[29]. In general, the most common growth mode is the SK growth mode.

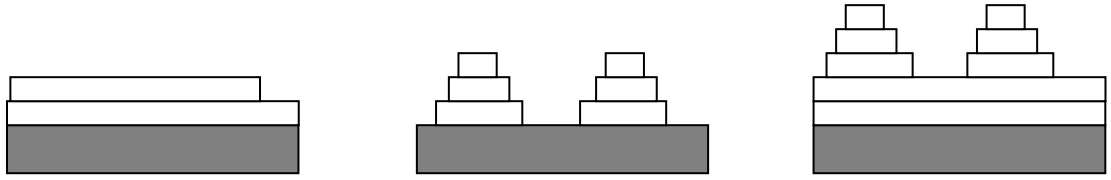

a b c

Fig. 2.3 : Epitaxial Growth Modes : (a) Frank-van der Merwe(FM) (b) Vollmer-Weber (VW) (c) Stranki-Krastanov (SK)

The dynamics[21] of film growth of a species A on a substrate B with the assumption of equlibrium between the components of the film on the surface and the gas phase is given by the relation :

$$\Delta\gamma = \gamma_A + \gamma_i - \gamma_B \qquad 2.1$$

where γ_A and γ_B are the surface free energies of A and B respectively and is γ_i the interfacial free energy. The interfacial free energy is dependent on the strain and on the chemical interactions between the reactant and the substrate at the interface. From the above relation, in order for FM growth to occur,

$$\Delta\gamma = \gamma_A + \gamma_i - \gamma_B \leq 0 \qquad 2.2$$

i.e. the sum of the interfacial energy and the sum of film surface energy must be less than the surface energy of the substrate. When this condition is satisfied, wetting occurs. However, strain due to factors such as lattice mismatch between the film and the substrate, increases with the increasing number of layers grown and as strain is a function of the interfacial energy, there is a corresponding increase in γ_i. At a critical thickness when the sum of $\gamma_A + \gamma_i$ is greater than the surface energy of the substrate, γ_B, the growth mode changes from the layer by layer growth mode to the Stranski-Krastanov growth mode. This results in the formation of 3D islands on a 2D wetting layer. A good example of this growth mode is the formation of 3D Ge islands on a 2BL thick Ge wetting layer on the Si(111) substrate. However, in the case

where γ_A is much larger than γ_B or when there is little or no lattice mismatch and weak chemical interaction at the interface between the film and the substrate i.e. $\gamma_i \cong 0$, then nucleation of 3D island results, leading to the VW growth mode. To get around this problem, the substrate could be pre-wetted using surfactants, which lower the high substrate surface energy.

2.3.3 Chemical Vapour Deposition

2.3.3.1 Introduction

In chemical vapour deposition, film formation on the substrate proceeds via the activation energy produced from the chemical reaction of the precursor gases. In CVD, the properties of the film and the deposition rate are affected by the choice of precursor gases and their purity, the ratio of precursor gases (in a mixed gas system), the gas flow rate (pressure), the geometry of the reaction chamber, the preparation of the surface of the substrate and the temperature of the substrate . The main advantages of epitaxy by CVD lies in the fact that the films produced are uniform, reproducible and precisely controlled. In addition, the deposition process via CVD is facilitated by the ease of handling and process scalability. The main disadvantage with this technique is that the precursor gases used are either toxic, inflammable or corrosive, relatively high temperatures are often required to actuate the process.

2.3.3.2 Mechanism of CVD

The CVD process is usually considered to be a heterogeneous process as it occurs as a reaction in an adsorbed layer on the surface of the substrate and the growing film. There are eight stages (Fig. 2.4) in the formation of film growth via CVD[21]. They are as follows:

1. Transport of the precursor gases to the vicinity of the surface of the substrate.
2. Diffusion of the precursors to the substrate surface.
3. Adsorbtion of the reactive species onto the surface of the substrate.
4. Surface chemical reaction
5. Surface migration and lattice incorporation
6. Desorption of reaction product
7. Diffusion of reaction products away from the surface of the substrate
8. Transport of the reaction products away from the deposition zone.

These steps occur simultaneously and under steady state conditions, all of them proceed at the same rate. However, under under non steady state conditions, the slowest of the above steps would be the rate determining step. The CVD control process is classified as mass transport of the first kind (equilibrium controlled process), mass transport of the second kind (diffusion controlled process) and as surface kinetics, depending on the rate determining step of the CVD process. The first type of mass transport occurs when Step 1 or 8, ie. the precursor gas flow into deposition zone or the removal of reactant products from the deposition zone is the slowest step. The second type of mass transport occurs when the transfer of the precursors or the reactant products between the gas stream and the surface of the substrate (Step 2 or 7) is the rate determining step. The last type of CVD control process occurs when either adsorption (Step 3), chemical reaction (Step 4), surface migration and lattice incorporation (Step 5) or desorption (Step 6) is the rate determining step. When surface concentrations are close to equilibrium at high temperature or low flow rates the growth rates of the films can be calculated from the values of the equlibrium partial pressure of all the species. The rate of film growth via CVD at medium total gas flow rates and high temperatures is determined by

diffusion in the gaseous phase. At high temperatures and or at high gas flow rates, the CVD process is predominantly controlled by surface kinetics. In general, the control step is usually composed of both mass transport and surface kinetics. However, it is common for one mechanism to predominate.

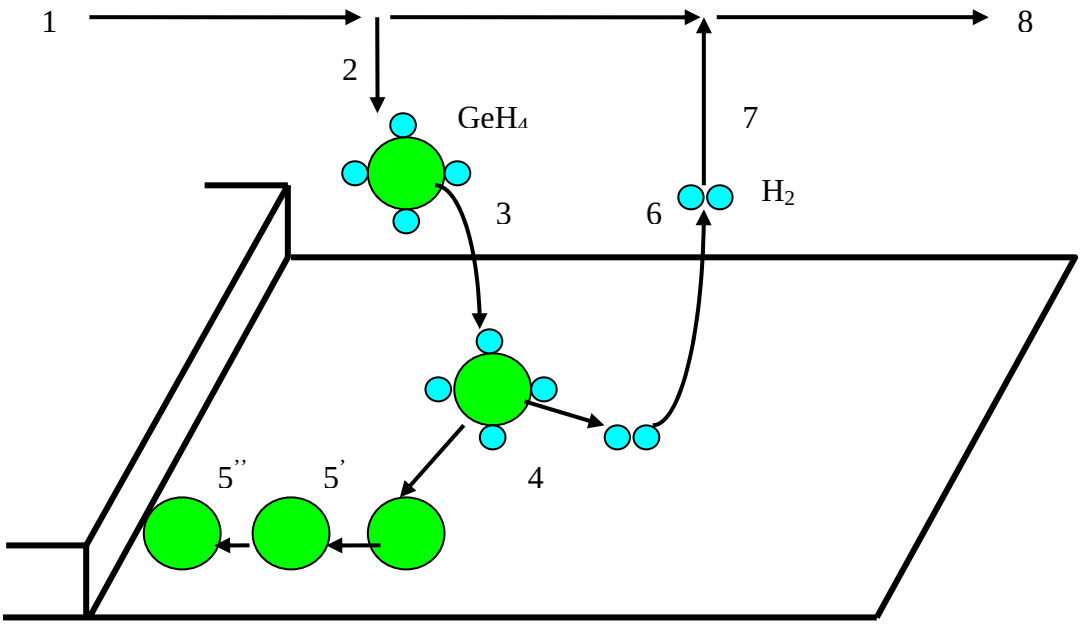

Fig. 2.4 : Steps of the CVD process with GeH_4 as the precursor gas

2.3.3.3 Kinetics of thin layer CVD

For a reaction of the form,

$$XY(g) + Z(g) \rightarrow X(s) + YZ(g) \qquad 2.3$$

the rate of deposition of a species can be calculated from the thickness of the deposited layer (h) for a particular deposition time (t) and is as follows:

$$R_d = \frac{h}{t} \qquad 2.4$$

For a first order heterogeneous reaction of the type shown in eq. 2.3, the rate constant (k) is given by:

$$k = \frac{R_d}{X^0} \qquad 2.5$$

where X^0 is the mole fraction of the main reactant in the gas mixture. From the Arrhenius equation, the rate constant is expressed as follows:

$$k = A\, e^{\left[\frac{-E}{RT}\right]} \qquad 2.6$$

where A is the pre-exponential factor, E is the activation energy, R is the gas constant and T is the absolute temperature. Hence, the kinetic equation of the deposition rate is written as follows:

$$R_d = A\, e^{\left[\frac{-E}{RT}\right]} X^0 \qquad 2.7$$

The activation energy and the pre-exponential can be obtained from a plot of log k vs 1/T (derived from eq. 2.6), where the value of E is obtained from the slope of the straight line and A from the intercept at the y-axis.

2.3.4 SiGe Epitaxy

Heteroepitaxial growth of Ge or the Si_xGe_{1-x} alloy on the silicon substrate can be achieved by MBE or CVD. In the former the material to be deposited is brought into contact with the substrate surface in its elemental form while the latter process involves the adsorption and decomposition of precursor gases (usually hydrated or chlorinated) on the substrate surface, followed by the desorption of the gaseous by-products from the surface as described in the previous section. This section gives an overview of some of the work carried out using both of these processes.

2.3.4.1 Ge on Si[100]

This has been extensively[30-34] studied due to technological importance of the Si[100] surface. In the case of MBE grown Ge on the Si(001) substrate, the initial wetting layer is strained and consists of the $(2\times N)$ reconstruction which is a periodic array of the (2×1) reconstruction with every N^{th} dimer missing[30]. This produces a periodic array of trenches which partially reduce the strain caused by the Ge-Si lattice mismatch, by the outward relaxation of germanium near the trenches. However, the formation of trenches leads to an increase in the formation energy of the film. These two opposing forces, determine the periodicity ofthe reconstruction. In-situ STM imaging during MBE growth carried out by B.Voigtländer's group[30] showed that the distance between the trenches , ie. the periodicity N of the $(2\times N)$ reconstruction decreased with increasing coverage. This was hypothesised[30] to be due to the increasing strain energy due to the increasing Ge coverage which could not be compensated by the energy of trench formation which should not change as a function of coverage. When the stress could not be further relieved by the dimer vacancy lines, trenches are formed along the rows, ie. perpendicular to the $(2\times N)$ trenches[31,32]. This occurs beyond 2ML.

The Ge wetting layer grown by CVD on the Si(001) surface using silane as a precursor gas[30] shows a similar behaviour to the wetting layers growth by MBE. However, the wetting layers grown by CVD have been observed to be strongly dependent on temperature, with thicknesses ranging from about 4 ML at 620 K to about 9 ML at 700 K[32]. In contrast the wetting layers of MBE grown Ge films are in the 3-4 ML range[33]. This temperature dependent wetting layer growth in the CVD process has been attributed to the influence of hydrogen which acts as a surfactant promoting the layer by layer growth.

After the formation of the two dimensional wetting layer, the Ge 3D island growth is initiated. In the case of Ge on Si(001), the structures have been observed to form clusters of 'huts'. These 'huts' have been reported to form near defects such as pits or at step edges[34]. In the in-situ STM imaging during the Ge on Si(001) growth by CVD carried out by B.Voigtländer's group[30], the pits were observed to nucleate from from existing defects which were in most cases voids formed from the agglomoration of the missing dimers. The nucleation of the 'hut' cluster was observed to form in the close proximity of these pits. A similar nucleation pattern was observed in the MBE grown Ge 'hut' cluster. This has been ascribed to the greater elastic relaxation energy for a 3D island nucleating at close proximity to a pit, which increases with pit size. Hence the pits are prefered sites for nucleation of the Ge 3D islands. The initial hut clusters have a square base. However, with increasing island size, the islands become elongated in order to accomodate the increasing stress.

2.3.4.2 Ge on Si(111)

STM studies on Ge films grown on Si(111)-(7×7), carried out by Wintterlin and Avouris[34] showed differences in the surface structures present on the germanium films grown by CVD and by MBE. The CVD grown films also showed different structures at different temperatures.

In the Ge films grown by MBE at 370°C and 430°C, a mixture of domains consisting of (7×7) and (5×5) DAS structures was observed[34]. In contrast, in the CVD process, Ge film growth at 370°C is via monolayer growth of the hydrogen stabilised (1×1) structure[34]. As the hydrogen desorption maximum from the Si(111) surface lies at 540°C, it is expected that at 370°C some hydrogen atoms resulting from the decomposition of germane would occupy the vacant dangling bond sites and would impede Ge adsorption at these sites. On top of the hydrogen covered monolayers, individual adatoms which were not bonded to any hydrogen atom, were adsorbed resulting in the hydrogen stabilised (1×1) structure. In addition, at this temperature, the substrate surface was observed to be etched selectively at the centre adatoms of the (7×7) DAS structure. It has been deduced[34] that this was due to "chemically induced intermixing" between silicon and germanium.

CVD films of Ge grown at 430°C, were observed to have not only the mixed domains of (7×7) and (5×5) DAS structures seen on MBE film grown at the same temperature but also patches of the $\left(\sqrt{3}\times\sqrt{3}\right)R30^{0}$ structure which had not been seen on the MBE grown Ge films.. Due to the relatively low surface hydrogen coverage at this temperature the (1×1) structure is not formed. Instead transient hydrated species GeH and SiH which are trivalent like the Gp III elements such as Al and Ga are formed. The hydrated species adsorb as adatoms onto the Si(111), thus saturating dangling bonds giving rise to the $\left(\sqrt{3}\times\sqrt{3}\right)R30^{0}$ structure which is similar to structures formed by the Gp III elements on Si(111). The $\left(\sqrt{3}\times\sqrt{3}\right)R30^{0}$ germanium structure on Si(111) was found to be relatively stable even after the desorption of hydrogen. However, this structure was observed to partially transform at about 600°C and to full (7×7) reconstruction at higher temperatures[34].

Studies in Motta`s group[7] and by Kamins et. al[35] have reported that with MBE, the nucleation of the Ge 3D island starts at a coverage between 3 and 5 ML and is a function of the incoming Ge flux and the temperature of the substrate. The initial islands formed were pyramidal which morph to a truncated tetrahedral in order to release strain. The (5×5) DAS structure was observed on the wetting layer and the strain released (7×7) DAS structure has been observed on the top surface of the truncated tetrahedral. With further island growth the

strain is released by formation of facets at the sides, eventually leading to a more rounded structure. At this trench (erosion) formation around the edges of islands was noted. The final stage of the island formation resulted in a hole in the centre of the island. This structure has been dubbed as an `atoll` structure due to its resemblance to the geological structure of that name. These structures have only been observed on Si(111) substrates.

2.3.4.3 Si_xGe_{1-x} epitaxial growth on silicon

In recent years there has been widespread interest in Si_xGe_{1-x} epitaxy on silicon as band gap engineering had opened the way for the incorporation of epitaxially grown Si_xGe_{1-x} heterostructures into existing silicon device architectures. The epitaxial layers have been mainly grown by either MBE or UHV-CVD.

In gas-source molecular beam epitaxy and CVD, gaseous hydrides of Ge and hydrated or chlorinated Si precuursor gases were used. However, the growth mechanism of the Si_xGe_{1-x} alloy from the precursor gases has not been precisely understood.

Previous work carried out on the Si_xGe_{1-x} epitaxial growth reported a monotonic increase in growth rate with increasing germane flow in the hydrogen-dicholorosilane-germane mixed gas system[36] while others reported that in the silane/germane[37-40] or disilane/germane[41] mixed gas systems the rate increases until a certain Ge fraction after which there is a decrease in the alloy growth rate. The increase in growth rate had been attributed to the enhanced desorption of hydrogen[37] or chlorine[42] which was catalysed by the presence of germanium atoms at the silicon surface

Studies by Kim et. al.[37] on the Si(100) substrate over a range of alloys with different germanium compositions, have classified the growth rate into the high and low temperature ranges. In the high temperature region of 600-700°C, the growth rate peaked at a certain Ge fraction. The peak occured at a low Ge fraction in agreement with other studies by Jang and Rief[38,39] and Robbins[40] et. al. However, in the low temperature range of 300-500°C, were reported to increase with increasing germanium composition with an enhanced increase in the growth rate observed at the higher end of the low temperature range. This increase was attributed to the increase in the desorption rate of surface hydrogen at increasing temperature and germanium fraction. Hence, it had been proposed that at this range the rate limiting step is the hydrogen desorption process. This supports the idea that the growth rate is limited by the number of available free adsorption sites, $(1-\theta_H)$.

In recent studies, J. Braun et. al.[12,13] have studied the growth of the Si_xGe_{1-x} alloy on Si(111) by CVD using STM and XPS. In their study they had used a GeH_4/Si_2H_6 mixed gas system using two different gas mixtures and depositing over a temperature range of 400- 760 K. Their results also indicated a low and high temperature regime. In the low temperature regime of less than 600 K, the surfaces were reported to have been coverd with hydrides and the growth was described to be self-limiting. However, it was reported that the surface structures were dependent on the composition of the gas mixtures, where the hydrogen coverage was observed to be lower with depostion with the gas mixture with the higher germanium content.

At the high temperature range of greater than 730 K, the surface was observed to be free of hydrogen and the structures were reported to be similar to those observed on silicon homoepitaxy for both gas mixtures. Comparison of sticking coefficients of the individual gased in the mixture to that of the pure gases indicated that for disilane, the sticking coefficient was smaller than observed in the pure gas while the sticking coefficient of germane was observed to be greater in the mixture when compared to the pure gas. These differences were attributed to strain effects in the Si_xGe_{1-x} layer.

Chapter 3

Experimental Techniques

3.1 Introduction

All the experiments, with the exception of AFM (ex-situ in air), PL (Dept. of Semiconductor Physics, University of Ulm) and TEM (Centre for Electron Microscopies, University of Ulm), for this work have been carried out in the UHV system, designated as STM V (Fig. 3.1). The system is equipped with a home-made beetle STM, a Fisons XPS with a twin anode source, a QMS and an Er-LEED (Fig. 3.2), which can be exchanged with a spinning rotor gauge (Appendix 2). The system also comes with a loadlock at the rear of the system, which is used to introduce samples and STM tips, without venting the entire system. The base pressure of the main chamber is 1.0×10^{-10} mbar or better. This is achieved by a combination of pumps, described in Appendix. 2. The pressures in the load lock and the main chamber are measured by individual ion gauges (refer to Appendix 2). The precursor gases are delivered via stainless steel gas lines, which have been cleaned by flushing with nitrogen, is then pumped via a turbo pump while being baked out. The precursor gases are introduced into the main chamber through a stainless steel capillary line positioned in close proximity to the sample. The gas flux is controlled by a precision leak valve. For mixed gas epitaxy, the precursor gases are mixed in a mixing chamber prior to their introduction into the main chamber. The correct mix ratio is achieved by measuring the individual gas flow into the mixing chamber with the aid of a Baratron. The cleanliness of the system and the gases introduced into the system is monitored by the QMS.

The sample transfer to and from the loadlock, the various sample stages, XPS manipulator and the wehnelt is carried out using the wobblestick. To transfer the sample to the STM, the removable sample stage (Fig. 3.2) is first moved into position (via the wobblestick) over the STM. The sample holder (containing the sample) is then picked up by a vertical T-shaped STM manipulator which is then used to place the sample holder in the STM.

The preparation (reconstruction or CVD) is carried out at the wehnelt. The sample is heated at the unpolished (backside) side of the sample by emission of electrons from a heated filament within the wehnelt. The filament in the wehnelt is constructed from a 0.2 mm thoria coated tungsten wire. All other wires that constitute the set up for heating, i.e. the internal connections to high voltage supply, wehnelt and filament controls are made from 0.5 mm tantalum wires. All the internal wires used in the wehnelt construct are encased in ceramic tubings.

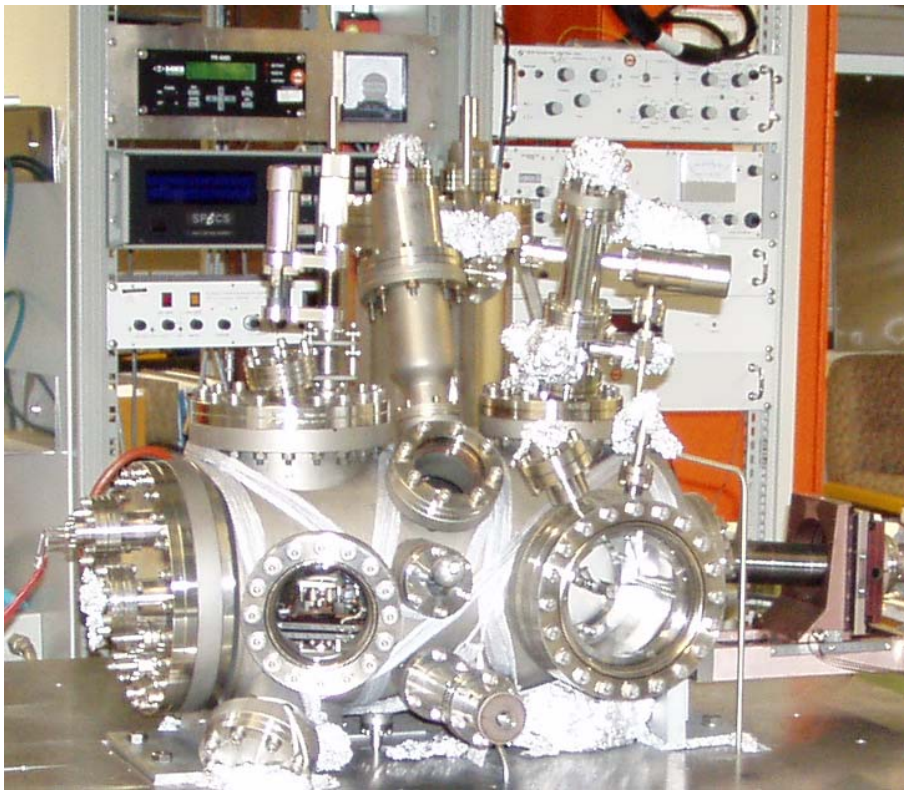

Fig. 3.1 : STM V

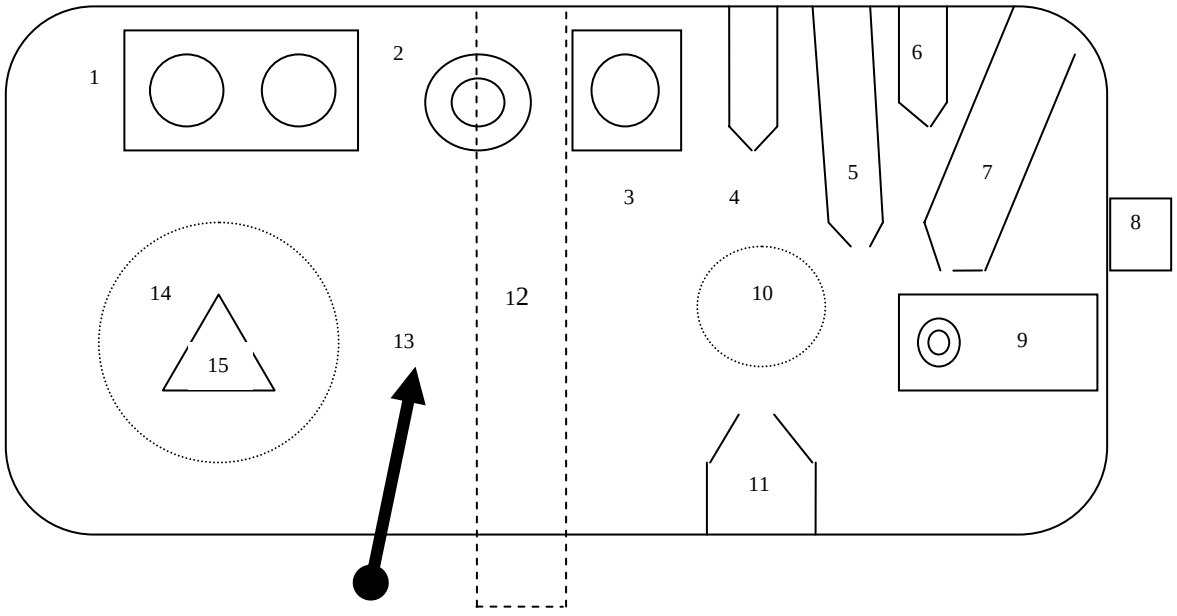

LEGEND :

1 : Spare Sample Stage,	6 : Ion Gauge,	11 : LEED or SRG,
2 : Wehnelt,	7 : XPS Twin Anode,	12 : Load lock manipulator,
3 : Removable Sample Stage,	8 : XPS Ion pump,	13 : Wobble stick,
4 : QMS,	9 : XPS manipulator,	14 : Exit to turbo/diffusion pumps,
5 : XPS Clam 2,	10 : Exit to ion pump/TSP,	15 : Beetle STM

Fig. 3.2 : Internal (top view) layout of STM V

3.2 X-Ray Photoelectron Spectroscopy (XPS)

3.2.1 Introduction

To obtain information on the composition of the surface, methods utilising the sensitivities of low energy electrons or which use electrons as the source or as the detected particles are used. These surface sensitive techniques are collectively known as electron spectroscopies. In XPS soft X-rays are used to bombard the surface. Hence the XPS spectrum of a sample consists of not only the photoelectrons from the intital bombardment and the Auger electrons which are emitted in a secondary process, but also features associated with inelastic scattering.

3.2.2 Theory

3.2.2.1 Process of photoelectron and Auger electron emission

As seen from Fig. 3.1, when soft X-rays bombard the surface of a solid sample, an electron from the core levels is emitted only if the energy of the initial photon is greater than the sum of the binding energy and and the workfunction. The excess energy (eq. 3.3) is carried off by the emitted photoelectron as kinetic energy.

$$E_{K.E.} = h\nu - E_{B.E.} - \Phi \qquad 3.1$$

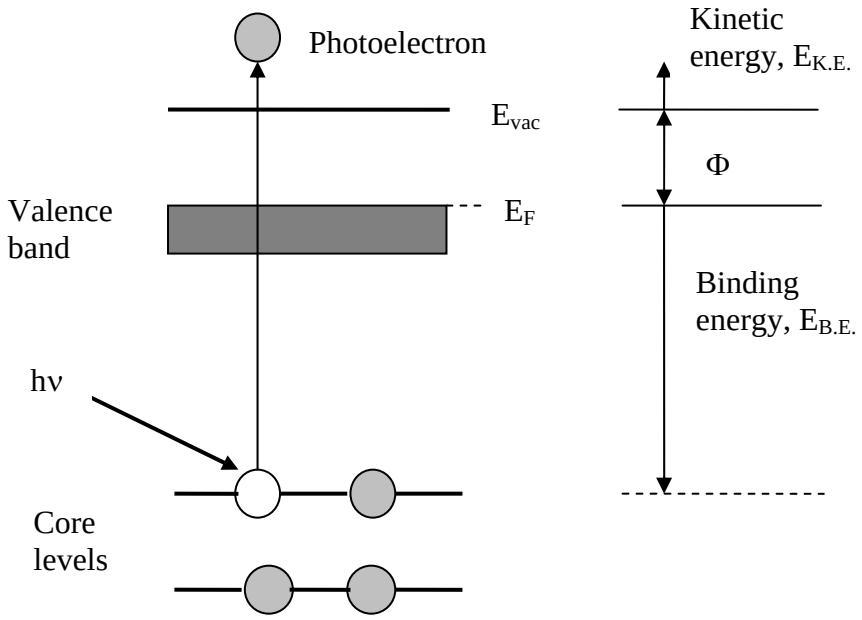

Fig. 3.3 Schematic diagram of the process of emission of a photoelectron

With the emission of the photoelectron, there is now a 'hole' in a core level. As illustrated in Fig. 3.4, a decay occurs whereby an electron from an upper level drops into the vacancy in the core level. The excess energy gained from this decay from this process is released either via X-ray Fluorescence as a photon (XRF) or as in Fig. 3.3 be used to eject an Auger electron from the same or a different level, whereby a doubly ionized final state is reached. The kinetic energy E_A, of the Auger electron is therefore given by,

$$E_A = (E_{L1} - E_K) - E^*_{L2,3} - \Phi \qquad 3.2$$

X-ray fluorescence is more probable for elements with a high atomic number that have a deep core hole (high B.E.). For elements with an atomic number of less than 15, the alternate Auger process is more probable. From the above equation it can be seen that unlike the photoelectrons emitted in the primary process, the kinetic energy of the Auger electron is independent of the initial energy of the X-ray photon. Hence, if the XPS spectra taken with different anodes (Al and Mg) are plotted on a kinetic energy scale for the same material, the peaks associated with the Auger electrons will be fixed while those for the photoelectrons will shift relative to the incident photon energy.

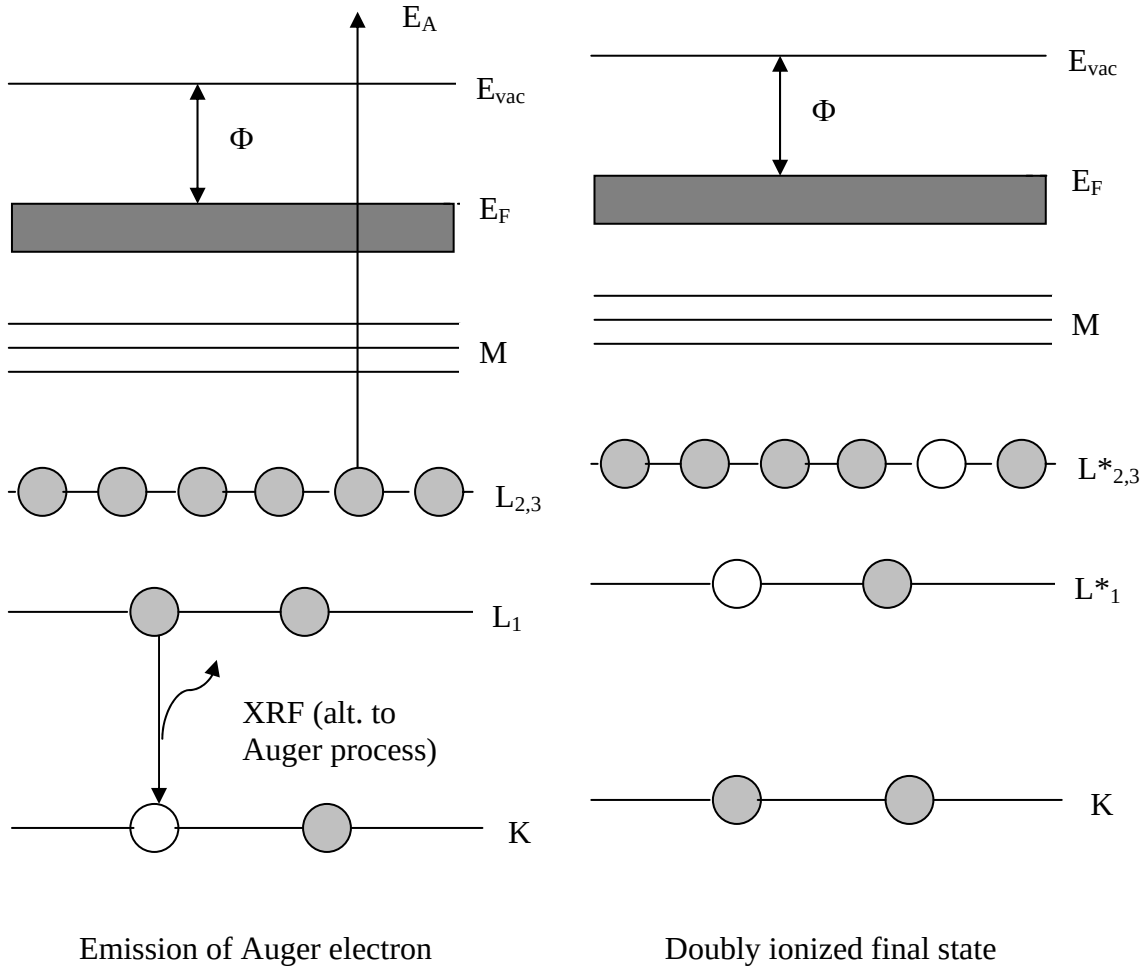

Fig. 3.4 Schematic diagram of the process of the emission of the Auger electron

As the Auger process illustrated in Fig. 3.4 involves the K shell and the L shells, the Auger electron from this process is designated the $KL_1L_{2,3}$ electron. This involves the initial decay from a core shell. Other possible Auger processes involve LMM and the LLM shells. The latter process is also known as the Coster-Kronig process and is extremely fast as the initial decay occurs within the same shell. This process is favoured for the initial decay of core holes with low angular momentum quantum numbers (eg. 2s, 3s, 4p, 3s, etc). However, these transitions are usually not observed as the kinetic energy from these transitions is low.

3.2.2.2 Koopman's Approximation

In Koopman's theorem, the Binding Energy (Fig. 3.3) of an electron is the difference in energy between the initial state (neutral atom with n electrons) and the final state (ionized atom with n-1 electrons and one ejected photoelectron). However, Koopman's energy is not observed as the relaxation process that occurs with the photoemission is not taken into account.

3.2.2.3 Spin Orbit Splitting

Spin orbit splitting occurs when the orbital angular momentum of an electron couples with its spin angular moment. This results in the formation of doublet peaks for all orbitals except for the s-orbitals.

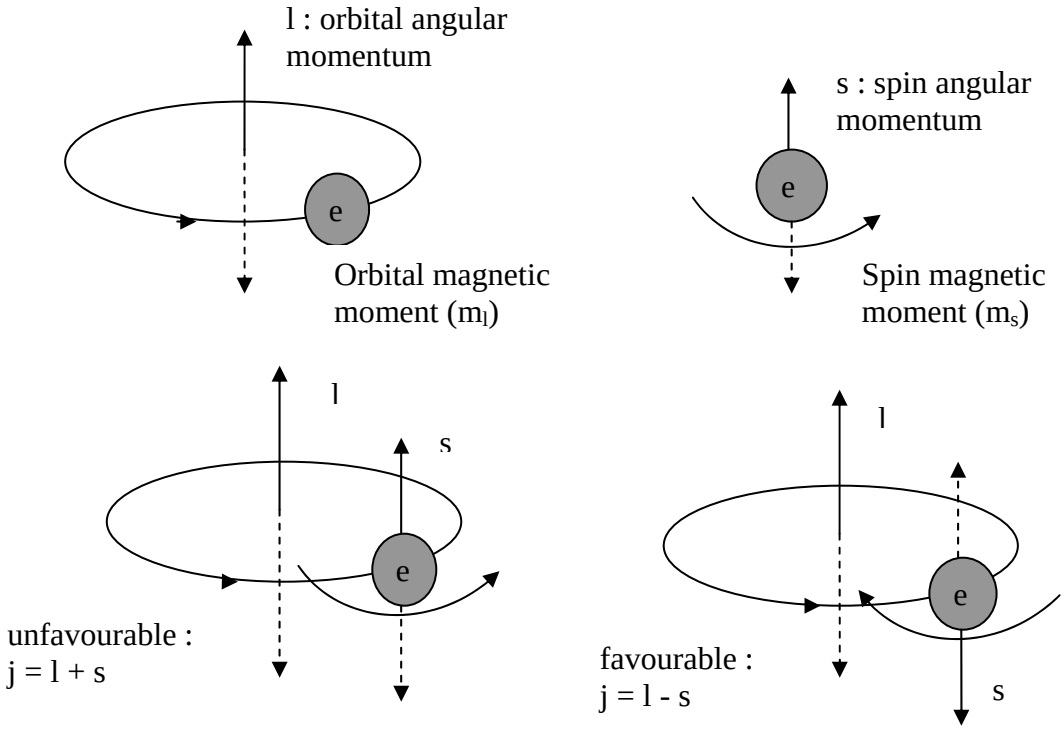

Fig 3.5 : Spin Orbit Coupling

3.2.2.4 Chemical Shift

When a species is present as a compound and not as an element, not only is the peak of the species observed but the peak associated with the charged species is also observed. This difference is known as the chemical shift. As the chemical shift is associated with the overall charge on the atom, a reduction of charge leads to an increase in the binding energy of the atom (shielding effect). Hence the magnitude of the shift from neutral atom depends on the number of substituents, the electronegativity of the substituents and the oxidation state. This feature combined with the surface sensitivity, makes XPS an attractive tool for chemical analysis as the actual species present may be identified from the chemical shift for the element.

3.2.3 Instrumentation

3.2.3.1 Introduction

The XPS spectrometer used for all measurements is a Fisons Spectrometer built into the UHV system. It consists of a twin anode source, a Clam 2 Electron Energy Analyser, a channeltron and a small ion pump to pump off outgassed products from the anode. The sample is placed in the clamp of the XPS manipulator with the aid of a wobblestick. The sample is then positioned as close as possible to the X-ray source (~ 5 mm), with the aid of the X and Y-positioning micrometers screw gauges.

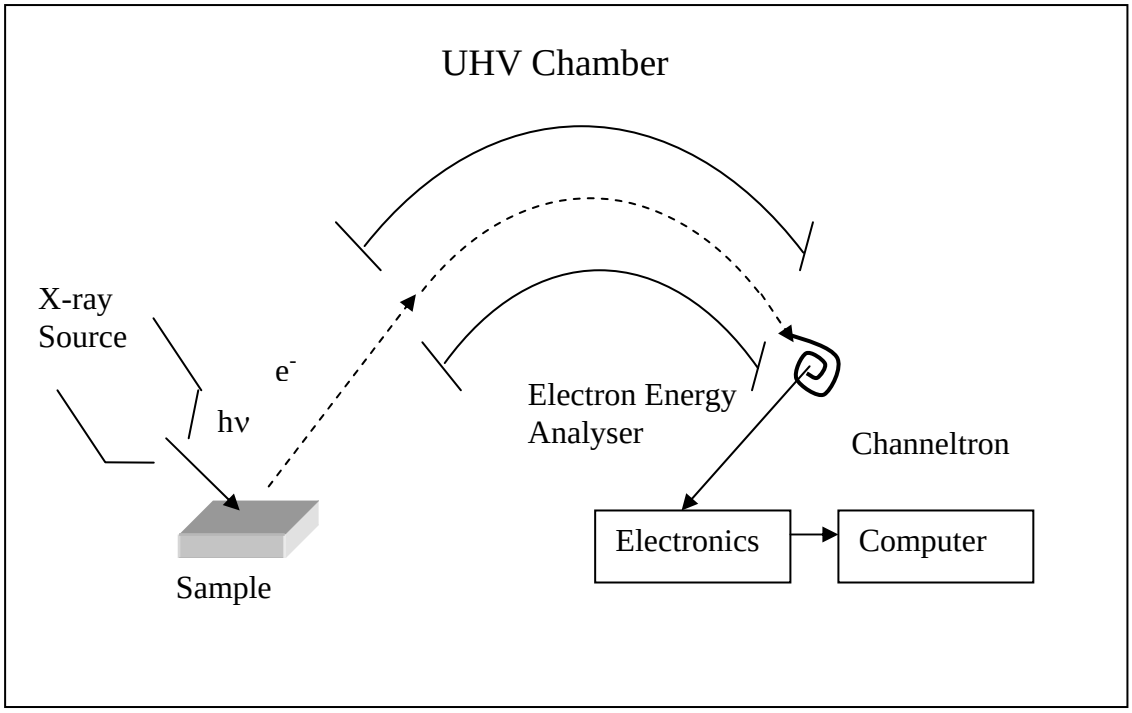

Fig. 3.6 : A schematic design of an XPS Spectrometer

3.2.3.2 Vacuum Requirements

As the sensitivity of the technique depends on the detection of electrons which are ejected from the surface of the sample, it is important that these electrons are not lost through collisions with gas molecules in the analysis chamber while they are travelling from the sample to the detector. This imposes a requirement that the spectrometer is operated in vacuum with pressures of 10^{-5} mbar or better. In the STM V, ultra high vacuum (UHV) conditions of 10^{-10} mbars are achieved with a combination of a pre pump, a diffusion pump, a turbomolecular pump, an ion getter pump and a titanium sublimation pump as described in Appendix 2.

3.2.3.3 X-ray Source

The choice of material for a soft x-ray source depends line width and the energy of the characteristic X-ray emitted by the material. From equation 3.1, it can be seen that the line width of the ejected electrons is dependent on the line width of the characteristic energy of the X-Ray photon as the work function can be considered to be a constant and the line width of $E_{B.E.}$ is very narrow. In general for best energy resolutions, materials which emit a

characteristic X-ray of line width of less than 1.0 eV are suitable as anodes. The actual choice of a material also depends on the magnitude of the characteristic energy. The characteristic energy must be large enough to be able to analyse as wide a range of elements as possible but small enough to ensure that only the surface of the sample is analysed. For example, Table 3.1 lists a few materials[43] which may be suitable as anodes.

Line	Energy, eV	Line Width, eV
Y M_ζ	132.3	0.47
Zr M_ζ	151.4	0.77
Mg K_α	1253.6	0.7
Al K_α	1486.6	0.85
Si K_α	1739.5	1.0

Table 3.1 : Energies and Line Widths of some characteristic X-ray lines

It can be seen from the above table that although both Y M_ζ and Zr M_ζ have narrow line widths of less than 1.0 eV, their line energies are too low to be of practical use in analysis. Si K_α on the other hand meets both the requirements for the line width and the line energy. However silicon is rarely used as an anode material and then only for special applications, as it is difficult to fabricate and it has poor heat conduction characteristics since it is a semiconductor. Therefore, Mg K_α and Al K_α are the two widely used soft X-ray sources in X-ray photoelectron spectrometers.

The generation of X-rays in a material is achieved by bombarding the material with electrons of sufficient energy. In our XPS spectrometer, this is set at 15 kV. As sensitivity is directly proportional to the oncoming photon flux at the sample, and hence to the electron current bombarding the anode, a high current is necessary to achieve optimal sensitivity. Furthermore, the irradiating flux is inversely proportional to the square of the distance between the sample and the anode. Hence, it is optimal to place the sample as close as possible to the anode barring other design concerns. So, taking these factors into consideration, the typical design for a X-ray twin anode source is shown in Fig. 3.7[43,44].

From Fig. 3.7, it can be seen that the ends of the Cu anode consist of two angled anode faces, one of which has an Al film deposited on it and the other a Mg film. The thickness of the films are such that there is no emission of Cu L_α radiation but thin enough such that heat transfer is not hindered. There are two semi-circular filaments, one for each anode. The filaments and the focusing shields are earthed while at the anodes the accelerating potential of up to 15 kV is applied. The filaments are positioned such that only the anode faces close to the respective filaments are bombarded by the electrons from the filaments. The X-rays thus generated pass through an aperture in the shield surrounding the x-ray source. The aperture is covered by a thin aluminium window of thickness of about 2 μm. The aluminium window blocks out stray electrons and contamination originating from the source and dissipates any heating effects. During operation, the anode is cooled by water to prevent overheating as this may lead to either interdiffusion between the aluminium and the magnesium anodes where spectral features due to dual excitation (ghost peaks) may arise or agglomeration of the two films which leads to features due to Cu L_α excitation.

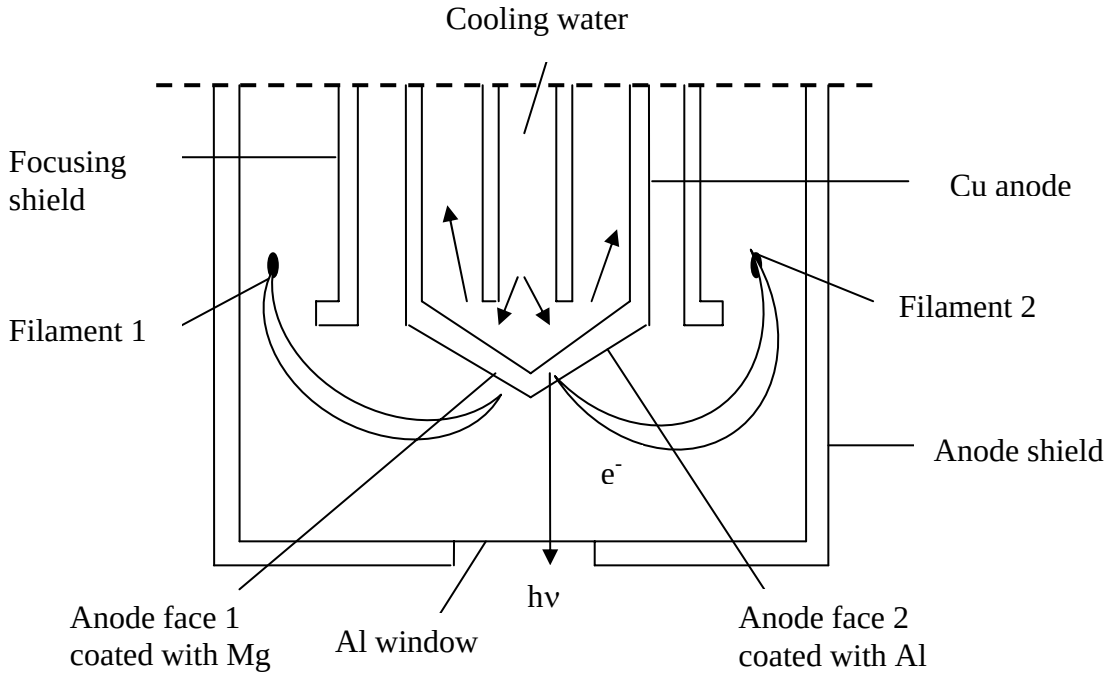

Fig. 3.7 : A schematic design of a typical twin anode X-Ray Source

3.2.3.4 Electron Energy Analyser

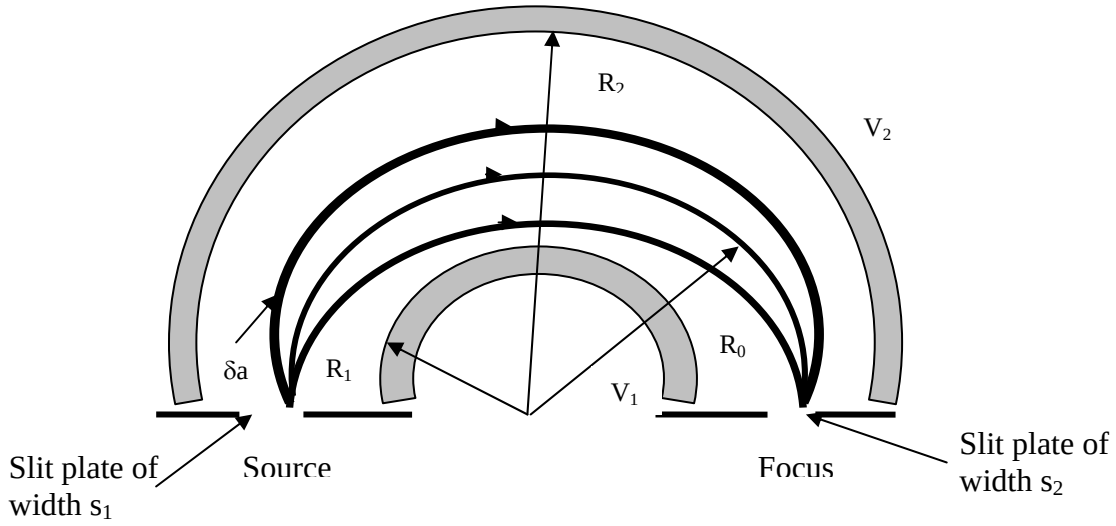

Fig. 3.8 : A schematic diagram of a concentric hemispherical analyser (CHA)[43]

In XPS differences due to different chemical states of the elements can be observed. As XPS is essentially a technique which measures the electron energy spectrum, the ability to resolve the peaks which are closely spaced is dependent on the energy resolution, which should be the same over the whole spectral range measured, and an acceptable signal to noise ratio at that resolution. Hence the electron energy analyser occupies a position of central importance. In the past there have been several different types of electron energy analysers. These have been

eventually abandoned for use in XPS (although they are in use in different spectrometers,) in favour of two; the cylindrical mirror analyser (CMA) and the concentric hemisherical sector analyser (CHA). The Clam 2 system, as all other modern XPS spectrometers, uses a concentric hemispherical analyser (Fig. 3.8).

In a CHA two hemispheres of radii R_1 and R_2 are placed concentrically. Two negative potentials, V_1 and V_2 are applied at the inner and outer hemisphere respectively such that V_1 is less than V_2. An electron entering the CHA will describe a circular path through the hemispheres, with a radius R_0. Hence the kinetic energy of the electron is :

$$eV = V_0 \qquad 3.3$$

where V_0 is the potential of the mean path through the CHA and is given by :

$$V_0 = \frac{V_1 R_1 + V_2 R_2}{R_0} \qquad 3.4$$

where R_0, R_1 and R_2 are fixed.

The line width of the peaks detected in the XPS is a function of the line widths of the X-ray source, the natural line width of the peak itself and the resolution of the analyser itself. As the line width of the source and the peak are inherent to the material, the resolution of closely spaced peaks is improved by changing the analyser resolution. As the resolution R is given by :

$$R = \Delta E/E \qquad 3.5$$

where ΔE is the the line width of the peak and
E is the kinetic energy of the electron.

For example, to achieve a line width of 0.5 eV across the entire spectrum, the resolution of the peaks would be :

At K.E. 1000 eV, 0.5/1000 = 0.0005 but
at K.E. 10 eV, 0.5/10 = 0.05.

So in order to improve the resolution and to keep it constant for the entire spectral range measured, it is necessary to retard the kinetic energy of the electrons entering the CHA. This is known as the pass energy and can be achieved by changing V_1 and V_2 in the above equation. A lower pass energy leads to an improvement in peak resolution. However, it must be noted that this is achieved at the expense of peak intensity. In practice, the pass energy is selected such that not only a good resolution is obtained but also an acceptable signal to noise ratio is achieved.

3.2.3.5 Detector

The typical detector used in an XPS spectrometer is a channeltron electron multiplier. This is a horn shaped dynode constructed with a special lead silicate glass which is formulated such that it has electron emissive properties. When an emitted photoelectron enters a channeltron, it strikes the input face of the channeltron, causing about 2-3 electrons to be emitted. The potential difference between the input and output of the channeltron which is

around 1-3 kV, causes these electrons to be accelerated further down the tube. As the channeltron is horn shaped, each emitted electron strikes various faces of the channel wall as it accelerates towards the end of the channeltron , emitting 2-3 electron with each strike, creating an avalanche of electrons (Fig. 3.9). Hence, each emitted electron can produce up to 10^8 electrons at the output.

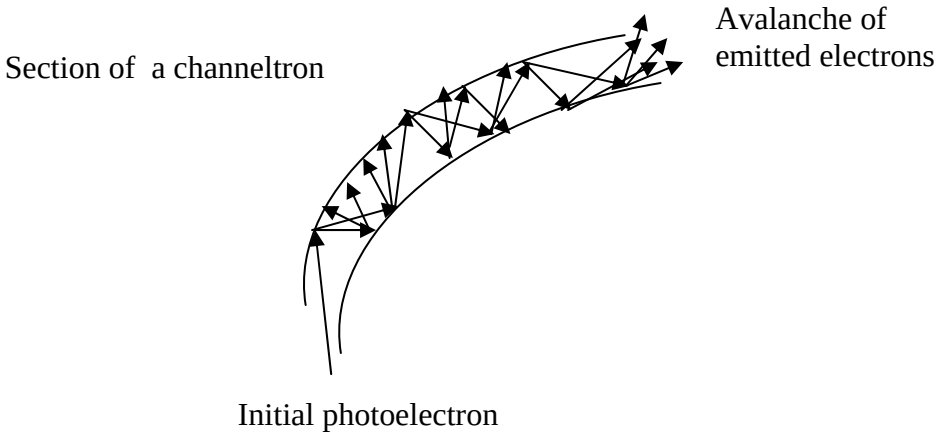

Fig. 3.9 : A diagram showing the avalanche effect in a channeltron

3.2.4 Data Processing

In an XPS spectrum the energy loss processes due to inelastic scattering result in the characteristic stepped background. Various processes including photon scattering, plasmon excitation, ionization and interband transitions, contribute to this loss which leads to a reduction of the kinetic energy of the emitted electron. The intensity of the background (due to the energy loss), is higher at the higher binding energy of the photoemission peak than at the lower binding energy. Hence for the quantitative analysis background corrections need to be carried out on all peaks that are to be quantitatively evaluated. So, to reduce the errors that arise out of the background corrections, peaks that have relatively close binding energies and therefore suffer similar loss processes are used for quantitative analysis. For these reasons the Ge 3d peak is used instead of the more intense Ge 2p peak as the former peak not only has a lower binding energy and therefore less energy losses but also has a binding energy which is closer to the Si 2p reference peak.

The background correction of the high resolution spectra is carried out using the Shirley correction[43,45] using Sigmaplot 2001. The Shirley background corrected peak is obtained from the following function:

$$G(E) = j(E) - j(E)_n\left(\int_0^n G(E)dE \Big/ \int_0^{n'} G(E)dE\right) \qquad 3.6$$

where $G(E)$, is the value after Shirley background correction, $j(E)$, is the experimental data obtained from XPS measurements and the term, $j(E)_n\left(\int_0^n G(E)dE \Big/ \int_0^{n'} G(E)dE\right)$ is the expression for the Shirley background correction. The background is determined iteratively from the experimental data for a number of pre-set iterations and the term $j(E)_n$ is the number

of counts in the final iteration. The ratio $\left(\int_0^n G(E)dE \Big/ \int_0^{n'} G(E)dE \right)$ goes from 0 to 1 across the range of iterations from 0 to n such that the background to be substracted matches the experimental value of the binding energy of each peak at its high side in the spectrum The resultant background corrected peak has an almost symmetrical Gaussian/lorentzian peak.

3.3 Scanning Tunnelling Microscopy (STM)

3.3.1 Introduction

The basic principle in STM involves applying a bias voltage between an atomically sharp metal tip and the surface of a conducting or semiconducting sample and then reducing the tip to sample distance to a separation of a few Angstroms, whereby a tunnelling current flows between the tip and the surface, due to the quantum mechanical tunnelling effect. As the tunnelling current is exponentially dependent on the tip to surface separation, the distance control based on tunnelling is very sensitive. Hence, by scanning the tip over the sample surface at a constant current which is maintained via a feedback loop, a three dimensional constant electronic density of states obtained by monitoring the position of the tip (z-direction) with respect to the scanning direction (x-y direction of the sample surface).

As the STM can be operated in air and in liquids, as well as in vacuum, it has useful applications in in-situ electrochemical studies as well as in the more traditional UHV studies in surface chemistry and physics. The main advantage of the STM is that it is a non-destructive way of obtaining real space information at an atomic level, in contrast to diffraction techniques. Hence, besides providing information about the atomic surface structure, it is also useful in the study of surface defects, such as steps, grain boundaries, vacancies, and impurities. A disadvantage with this technique is that the area of analysis is very small and there is a danger of drawing a conclusion for the whole surface based on a very small area. However, this can be overcome by carrying out multiple scans over different areas on the surface.

In recent years, with the shrinking chip geometries, the STM has new applications in fabrication of nanoscale devices, where the tip itself is used as a fabrication tool that is used to manipulate the surface atoms.

3.3.2 Theory of tunnelling

3.3.2.1 Time independent elastic tunnelling through a one dimensional rectangular potential barrier

The basis of the operation is based on the quantum mechanical effect of tunnelling which is forbidden in classical mechanics. In order to explain the concept of tunnelling we consider the simplest case which is of a particle confined in a one dimensional box where the potential energy is zero everywhere, except at the two walls, where it is infinite. According to classical mechanics, the particle has insufficient energy to overcome the potential energy barrier and hence will be confined within the box. However in quantum theory, the wave-particle duality of the electron, allows it to travel or tunnel through the barrier and to be found on the other side of the wall.

In order to explain this consider the case of a particle, with energy E, which is confined in a one dimensional rectangular barrier[46,47] with a potential barrier V (i.e. the potential energy does not rise up to infinity at the walls of the barrier). In the case of E<V, according to quantum theory the wave function does not decay to zero at the walls. If the walls are of a finite thickness such that the potential barrier falls to zero again, the wavefunction of the particle oscillates inside the box, varies smoothly inside the wall and oscillates again but with a reduced intensity on the other side of wall (i.e. outside the box). It must be noted that it is important that the wavefunction and the slope of the wavefunction be continuous at both edges of the potential energy barrier. This continuity allows for the connection of the wavefuntions in the three different areas shown in Fig. 3.10 and hence to obtain the solutions of the Schrödinger equation.

For the region on the left (x<0) of the wall (region 1 in Fig. 3.10), where V=0, the Schrödinger equation is as follows :

$$-\frac{\hbar^2}{2m}\frac{d^2\Psi_1}{dx^2} = E\Psi_1 \qquad 3.7$$

The solutions of the equation are

$$\Psi_1 = Ae^{ikx} + Be^{-ikx} \qquad 3.8$$

and $$k\hbar = \sqrt{2mE} \qquad 3.9$$

For the region inside $(0 \le x \le L)$ the wall (region 2 in Fig. 3.10), where the potential energy is V, the Schrödinger equation is:

$$-\frac{\hbar^2}{2m}\frac{d^2\Psi_2}{dx^2} + V\Psi_2 = E\Psi_2 \qquad 3.10$$

When E<V, V-E is positive and hence the solution for the Schrödinger equation is:

$$\Psi_2 = Ce^{\kappa x} + De^{-\kappa x} \qquad 3.11$$

and $$\kappa\hbar = \sqrt{\{2m(V-E)\}} \qquad 3.12$$

The exponentials are now real funtions, instead of the complex oscillating functions in the regions (regions 1 and 3 in Fig. 3.10) where the potential energy is zero.
For the region on the right of the wall (region 3 in Fig. 3.10), where x>L, the potential energy is again zero. Hence the wavefunction and the solution are :

$$\Psi_3 = A'e^{ikx} + B'e^{-ikx} \qquad 3.13$$

and $$k\hbar = \sqrt{2mE} \qquad 3.14$$

Therefore the complete wavefuntion describing the motion of the particle from the left of the barrier to the right of the barrier consists of the incident wave from the left, the reflected wave from the left of the barrier, the exponentially decaying amplitude inside the wall and the

oscillating wave of the particle to the right of the wall after it has tunnelled through the wall. For the wavefunctions to be acceptable, Ψ must not be infinite anywhere and the wavefuntion must be single valued at each point in space.

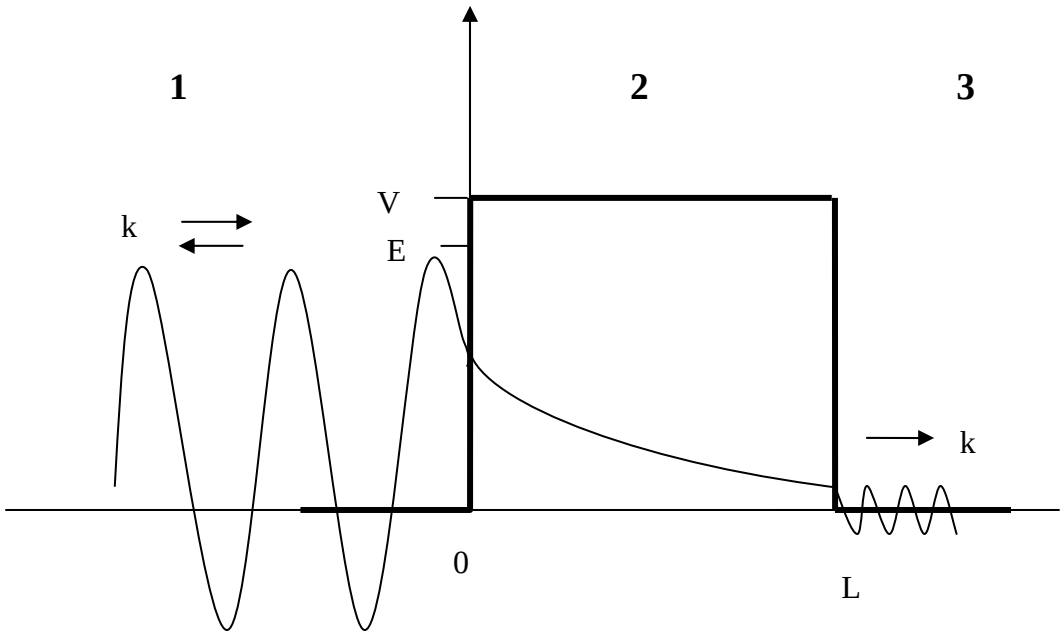

Fig. 3.10 : One dimensional rectangular potential barrier with height V and width L.

It must be continuous with no kinks or sharp points especially at the edges of the barrier where x=0 and x=L, $e^0=1$. Then,

$$A + B = C + D \qquad 3.15$$

and $$Ce^{\kappa x} + De^{-\kappa x} = A'e^{ikx} + B'e^{-ikx} \qquad 3.16$$

Further more the slopes (first derivatives) must also be continuous. Then,

$$ikA - ikB = \kappa C - \kappa D \qquad 3.17$$

and $$\kappa Ce^{\kappa x} - \kappa De^{-\kappa x} = ikA'e^{ikx} - ikB'e^{-ikx} \qquad 3.18$$

If the particles are traveling to the wall from the left, then there will be no particles traveling to the left, from the right side of the wall. Therefore, $B' = 0$. However, $B \neq 0$ as some particles are reflected from the wall in the negative x direction (Fig. 3.10). The probability that the particle is traveling towards to the right, on the left side of the wall is $\propto |A|^2$ and the probabilty that the particle is traveling to the right, on the right side of the wall is $\propto |A'|^2$. The ratio of these probabilities can be calculated[46] and is called the transmission probability T which is given by equation 3.19.

$$T = \frac{P_t}{P_r} = \left\{ 1 + \frac{(e^{\kappa x} - e^{-\kappa x})^2}{16\varepsilon(1-\varepsilon)} \right\}^{-1} \qquad 3.19$$

where $\varepsilon = \frac{E}{V}$ 3.20

For high, wide barriers, $\kappa x >> 1$ and T, reduces to

$$T \approx 16\varepsilon(1-\varepsilon)e^{-2\kappa x} \quad 3.21$$

where the decay rate

$$\kappa = \frac{\sqrt{2m(V-E)}}{\hbar}. \quad 3.22$$

It can be seen that the transmission probability T varies exponentially, with the barrier thickness and the square root of the barrier (V-E) thickness and mass of the particle. A consequence of this relation is that particles with low mass such as electrons are more able to tunnel through the barrier than heavier particles. It can also be seen with the above equations that due to the strong exponential variation of T with respect to the barrier thickness, assuming a barrier thickness of 5Å and a barrier height of 4eV (with an exponential factor of 10^{-5}), a change of a barrier width of 1Å would then lead to a change in the transmission by one order of magnitude. This extreme sensitivity of the transmission through the wall by tunnelling to the barrier width leads to high vertical resolution and is the heart of the technique of Scanning Tunnelling Microscopy.

3.3.2.2 Perturbation Theory of STM - Tersoff Haman Model

To have an understanding of the atomically resolved images obtained from the STM, an explanation of the lateral corrugation which comes from the surface structure is required. This can be understood using the Tersoff and Hamann[48,49] model which is based on Bardeen's Hamiltonian[50]. This provides a simple but more realistic three dimensional quantum mechanical model for tunnelling than the one dimensional barrier model which has been discussed in the previous section.

Fermi's golden rule which is used to describe the electronic transitions in perturbation theory, states that the transition probability (from an initial state ψ_i to all final states ψ_f, per unit time) is a product of the prefactor $2\pi/\hbar$, the square of the absolute of a transition amplitute and the density of the final states at the energy E_i of the tunneling electron $\sum_f \delta(E_f - E_i)$. The transition amplitute is the matrix element of a transition inducing potential V_{curr} (for the STM) between the initial and final states ψ_i and ψ_f repectively, with corresponding energies, E_i and E_f where the initial state is the wave function containing the electron before the transition and the final state, the wave function containing the electron after the transition. Assuming elastic tunneling conditions, the current is obtained by multiplying the transition probability with the electron charge, e and is as follows :

$$J_i = \frac{2\pi e}{\hbar}\sum_f \left|\langle \psi_f | V_{curr} | \psi_i \rangle\right|^2 \delta(E_f - E_i) \quad 3.23$$

The Hamiltonian is written as

$$H = H_0 + V_{curr} = H_{tip} + H_{sample} + V_{curr} \qquad 3.24$$

with $H_{sample}\psi_f = E_f\psi_f$ 3.25

where H_0 describes the two non-interacting electrodes, the isolated tip apex (H_{tip}) and the sample $\left(H_{sample}\right)$ and V_{curr} is the interaction potential between the tip and the surface of the sample.

In the case where the current flows from the tip to the sample, according to Fermi's golden rule, ψ_i is assumed to be an eigenstate of the tip electrode. Hence,

$$H_{tip}\psi_i = E_i\psi_i \qquad 3.26$$

The Tersoff-Hamann approximation is the simplest case where the tip is assumed to be the ideal, single spherical point. Hence the tip wave function is represented by spherical s-type wave function.

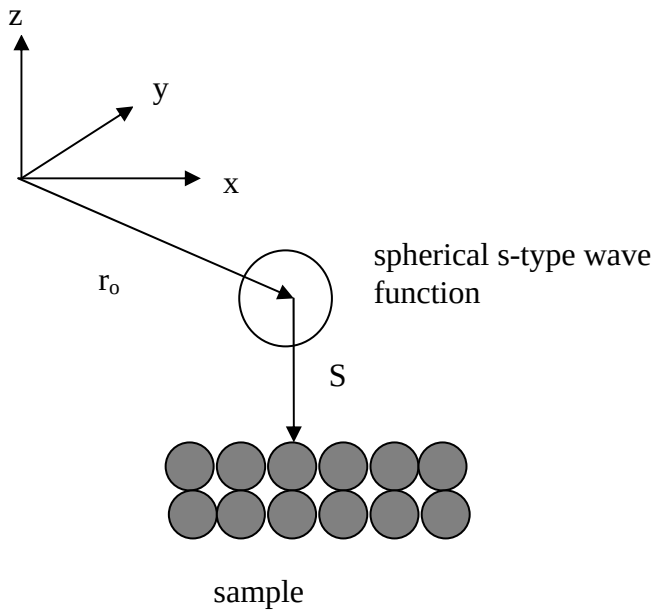

Fig. 3.11 Tersoff-Hamann approximation of the tip wave function as a spherical s-type wave function at a position r_o and a distance S from the surface of the unperturbed sample[51].

Assuming that[51],

1. ψ_i is real,
2. $H\psi_f = E_f\psi_f$ within the sample and the barrier and
3. $V_{curr}\psi_f \neq 0$,

the tunnelling current is now approximated to be as follows

$$I \propto \sum_f \left|\psi_f(r_o)^2\right| \delta(E_f - E_F) = \rho(r_o, E_F) \qquad 3.27$$

and is now related to $\rho(r_o, E_F)$ which describes the local density of states (LDOS) of the surface at the Fermi level with respect to the position of the tip apex at the sample. Hence, the atomically resolved STM images can be regarded as a contour map of the charge density at the Fermi level[51-53]. Therefore, the lateral corrugations measured in the STM in the constant current mode in the STM are a consequence of the variations in the local charge density of the surface states due to the periodicity of the crystal lattice.

In the case of the Si(111)-(7×7), the work of Binnig and Rohrer[54] and Hamers[55] has helped to elucidate its geometric and electronic structure and hence support the DAS model which has been by Takayanagi[19,56]. The experiments of Binnig and Rohrer[54] have shown that at a tunnelling voltage 2.5 V, of the (7×7) unit cell is imaged to be a rhombohedral bounded by deep corner holes encompassing 12 uniform maxima (seen as bright spots) with diagonal dimensions of 46×29 Å. The 12 maxima are attributed to be from the three fold coordinated silicon adatoms and the empty sites (imaged as dark spots) at the corners to be the corner holes. However, the tunnelling experiments carried out at -2.0V , reveal an asymmetry in the unit cell, where one half of the rhombohedral consisting of a triangular arrangement of the 6 adatoms is imaged to be brighter than the 6 adatoms in the other half of the unit cell. This indicates that one half of the unit cell is higher than the other half. This displacement is shown to be approximately 2 Å[54] and is attributed to the presence of a stacking fault on one half of the unit cell (faulted half, F). The other (brighter) half which does not have the stacking fault is designated as the unfaulted half, U. Hence the STM provides the crucial evidence to the acceptance of the Takayanagi DAS model for the (7×7) reconstruction of Si(111).

3.3.3 Instrumentation

The STM V is a home-made beetle STM (Fig. 3.12) based on the original Besocke STM[57-59]. For high resolution work a high tip to sample stability is required. So vibration isolation is of great importance for the instrument. The STM V is located in the cellar where floor vibrations are greatly reduced. The entire UHV table is further dampened via external dampening by mounting the system on top of a table supported by 4 pneumatic dampeners which are in turn positioned on individual concrete blocks. To dampen high frequency vibrations, the STM is placed on top of a stack of copper plates with strategically placed viton spacers for additional dampening.

The microscope itself consists of a triangular stage with 4 piezo electric tubes, a sample ring which has 3 ramps cut into its underside and three ruby balls on which the ring rests on. The ring rests on three of the (outer) piezos, which enable the movement in the x-y direction as well as in the clockwise and anti-clockwise direction. Scanning is achieved by applying the same amount of scanning pulses to each of the outer piezos. In order to rotate the ring, a different pulse is applied to each of the outer piezos. Hence the three piezos no longer bend in the same direction but tangentially with respect to the ring. This results in a upward or downward motion of the ring. The fourth piezo which is in the centre of the triangular stage, is the z-piezo which holds the tunnelling tip.

The coarse tip approach[58] in STM V is automatically controlled by the STM electronics and is as follows. When the electronics is switched to the approach mode, individual pulses are

applied to each of the outer piezos, such that they first bend to one side and then quickly to the other side. This causes the ruby balls which rest on top of the piezos to slide along on the ramps which are cut into the underside of the ring causing the ring to move upwards and downwards through the rotating motion of the ring in small steps which have been preset. The distance between the tip and the sample decreases with successive cycles and ends automatically once the tip is within the approximate tunnelling distance to the sample. The final tip approach is carried out manually where small pulses are applied until the tip approaches the tunnelling distance to the sample. The electronics are then switched to the tunnelling mode for scanning where the sample scanning takes place by moving the inner piezo which holds the tunnelling tip.

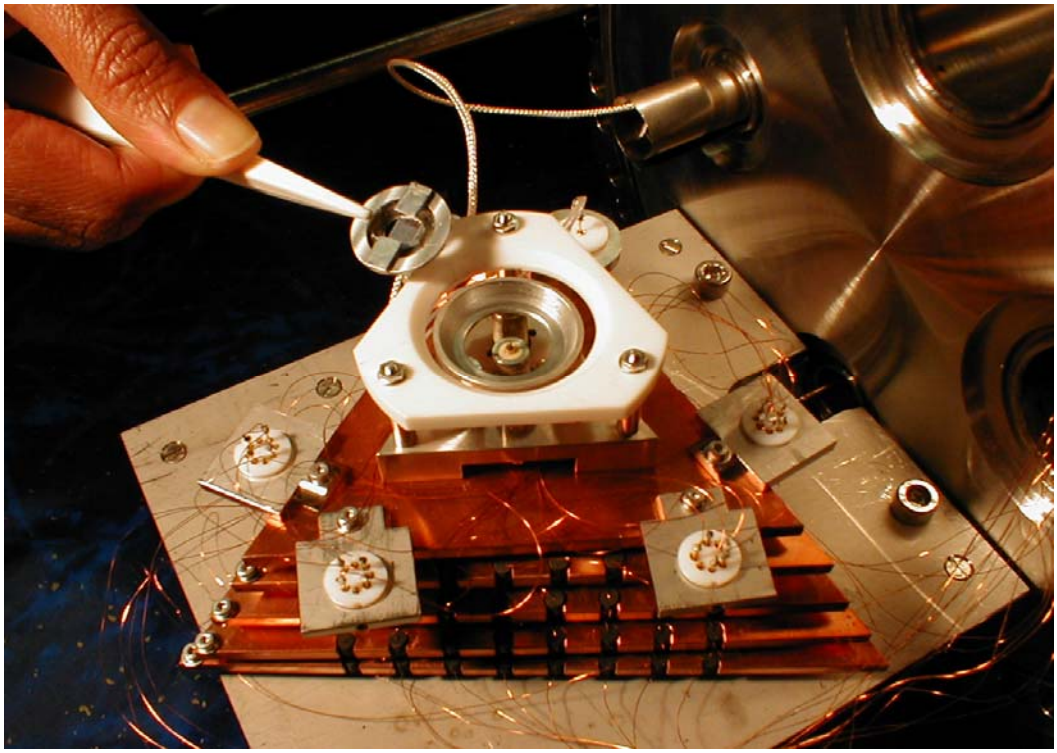

Fig. 3.12 : Home-made beetle STM

3.4 Sample Preparation

3.4.1 Storage and Handling

All samples have been handled under the flow box, with clean teflon tweezers and gloves. Beakers that are used for cleaning the sample and sample holder, have been rigorously cleaned by soaking for 24 hrs in Caro's acid (H_2SO_4+H_2O_2) followed by multiple rinses in distilled deionised water and a final clean in boiling distilled deionised water (2hrs). The dry beakers thus cleaned are finally rinsed with the chemicals which they will contain, labelled and have only been used for their respective purposes. Only teflon beakers have been used for HF solutions while the regular Duran glass beakers are used for all other chemicals. All wafers and samples have been kept under a flow box.

3.4.2 Standard Si(111) – (7×7) sample

The Si(111) samples are either the 10mm x 5 mm pieces cleaved out of a 6" ultrapure silicon wafer from Siltronic AG (Burghausen) or the 'pre-cut', low offset orientation wafer samples of a similar size from CrysTec Crystaltechnologie.

3.4.2.1 Clean Si(111) sample

Prior to introduction into the UHV system, the silicon samples are cleaned[12] ultrasonically in VLSI (Merck) grade Acetone for 15 min, which is followed by 15 min of ultrasonic cleaning in VLSI (Merck) grade methanol. The molybdenum sample holder is cleaned by first boiling it in conc. HCl for 15 min (to remove any reactive contaminants) and this is followed by the above cleaning procedure for the sample. The sample is then mounted in the sample holder and introduced into the UHV system via the loadlock.

As the sample has been cleaned in organic solvents, it is degassed overnight in the UHV system to remove the adsorbates on the surface. The filament of the wehnelt is first degassed at 1.5 V (1.5 A) for one hour. The wehnelt is then set at 50 V and the high voltage at 1.5 kV with a current limit of 0.3 A. The voltage at the filament is slowly increased such that at any one point the system pressure does not rise beyond 1.0×10^{-8} mbar. Once an emission current (at the sample) of 0.2 mA (500 K) is measured the sample is left to degas at this temperature for one hour. After that, the voltage at the filament is increased (again taking care that there is no large pressure rise), until an emission current of 2.0 mA (750 K) is reached. The sample is then allowed to degas overnight (a min. of 8 hours). When the sample has been completely degassed, the emission current will have increased to about 4.54 mA which corresponds to a substrate temperature of about 850 K.

3.4.2.2 Reconstruction from Si(111) – (2×1) to (7×7)

As a clean silicon surface is highly reactive, a layer of native oxide is immediately formed after chemical cleaning. This layer of oxide has to be removed before the the silicon is reconstructed. This is done by flash heating the sample to a temperature below the melting point of the crystal. The temperature of 1430 K is chosen as it is just high enough to flash off the oxide on the surface and any remaining surface carbon (confirmed by XPS studies) but low enough such that no surface deformation due to the melting and subsequent rapid cooling of the crystal occurs. This temperature is achieved by setting the wehnelt at -180V, the high voltage at 1.5 kV (with a current limit of about 4 A) and the voltage at the filament at about 5 – 7 V. The flashing procedure is carried out by rapidly heating the sample to 1430 K for about a second followed by rapid cooling. This is repeated about 5 times, by which time there is a minimal pressure increase, indicating that the surface components have been mostly removed. To ensure that almost all of these components have been removed, a final flash step is carried out, where the sample is heated to 1430 K for about 30 s, followed by rapid cooling. An optical pyrometer (with the emissivity set at 0.6 for Si) is used to monitor the temperature of the sample during the flash and reconstruction procedure.

The next step after flashing is the reconstruction itself. The sample is rapidly heated to 1430 K, then is rapidly cooled down to 1160 K, then is slowly cooled down at a rate of 1 K per min to 1090 K after which the heating is cut off, and the sample is allowed to cool down to room temperature (Fig. 3.13).

The flash and reconstruction cycle is controlled and carried out using a labview program and a PCI 6024 E computer interface card from National Instruments Appendix 1).

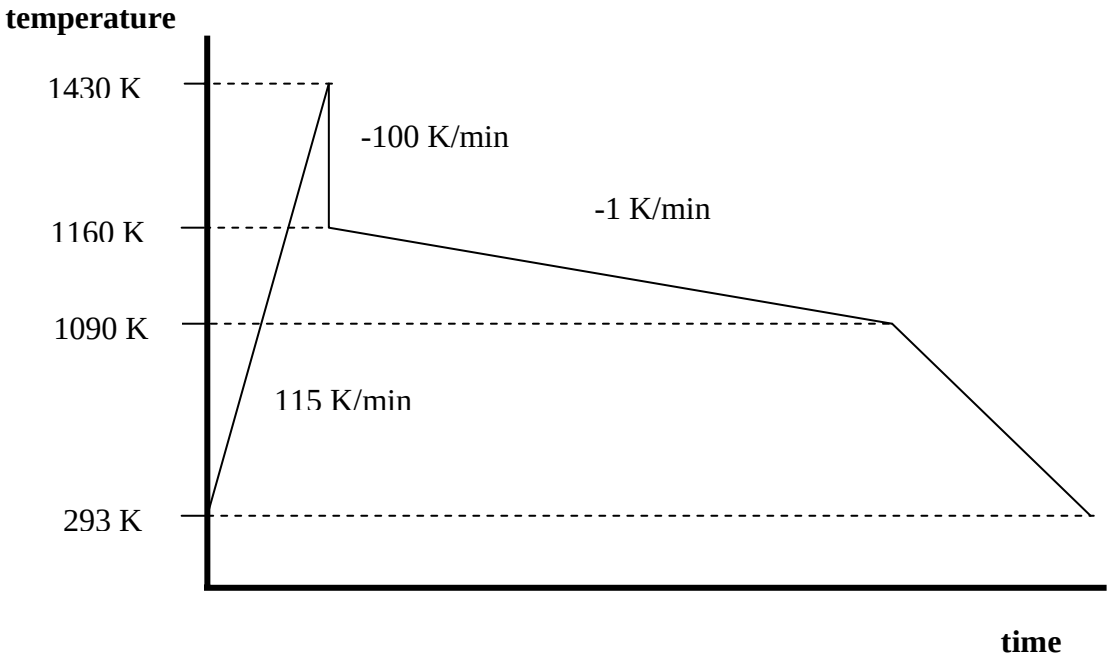

Fig. 3.13 : Heating and cooling profile for Si(111)-(7×7) Reconstruction process

The cooled sample is surveyed by the STM prior to deposition. The ideal surface after the reconstruction procedure has a low defect (white arrow in Fig 3.14a) density as is shown in the atomically resolved STM image in Fig. 3.14a and equidistant monoatomic steps (Fig. 3.14b).

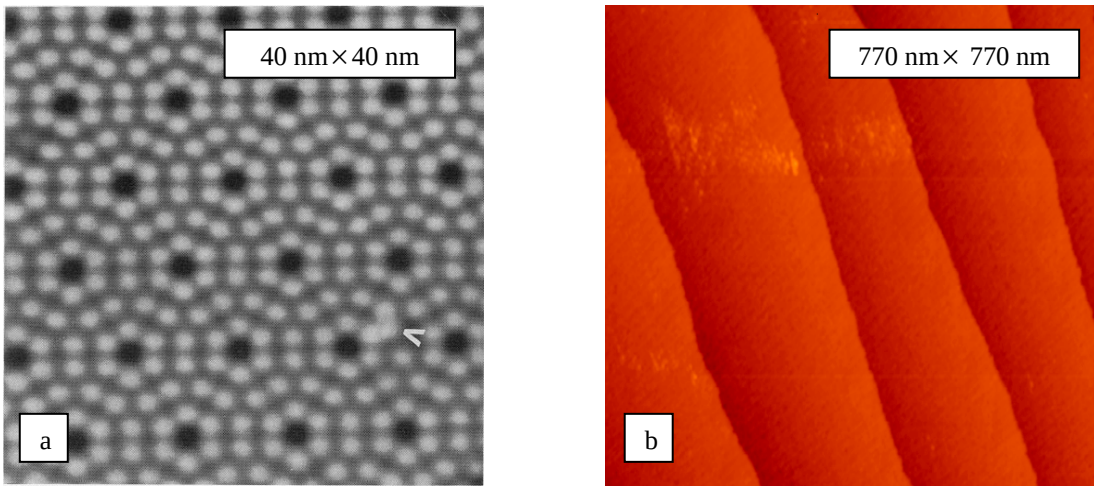

Fig. 3.14 : STM Images of Clean (reconstructed) Si(111)-(7×7)
(a) 40 nm×40 nm atomically resolved Si(111)-(7×7), (b) 770 nm ×770 nm monoatomic steps

3.4.3 Standard Ge(111) – (1×1) sample

The Ge(111) samples have been cleaved out of 2" (5 cm), single side polished, Ge(111) wafer from Siemens.

3.4.3.1 Clean Ge(111) sample

The Ge(111) sample that has been used for the XPS quantification studies is cleaned as per the etching and annealing procedure by Prabhakaran et al.[60]. As for the silicon sample, the Ge sample is first cleaned by sonication for 15 min in acetone which is followed by 15 min of sonication in methanol. Then the sample is rinsed in running DI water, a 5-10s dip in a 9:1 HF, DI water solution. This is followed by another DI water rinse. A thin layer of oxide is then prepared by dipping the sample for about 15s in a 9:1 H_2O_2, DI water solution. The excess solution is rinsed off in DI water. The thin oxide layer is subsequently etched off by dipping the sample for 5s in the 9:1 HF, DI water solution. To ensure that several atomic layers are removed, the oxidising and etching process is repeated 4 times. Then the final oxide layer is prepared by dipping the sample in the peroxide solution. The sample is dried in dry argon, mounted on an aluminium sample holder which has been cleaned in acetone and methanol (15 min of sonication each) and transfered to the UHV system via the load lock.

The sample is transferred to the wehnelt assembly and degased for 30 min at 300°C and then annealed at 500°C for 15 min, to remove the thin surface oxide (as confirmed by XPS).

3.4.4 Chemical Vapour Deposition

3.4.4.1 Preparation of the precursor gas supply lines

The individual supply lines of the precursor gases are prepared for filling by being flushed with nitrogen of purity 6.0 which is then pumped out by the small turbo via the loadlock. As a final step the lines are heated (while pumping with the small turbo) via heating coils with the variable transformer set at 100V for 2 hours. The mixing chamber for the precursor gases is prepared at the same time as above. When cool, the supply lines and the mixing chamber are further prepared by flushing with three full fillings in the mixing chamber with the required precursor gases.

3.4.4.2 CVD Procedure

The CVD is carried out under UHV (ultra high vacuum) conditions with a baseline system pressure of 1.0×10^{-10} mbar or better. For Ge deposition on Si, GeH_4 is used as the precursor gas and for the deposition of the Si_xGe_{1-x} alloy, disilane and germane are used as precursor gases. The disilane is supplied by BOC and has a purity of at least 99.994% while the germane is supplied by Messe Griesheim and has a purity of 99.999%. The precuror gases for CVD are delivered to the system via the mixing chamber. For the mixed gas CVD, the appropriate mix of disilane to germane is prepared in the mixing chamber with the aid of a baratron.

The purity of the precusor gas in the system is verified by the QMS. The deposition pressure is monitored by the Millenia IPGC1 ion gauge at low deposition pressures and the spinning rotor gauge at high pressures. During deposition the sample is heated via the Wehnelt by electron bombardment on the unpolished side. The precursor gases are delivered to the surface of the sample by a capillary which is placed at close proximity to the sample.

Chapter 4

Characterisation of Ge structures grown by CVD on standard and XPS exposed Si(111) – (7×7) surfaces

4.1. Introduction

Previous studies[11,12] of Ge deposition on the Si(111)-(7×7) surface by CVD have reported growth of MBE like 3D structures if the surface is irradiated by soft x-rays prior to deposition. In comparison, it has been reported that the epitaxial growth of the film grown by CVD is layer by layer and appears to terminate after 2.5 BL (effective thickness of 0.8 nm) under certain growth conditions. It has been suggested[11,12] that x-ray photons induced sub-surface C_s/C_i defects promote the growth of these 3D structures.

The first objective of the work described in this chapter is to ascertain if the Ge growth by CVD terminates after 2.5 BL or if the growth mode is the Stranski-Krastanov (S-K) growth under the CVD conditions set out in Ref. [11] and [12]. The second part of the work is to characterise the 3D structures.

In this work, Ge deposition has been carried out by CVD at a temperature of 750K which is the temperature at which the hydrogen desorption rate from the Si(111) surface is low. The Si(111)-(7×7) substrates are either the clean reconstructed samples or have been irradiated prior to deposition to create defects. Deposition is then carried out at different GeH_4 exposures and subsequent Ge growth has been studied by the STM (scanning tunnelling microscope), the AFM (atomic force microscope) and the TEM (transmission electron microscope).

4.2. Characterisation of 3D Ge growth by CVD on standard and irradiated Si(111) – (7×7) by STM and AFM

4.2.1 Experimental Procedure

The samples which have been reconstructed as described in Chapter 3 were surveyed by the STM prior to deposition. As outlined in Fig. 4.1, there are three preparation schemes, standard, irradiated, and irradiated and annealed. For the standard sample (Fig. 4.1), deposition is carried out immediately after the STM survey. The irradiated sample[11,12] (Fig. 4.1) is prepared by irradiating the surface by X-Rays for 30 minutes followed by the same

deposition scheme as the standard sample. The Al K_α (1486 eV) line of the XPS (300 W) is used for the irradiation. The last preparation scheme, the irradiated and annealed sample, is prepared by first irradiating the clean reconstructed substrate as outlined above. This is followed by a high temperature annealing at a 1000 K for 10 minutes with rapid cooling at the end of the annealing step. Finally deposition is carried out using the parameters described below.

Deposition is carried out at a temperature of 750 K and a deposition pressure of 7×10^{-5} mbar. The deposition times ranged from 30 minutes to 4 hours and varied at 15 minute intervals. This corresponds to an exposure range of 95 000 L to 760 000 L. STM imaging has been carried out on the samples where possible, followed by XPS measurements. The samples are then removed from the chamber and AFM imaging is carried out in air.

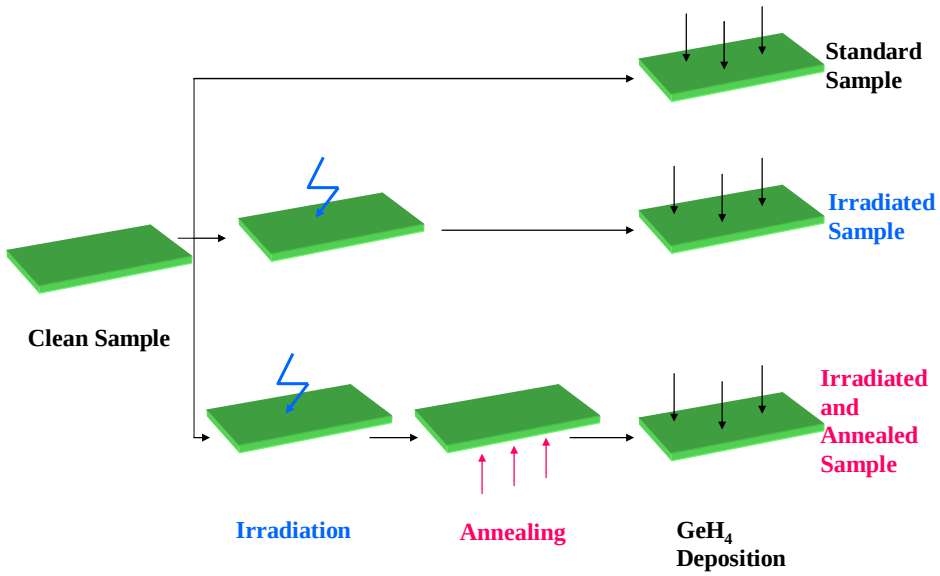

Fig. 4.1 : Sample Preparation Schemes

4.2.2 Results

Calculation of the Germanium Coverage

The germanium coverage is calculated from XPS peak integrals. An overview spectra (Fig. 4.2) is obtained at each deposition, followed by the high resolution spectra recorded at a pass energy of 20 eV of the Ge 3d and the Si 2p peaks. These two peaks are chosen as their binding energies are relatively close (Fig. 4.2) in comparison to the Ge 2p peaks (which have a higher intensity) as this facilitates the process of background correction and the quantitative evaluation of the Ge coverage. The high resolution spectra of the pure Si and Ge substrates have been obtained prior to the CVD experiments to facilitate the calibration of peak intensities of the bulk Si and Ge signals. The clean Si and Ge substrates are prepared as described in Chapter 3. The raw data files of the high resolution XPS spectra are imported into Sigmaplot 2001, which is then used to perform the background correction using the Shirley Background correction algorithm[61,62]. The peak intensities (areas) for the background

corrected peaks are calculated using Sigmaplot 2001. These values are then used in eq. 4.1[43] in order to calculate the effective thickness of the germanium film at each exposure for each substrate.

$$d_{Ge} = \lambda_{Ge/Si} \times \cos\alpha \times \ln\left[1 + \left(\frac{I_{Ge}}{I_{Si}} \times \frac{I^{o}_{Si}}{I^{o}_{Ge}}\right)\right] \qquad \text{Eq. 4.1}$$

where

d_{Ge} : effective thickness of Ge film

$\lambda_{Ge/Si}$: inelastic mean free path of the photoelectron

α : angle of detection with respect to the surface normal

I^{o}_{Si} & I^{o}_{Ge} : peak intensity of pure Si and Ge respectively

I_{Ge} & I_{Si} : peak intensities of the Ge film and the Si bulk respectively (of the measured sample)

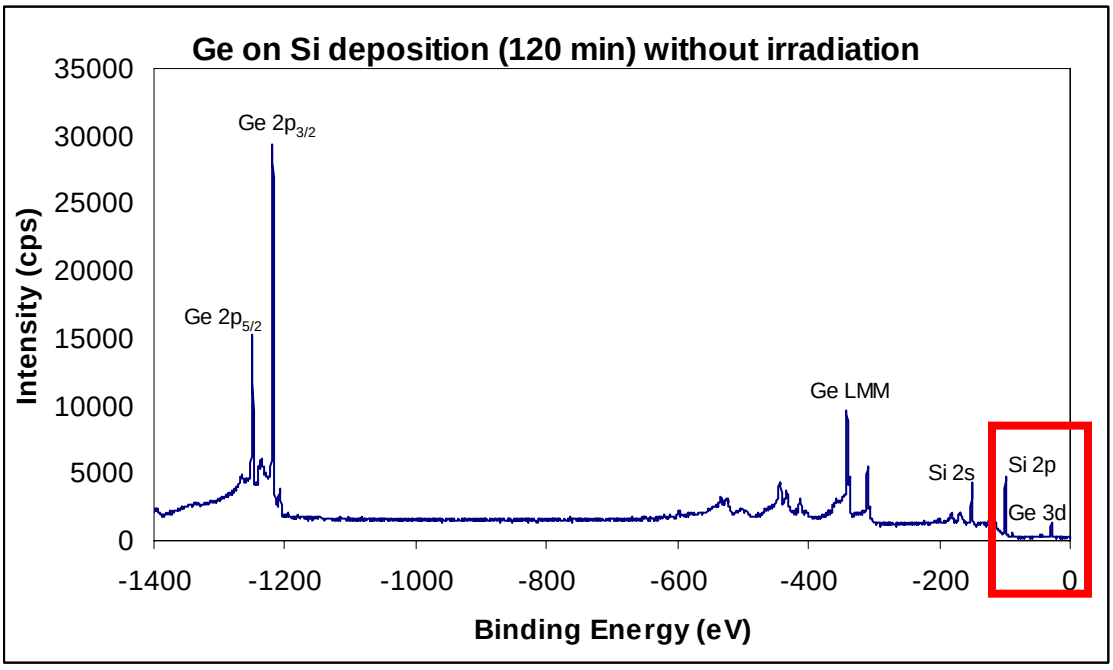

Fig. 4.2 : XPS Overview Spectra of Ge deposited on an irradiated Si(111)-(7×7) substrate, 750 K, 380 000 L.

The resulting values for coverage (effective film thickness) are then plotted against the corresponding values for exposures (Fig. 4.3) for both the standard and irradiated samples. It is observed that for both the standard and irradiated samples, there is a steep increase in coverage up to 100 000 L after which the increase is more gradual. However, there is little difference in the coverage values between the standard and irradiated samples at their corresponding exposures.

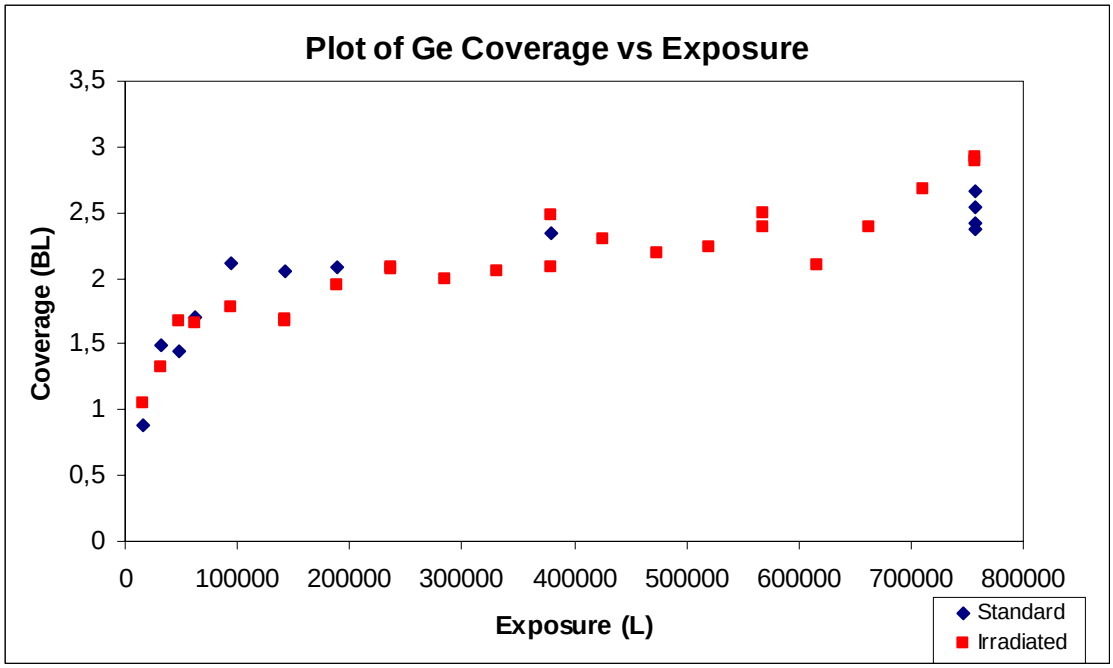

Fig. 4.3: Plot of Coverage vs Exposure for both the Standard and Irradiated Samples.

However, subtle differences between the standard and the irradiated samples are seen when the integrated sticking coefficients are calculated over the different exposure ranges.

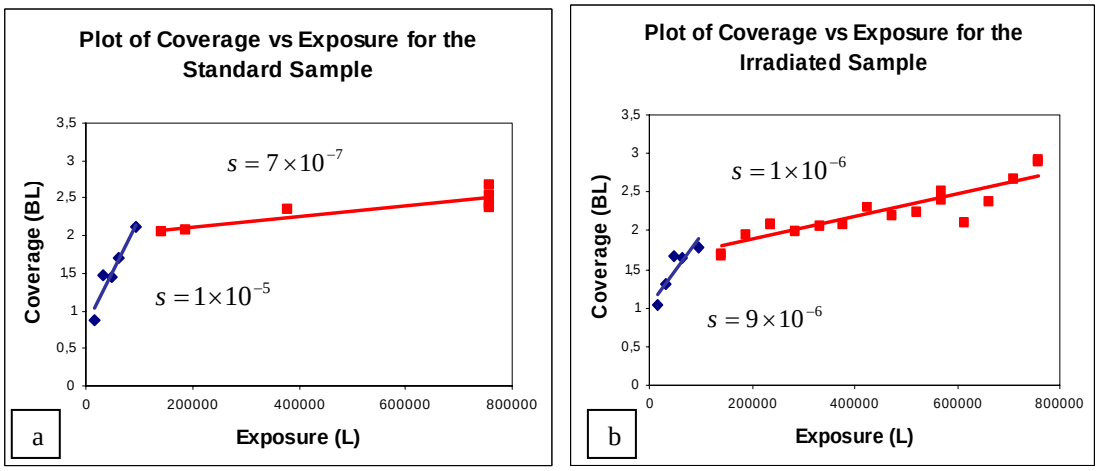

Fig. 4.4 : Coverage Plots vs exposure plots with sticking coefficients for (a) Standard sample, (b) Irradiated Sample.

In Fig. 4.4, the sticking coefficients of both types of samples have been linearised over two ranges of exposure, 1500 L to 95 000 L (low exposure) and 140 000 L to 760 000 L. It can be seen that there is little difference in the sticking coefficients of both types of samples at low exposures. However, at exposures greater than 95 000 L, the sticking coefficient ($s = 1\times10^{-6}$) for the irradiated sample is higher than the sticking coefficient ($s = 7\times10^{-7}$) for the standard sample. This can be seen in the slight difference in the steepness of the slopes in the second exposure range in Fig. 4.4.

This difference in the sticking coefficients over the two exposure ranges described above, could be due to the formation of the initial wetting up to 95 000 L. At higher exposures strain

release and 3D islanding is likely to predominate. The differences in the island growth morphology between the standard and the irradiated samples will be discussed in the succeeding sections.

Ge on standard Si(111) – (7×7)

Ge-(5×5) DAS structures are seen in the STM images at low exposures but at higher exposures (760 000 L) the more unusual Ge-(7×7) DAS structures[63-69] (Fig. 4.5) have been detected. Large scale STM images show highly irregular 3D structures which have cavities in the centre (Fig. 4.6).

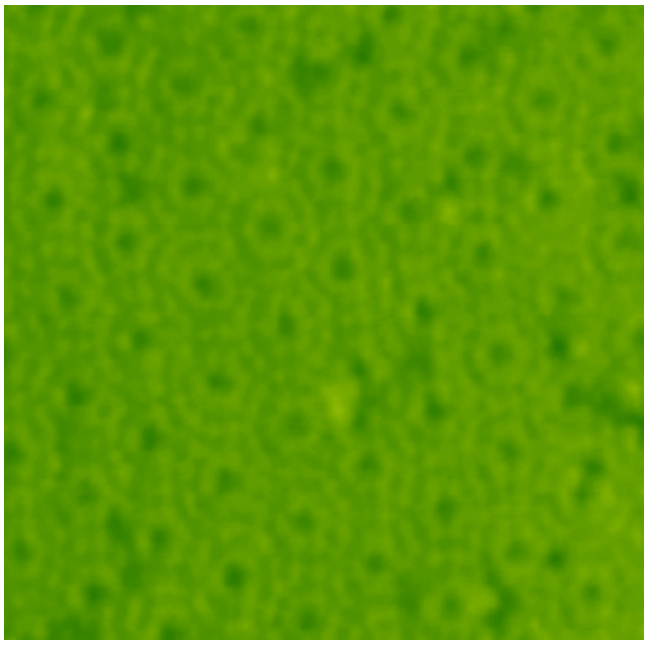

Fig. 4.5 :STM images after Ge Deposition by CVD, Standard Sample, 750 K, 58 nm × 58 nm, 760 000 L, Ge-(7×7)

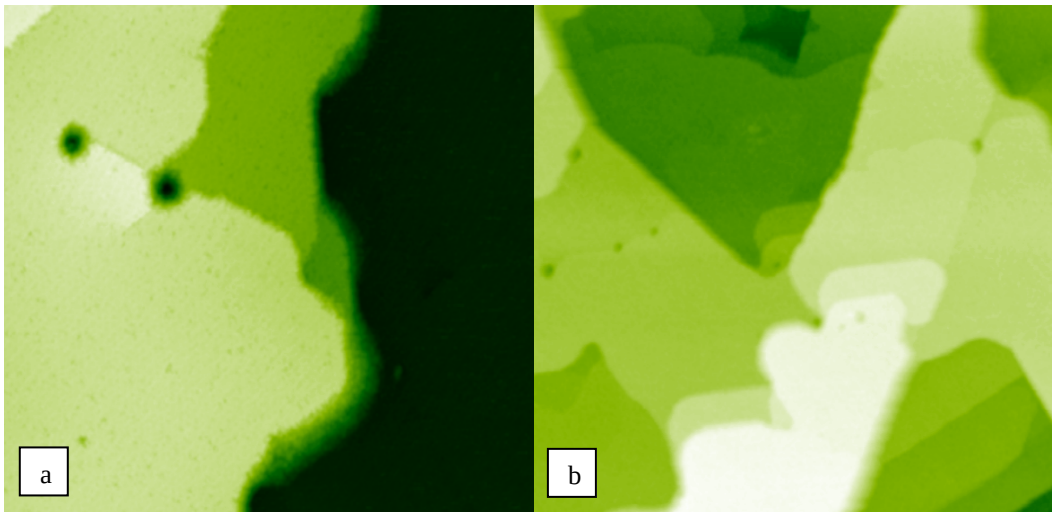

Fig. 4.6 : STM images after Ge Deposition by CVD, Standard Sample, 750 K, 760 000 L. (a) 218 nm×218 nm, (b) 2059 nm×2059 nm

The AFM images of the Standard sample at low exposures of 95 000 L indicate a fairly flat surface (Fig. 4.7a) with the beginnings of island formation. At higher exposures of 760 000 L,

the AFM images (Fig. 4.7b-d) show the presence two types of Ge 3D structures both of which are longer than they are wide. One type of structure with a centre cavity, has been described as an atoll structure[64] (Fig 4.7c) in MBE experiments, while the other is a flat topped polygon (Fig. 4.7d). The incidence of the former structure is greater than that of the latter by a factor of 12 (Fig. 4.7b). In addition, trenches of an average depth of about 7 nm are seen around both types of islands in the standard sample. The island density of the 3D structures at the high exposure of 760 000 L (Figs. 4.7b) is of the order of 0.9-2 islands per μm^2. The height of these islands is on average about 60 nm.

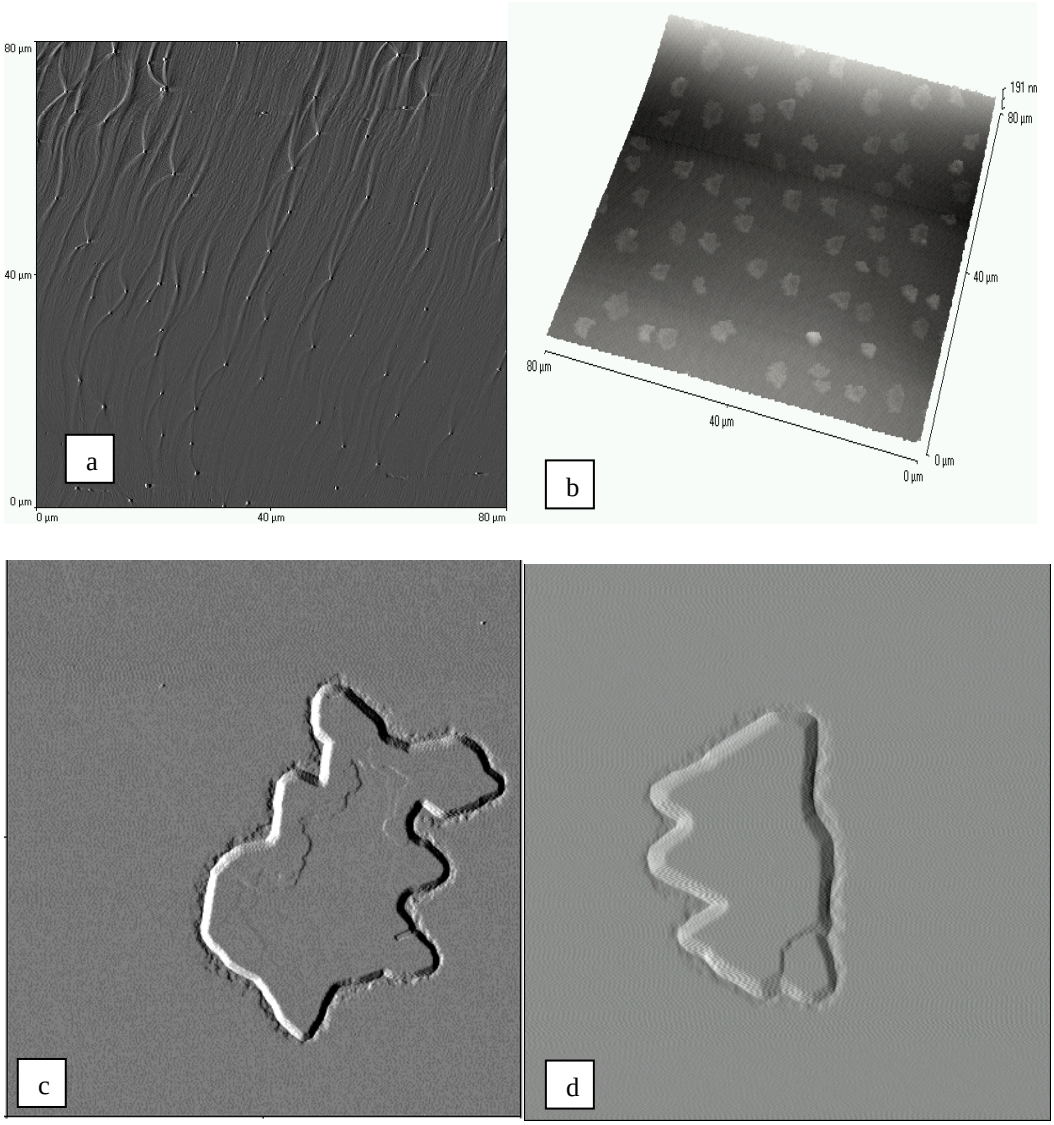

Fig. 4.7 : AFM Images after Ge deposition by CVD, Standard Sample, 750 K
(a) Exposure 95 000 L, 80 µm×80 µm, (b) Exposure 760 000 L, 80 µm×80 µm
(c) Exposure 760 000 L, Atoll Structure, 4.7 µm×4.7 µm,
(d) Exposure 760 000 L, Flat topped Polygon, 4.2 µm×4.2 µm

In both the atoll structure (Fig. 4.7c) and the flat topped polygon (Fig 4.7d) vestiges of smaller triangular shaped islands can be seen. In the atoll structure, the vestiges appear more rounded and less sharp. This could be a feature of multifaceting of the edges leading to strain release and is indicative that this is a more mature island in comparison to the flat topped polygon which still retains the sharp facets of the original islands. In addition, the small semi-

detached island at the bottom right side if the main island in Fig. 4.7d, is probably indicative of a smaller island coalescing with a larger island.

Ge on 'irradiated' Si(111) – (7×7)

STM images of the Ge layer grown on the irradiated substrate also show a Ge-(5×5) DAS (**D**imer-**A**datom-**S**tacking fault) structures (Fig. 4.8) at low exposures. At high exposures, the surface ws rough and was no longer successfully imaged by STM. These samples were then removed from the UHV system to be imaged by AFM (Figs. 4.9) in air. The AFM images of these samples show 3D island formation (Fig. 4.9a) at the lower exposures of 95 000 L and fairly rounded mature Ge 3D structures (Fig. 4.9b-c) at the higher exposures of 760 000 L.

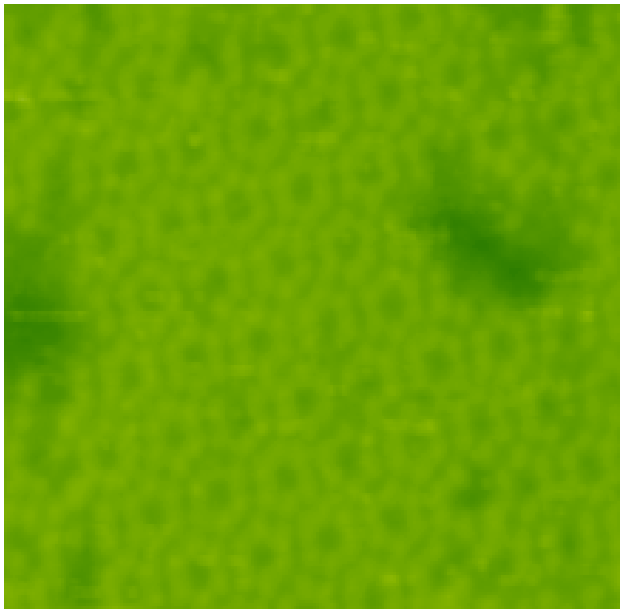

Fig. 4.8 : STM images after Ge Deposition by CVD, Irradiated sample, 750 K, 58 nm × 58 nm, 95 000 L, Ge-(5×5)

Comparison of the STM and AFM images of these samples to those grown on a standard (Fig. 4.7) Si(111)-(7×7) substrate does indicate that exposure to the XPS affects the substrate to the extent that not only is the island density of the 3D structures at similar exposures different but also the shape of the islands formed is also different (Figs. 4.9). At exposures of 760 000 L, a large number of islands are observed to have centre cavities. These islands have a more symmetrical shape as compared to those grown on a standard substrate, which are longer than they are wide (Fig. 4.7). The 3D structures have an average height of 5 nm at low exposures of 95 000 L and an average height of 80 - 100 nm at exposures of 760 000 L. It is observed that these islands are smaller in diameter but higher than those grown on a standard Si substrate. At the higher exposure the island density is more than 6.8 islands per μm^2 which is also higher than the island density on a standard substrate, grown at the same CVD conditions as described above.

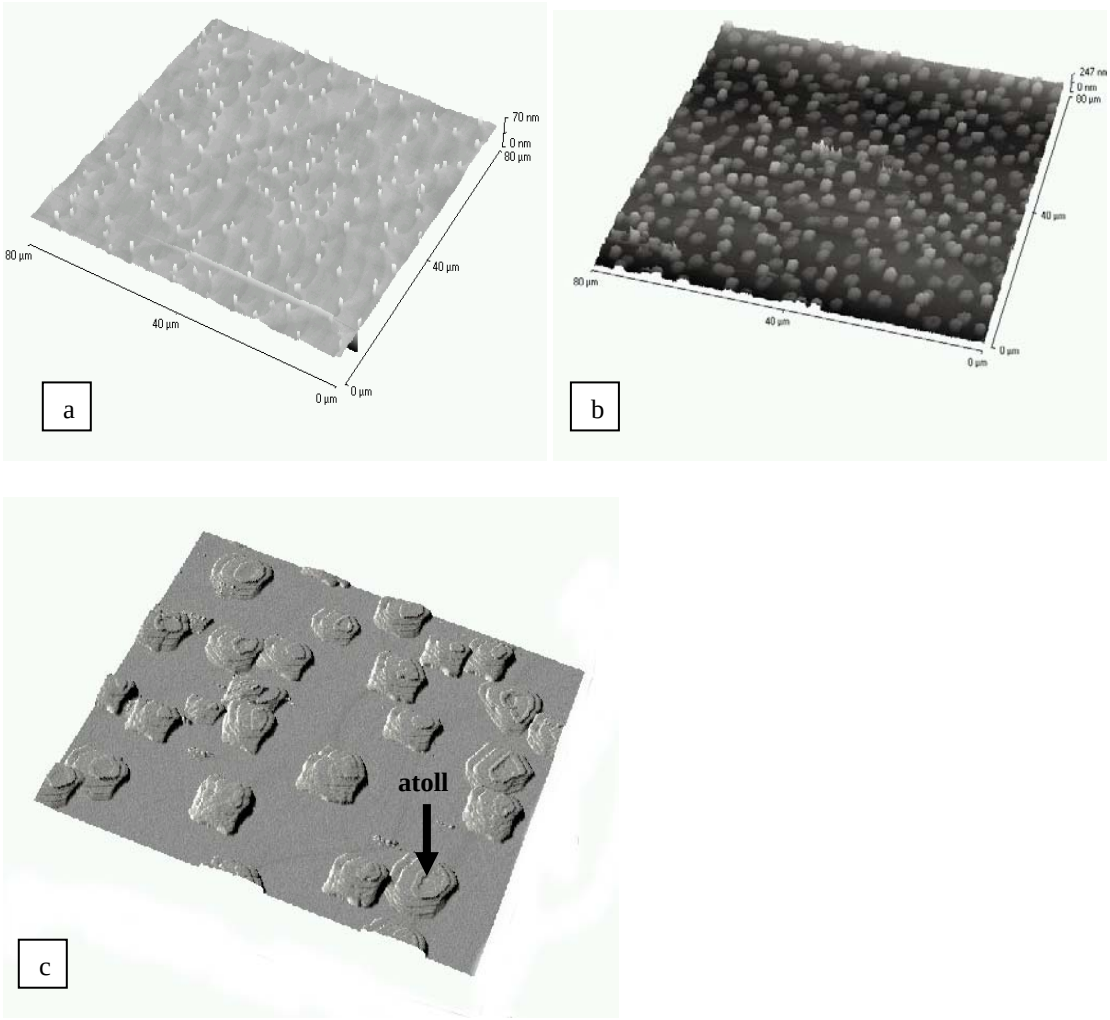

Fig. 4.9 : AFM Images after Ge deposition by CVD, Irradiated Sample, 750 K (a) Exposure 95 000 L, 80 µm×80 µm, (b) Exposure 760 000 L, 80 µm×80 µm (c) Exposure 760 000 L, 20 µm×20 µm

4.2.3 Discussion

Comparison of the STM and AFM images of the samples grown on the two different substrates does indicate that exposure to X-Rays affects the substrate to the extent that not only is the island density of the 3D structures different but the shape of the islands formed is also different.

The atoll structures (Fig 4.8c) seen in the samples have also been seen in MBE experiments carried out by Capellini et. al.[64] It was stated in this article the shape of this structure was due to 'selective depletion of the central part'. This selective depletion was hypothesized[63,64] to be due to the differences in the structural strain which is greater in the centre, than at the sides. So, the higher the strain the faster the depletion and hence the appearance of holes in the centre of the structure. Motta et.al[63]and Cappellini et.al.[64] also stated that they detected the Ge-(7×7) reconstruction at the centre of these islands.. It was deduced that this highly unusual reconstruction was induced by the residual compressive strain in the Ge layer[64,65] glancing-incidence x-ray diffraction studies[65] indicating that the 3D Ge films had a strain of

less than 0.4% as compared to the 4% strain on Ge-(5×5) on Si. Hence, the Ge-(7×7) reconstruction observed on the Ge 3D islands is considered to be relaxed[66,67]

The appearance of the flat topped polygon (Fig. 4.8d), suggests that it is not one single 3D island but an island that is a result of several smaller 3D islands which have coalesced together. The small structure at the bottom right hand side of the larger is probably such a small island in the initial stages of coalescence. In-situ TEM studies[68] of CVD growth of Ge on Si(111) using digermane as a precursor gas, have suggested that although small 3D island do indeed coalesce together to form larger structures, further island growth is a more complicated process. These studies have theorised that when two small strained islands are close together, a region of very high strain (which is like a 'coreless dislocation') is formed between these islands as they coalesce together. As the area located near the smaller island is denuded of Ge atoms, this locale acts as a preferential site for further nucleation and new small strained islands are formed in close proximity. As the island grows larger by repetitive coalescence, the shape of the large island changes in order to reduce strain and surface energy. Hence, it has been stated in the literature that the flat topped polygon is the strained precursor island and the atoll structures, the strain relaxed islands[63,64].

So, the mechanism of the large 3D structure formation in the standard sample is as follows. Initially, small 3D islands are formed. These eventually merged together to form larger strained islands. These strained islands undergo selective depletion at the centres to release the strain and formed the relaxed atoll structures as evidenced by the presence of the relaxed Ge-(7×7) reconstruction.

The structures observed on the irradiated sample are much smaller in comparison to those observed on the standard sample. Furthermore, as seen in Fig. 4.9c, even when the individual islands grow together in close proximity, they still retain their discrete shapes. This suggests that in the case of the irradiated sample, the widespread coalescence of smaller islands does not occur. The shape of these structures is also more regular in comparison and resembles a stepped mound. Some of these stepped structures have a central depression (atoll) which is probably indicative of strain release[63,64]. The shape and size of the islands formed on the irradiated substrate resembled the more discrete islands (atoll and flat topped pyramidal or multifaceted islands) formed in deposition studies by MBE[63,64]. From previous work carried out by J.Braun et. al.[11,12] these islands were initially formed as square pyramids. This was followed by multifaceting[11,12] to release the stress of island formation and eventually the islands matured to form the more rounded islands with the central cavity (Fig. 4.9) that have been observed in this work.

4.3 TEM Characterisation of 3D Ge growth by CVD Si(111)-(7×7)

4.3.1 Introduction

STM images indicated a high surface roughness at higher GeH_4 exposures and subsequent AFM images indicated the presence of a high 3D island density for the irradiated samples. Cross-sectional TEM imaging was carried out on samples with low and high GeH_4 exposures in order to characterise the Ge-Si interface.

4.3.2 Sample Preparation

The CVD samples used for the TEM images were as prepared under Section 4.2.1. Two samples were selected for imaging, one at a low exposure of 140 000 L and the other at a high exposure of 760 000 L. Both were from the lot of samples which have been irradiated prior to deposition. In addition, a standard sample with an exposure of 760 000 L was also sent for TEM imaging. The TEM sample preparation and imaging was carried out by Prof. F. Banhard* at the Centre for Electron Microscopy.

4.3.3 Results

Ge on standard Si(111) – (7×7)

The cross-sectional (across the length of the islands) TEM images show that the islands are long and two types of islands are observed as in Section 4.2 (Fig. 4.7c & d), the atoll (Fig. 4.10a) and the flat topped polygon (Fig. 4.10b).

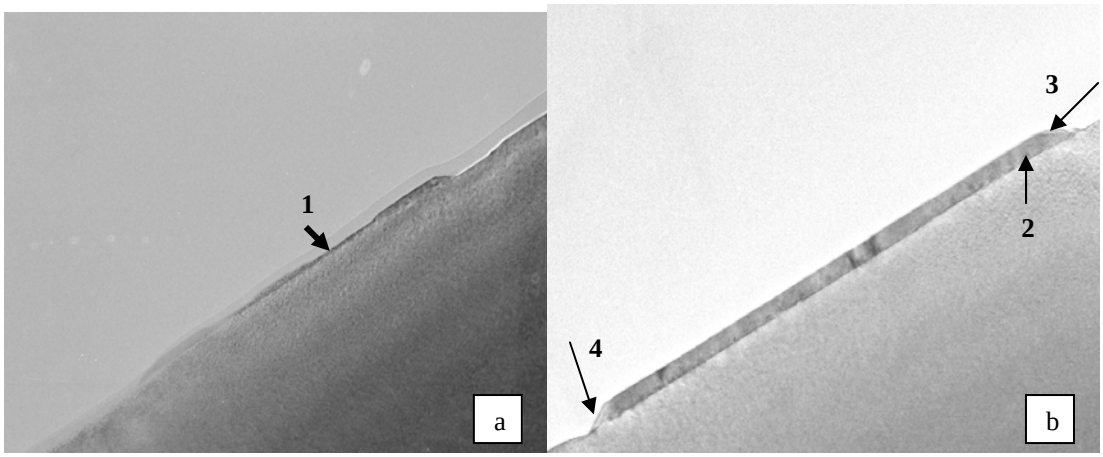

Fig. 4.10 : Cross-sectional TEM images, Standard Sample, 760 000 L :
(a) Atoll Structure, (b) Flat topped Polygon

In Fig. 4.10a, the arrow (1) indicates the cross-sectional TEM image of the central depression observed in the atoll structures (Refer to AFM image, Fig. 4.7c). A HRTEM image of this central depression is depicted in Fig. 4.11a. In this figure (4.11a) the lighter grey part at the lower half of the image is the silicon substrate, while the grey part on the top left of the image is the background. The darker stripe in the middle portion of the image is the germanium 3D island. The arrow marked `1` in Fig. 4.11a shows the beginning of the central depression. A closer look of this area is shown in Fig. 4.11b. The arrow marked ´1` in Fig. 4.11b shows a misfit dislocation which is found at the onset of the depression, 8 layers from the bottom of the island. Besides the first 2-3 layers (from the bottom of the island which contains most of the misfit dislocations, the rest of the layers in the central depression in the atoll structure are observed to be defect free.

The arrow marked `2` in Fig.4.11a shows the location (dark stripe) of a series of dislocations located at the higher part of the atoll structure. This series of dislocations affect 2-3 rows and are to be found 5 layers from the bottom of the island. Other series of dislocations are to be found towards the outer edge of the island. These dislocations involving rows of up to 5-6 layers are to be found at the first 5-6 layers of the island. These observations indicate that in the atoll structure, most of the defects are found in the outer, higher part of the island, while

the central part of the atoll is defect free except for the first 2-3 layers and at the onset of the depression.

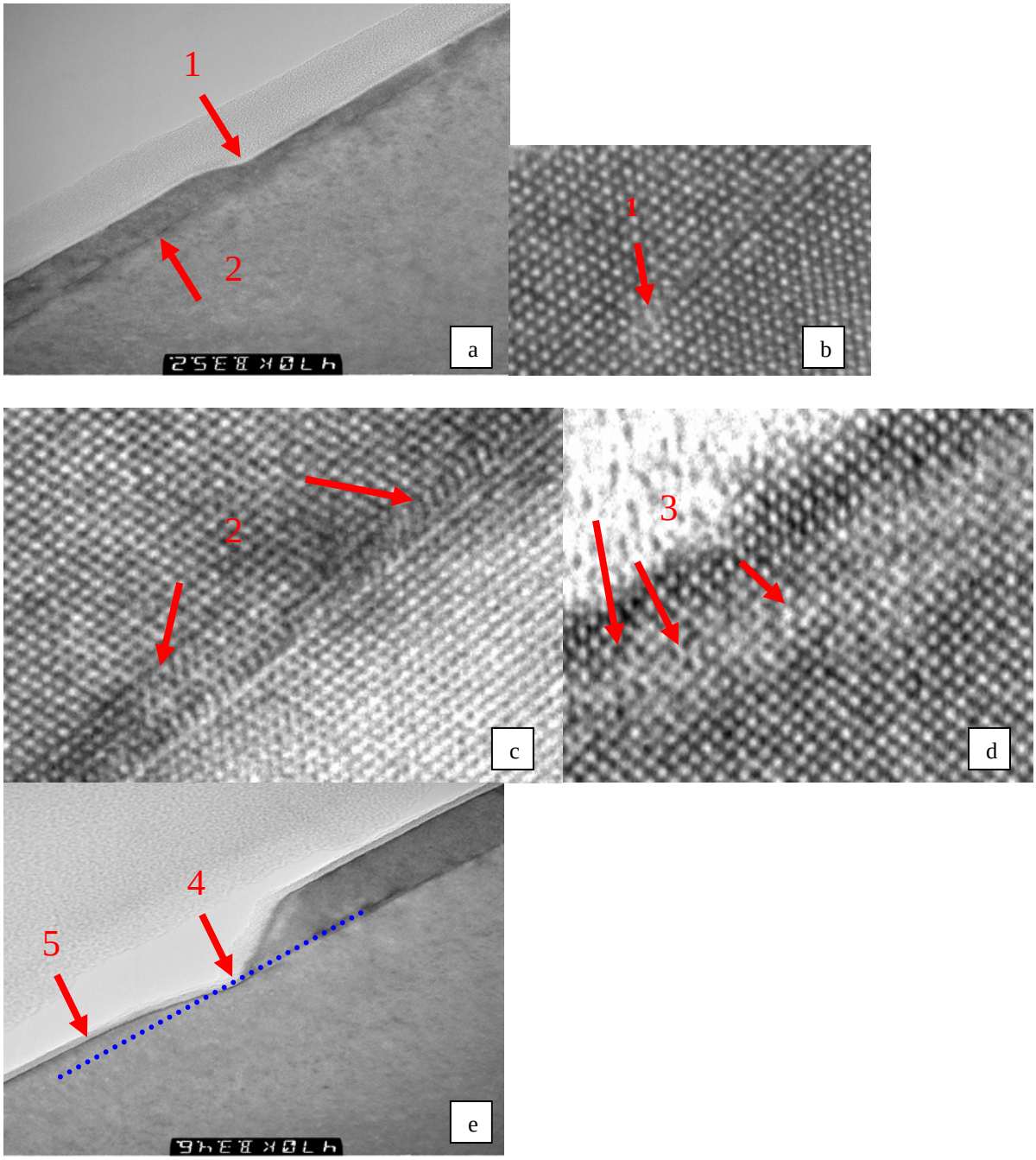

Fig. 4.11 : Cross-sectional HRTEM images, Standard Sample, 760 000 L :
(a) Atoll Structure, close up of region 1 from Fig. 4.10a,
(b) Atoll structure close up of region 1 from Fig. 4.11a,
(c) Flat topped Polygon close up of region 2 from Fig. 4.10b,
(d) Flat topped Polygon close up of region 3 from Fig. 4.10b,
(e) Flat topped Polygon, region 4 from Fig. 4.10b

The flat topped polygon (Fig. 4.10b) has a series of dislocations running along the first 2-3 rows from the interface across most of the length of the island. The locations at some points are 3-5 layers thick (arrow `2´ in Fig. 4.10b) and this is shown in Fig. 4.11c (arrow ´2`). In addition dislocations are also present at the edges of the island (arrow `3´ in Fig. 4.10b). A close up of these defects can be seen in Fig. 4.11d (arrow ´3`).

The TEM images (Fig. 4.10b and 4.11e) also confirm the presence of trenches. The trench is marked out by the arrow labelled `4´ in Fig. 4.11e. A close observation of this HRTEM image shows that the base of the 3D islands to be about 12 layers below the normal SiGe interface (Fig. 4.11e). The arrow labelled `5´ in Fig. 4.11e shows the SiGe interface. The dark line represents the initial layer by layer growth of germanium is about 2 layers thick.

The lattice mismatch of the atoll structure and the flat topped polygon is calculated from HRTEM images (Fig. 4.11 a and e) according to the following criteria :

$$\% \text{ mismatch} = \frac{a_{Ge} - a_{Si}}{a_{Si}} \times 100$$

where a_{Ge} and a_{Si} are the lattice constants of germanium and silicon respectively.

The lattice mismatch of the atoll structure is calculated to be 3.13% at the side of the island and 1.88% at the central cavity while that of the flat topped polygon is 3.75%. This indicates that the atoll structure is more relaxed than the flat topped polygon. In addition, the central depression of the atoll structure is more strain relaxed than the sides of this type of island.

Ge on 'irradiated' Si(111) – (7×7)

Fig. 4.12a is a HRTEM image of a germanium island formed at a low GeH_4 exposure of 140 000 L. The island seen in this image (Fig. 4.12a) has a height of about 22 layers with a flat SiGe interface. HRTEM image of the interface (Fig. 4.12a) shows the presence of a wetting layer consisting of two bilayers[7]. In this island, 3-4 rows dislocations have been observed midway up at the edges of the island. This can be seen in Fig. 4.12b which is a grazing angle view of the close up of the region marked in the box in Fig. 4.12a.

The cross-sectional TEM image (Fig. 4.13) of islands grown at the high exposure of 760 000 L show these island to be discrete islands (refer to AFM image, Fig. 4.9 b,c). The HRTEM micrographs of these islands are shown in Fig. 4.14 and 4.15. Fig. 4.14 is a HRTEM image of a 3D island with a rounded facet. The arrow labelled `1´ in Fig. 4.14a shows a horizontal row of dislocations of 3-4 layers located at the bottom third of the island. These dislocations are similar to those observed in the islands formed at the lower exposure of 140 000 L, and are found at around the same location from the edge of the island and from the interface. A close up view of the interface (box in Fig. 4.14a) is shown in Fig. 4.14b.

In comparison to the interface at the lower exposure of 140 000 L (Fig. 4.12a), the interface at the high exposure of 760 000 L (Fig. 4.14b) is no longer flat. The interface in Fig. 4.14b appears to be ´rounded´ in some areas. These rounded areas appear to be small 3D islands which are growing in close proximity to the larger islands.

Fig. 4.15a shows a 3D island with a sharp facet. In addition to the horizontal dislocations formed at the lower part of the island, this island also has a vertical dislocation (Fig. 4.15b) at the location shown in the box in Fig. 4.15a. This type of dislocation has not been observed in the more rounded island (Fig. 4.14) nor on the islands grown on a standard substrate (Fig. 4.10-11).

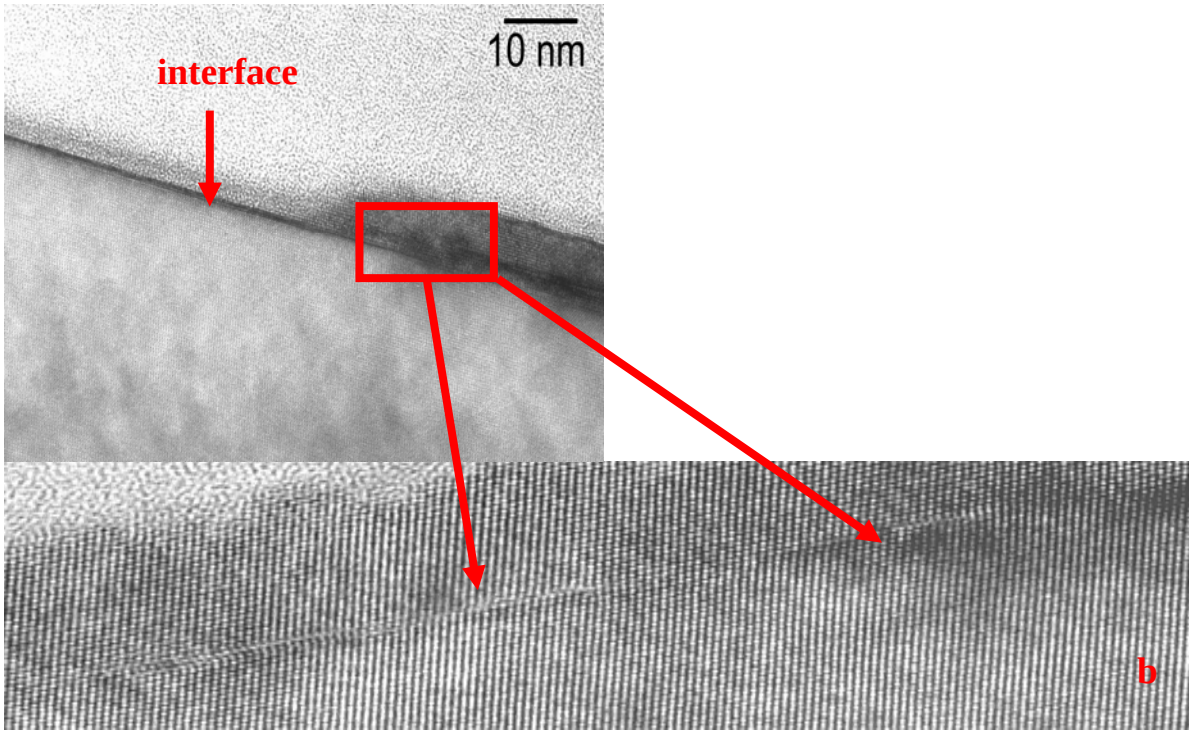

Fig. 4.12 : Cross-sectional HRTEM Images, Irradiated Sample, 140 000 L
(b) Ge Island, (b) Misfit dislocation (grazing angle view)

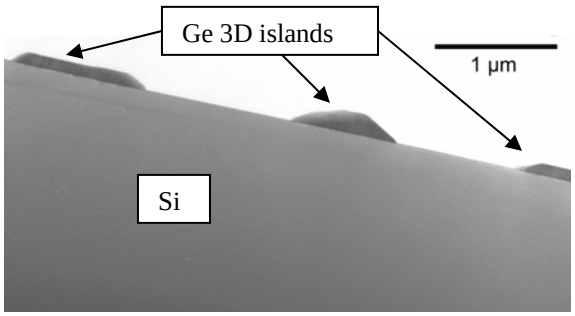

Fig. 4.13 : Cross-sectional low resolution TEM Image, Irradiated Sample, 760 000 L

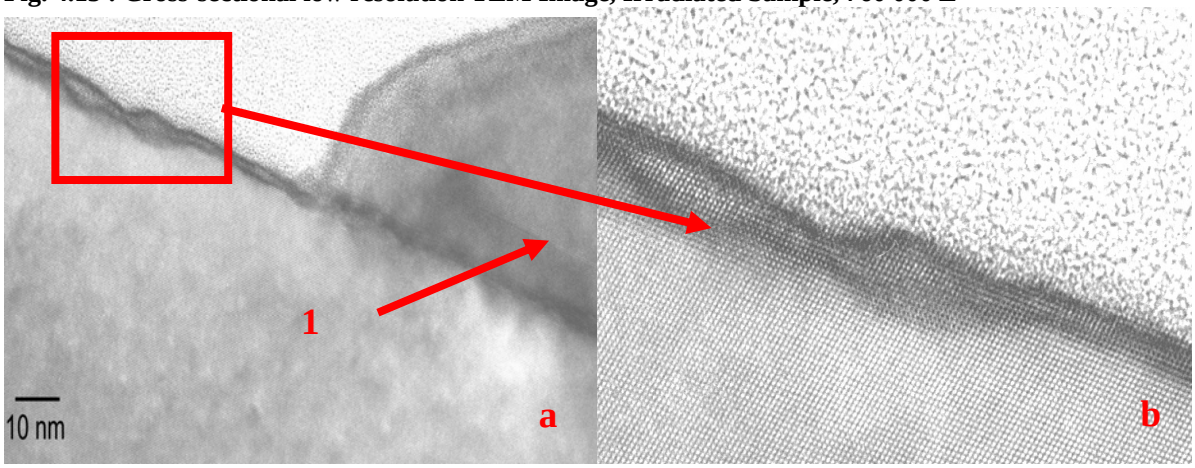

Fig. 4.14 : Cross-sectional HRTEM Images, Irradiated Sample, 760 000 L
(a) Ge Island, (b) Ge/Si Interface

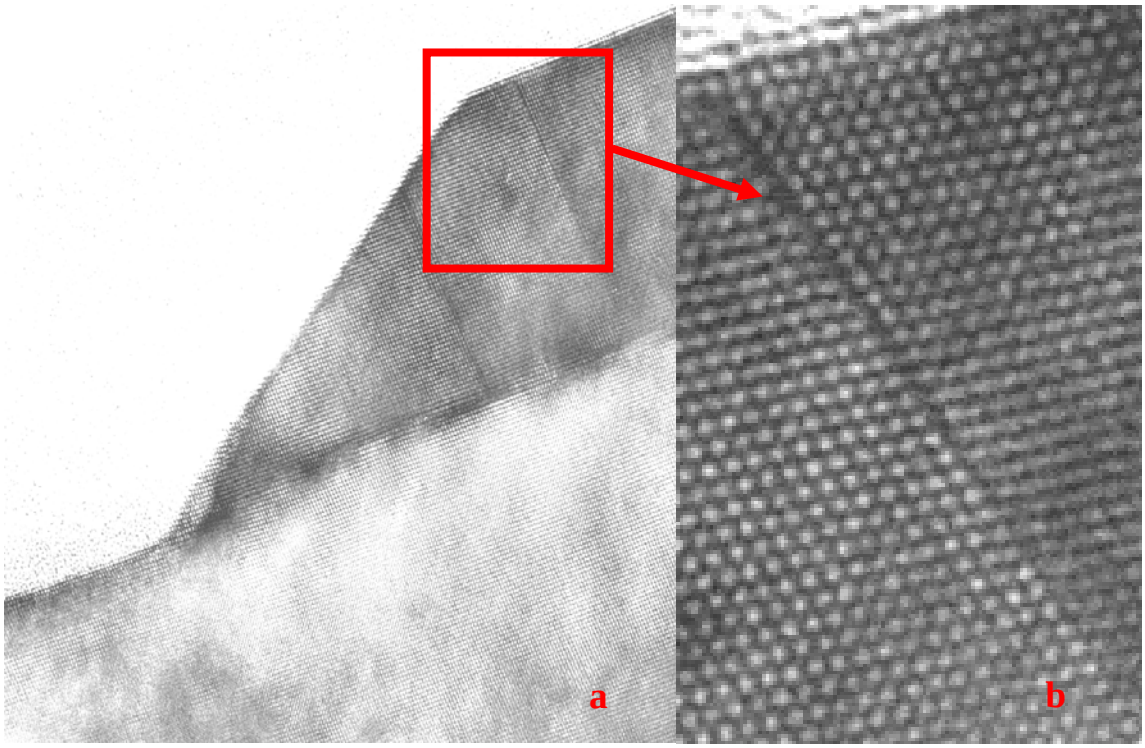

Fig. 4.15 : Cross-sectional HRTEM Images, Irradiated Sample, 760 000 L
(a) Ge Island, (b) Dislocation magnified

In contrast to the islands grown on the standard Si(111) – (7×7) substrate (Fig.4.10-11), no trenches have been observed around the islands (Fig.4.13-15) grown on the irradiated Si(111) – (7×7) substrate.

4.3.4 Discussion

Ge on standard Si(111) – (7×7)

HRTEM image (fig. 4.11e) of the interface indicates the presence of a wetting layer consisting of two bilayers[64]. The TEM images confirm the presence of trenches around the islands (Fig. 4.10b, 4.11e) and the islands formed on the substrate are observed to be sunken (Fig. 4.11e). Initial strain release is via the series of well known dislocations (Fig. 4.11c) which have been observed after the wetting layer. Dislocations have also been observed at the sides of the islands (Fig. 4.11d). For the atoll structures, dislocations are also observed at the onset of the central depression (Fig. 4.11b) i.e. between the sides and the centre of the island. The top layers of the centre of the atoll structure are observed to be defect free. From the HRTEM images, the lattice mismatch of the flat topped island is calculated to be 3.75% (Fig. 4.11e), while for the atoll structure, the mismatch is 1.88% at the centre and 3.13% at the side of the island (Fig.4.11a). These findings indicate that the atoll structures are strain relaxed in comparison to the flat topped polygon. The findings also indicate that the centre cavities in the atoll structure are strain relaxed in comparison to the sides of the same structures.

A feature that is observed on the AFM images of 3D islands formed at high exposures is trench formation (Fig. 4.7c,d). Cross-sectional HRTEM images (Fig. 4.11e) of the islands not only confirmed the presence of these trenches but also indicated that the Ge/Si interface at the island is shifted downwards until it is level with the bottom of the trench (Fig. 411e). This suggests that a diffusion of Si from the substrate into the Ge islands had taken place[70-72].

Trench formation has been reported on Ge structures grown by MBE on Si(100)[69], Ge structures grown by CVD and MBE on Si(001)[7,70,73,74], MBE grown Ge on Si(111)[75] and on MBE grown Ge on Si(113)[7]. It had been suggested that the formation of the trench was a consequence of strain energy[7,69,72,76-80] difference between the wetting layer and the islands. This energy difference acted as a driving force that drove the material flow from the substrate and into the islands causing a gradual erosion of the wetting layer around the island. This diffusion leads to the lowering of the Ge/Si interface in the island.

Ge on 'irradiated' Si(111) – (7×7)

TEM images of these structures shows the absence of trenches (Fig. 4.13, 4.14a, 4.15a), which are observed for the standard growth[7,72]. Instead it is observed that at higher exposures, the SiGe interface is warped (Fig. 4.14a,b). The warping is observed to extend into the substrate itself. However, the large 3D islands are not observed to sink into the substrate, which is a feature that is observed with islands grown on standard substrates. Cross-sectional TEM images of the islands grown at the lower exposure of 140 000 L (Fig. 4.12a,b), indicate the presence of dislocations after the initial wetting layers. At higher exposures (760 000 L), these initial dislocations (Fig. 4.14a) are also observed at around the same locations in the island with respect to the edge and the interface. On an island with a straight facet, a vertical dislocation which has its core at the centre of the island and which runs almost to the top, has been observed (Fig. 4.15a,b). The TEM images indicate that as compared to Ge growth in a standard Si substrate, dislocations are formed in the small islands grown at low exposures. The strain relaxation which subsequently occurred, is likely to facilitate the rapid growth of the Ge 3D islands.

4.4 Summary

The results indicate that at the given growth conditions[11,12], Ge growth on a standard Si(111) –(7×7) does not follow a self limiting layer by layer growth but by the well described S-K growth, with the formation of 3D islands. The mechanism of the formation and ripening of these Ge islands on the standard Si(111) substrate, grown by CVD is a complex process. This involves nucleation and coalescence of islands, dislocation formation, intermixing and trench formation. Initially, the two dimensional wetting layer grows layer by layer, relatively rapidly (Fig.4.4). This is followed by the onset of small 3D islands at about 95 000 L. These grow larger at higher exposures and where two small islands are in close proximity, they coalesce together to form larger strained islands. The resulting strain energy difference between the substrate and the islands drives the diffusion of Si from the substrate into the Ge islands, leading to an erosion of the wetting layer around the islands. At the same time these strained islands undergo selective depletion at their centres to release the strain and form the relaxed atoll structures.

Although the growth of the initial two dimensional wetting layer on the irradiated substrate is similar to that of the standard sample, the 3D Ge island growth morphology on the irradiated substrate does not follow the same path as that of the standard substrate. Here it is suspected that initially various nucleation zones are formed on the substrate and although 3D islanding

proceeds via dislocation, vertical growth on these nucleation zones, instead of island coalescence predominates resulting in smaller but higher islands, as well as a larger island density as compared to Ge growth on a standard Si(111) substrate. The cause of this effect has been investigated and will be discussed in the next chapter.

* Now at the Institut für Physikalische Chemie, Johannes Gutenberg-Universität Mainz , Welderweg 11 55099 Mainz, Germany

Chapter 5

Identification of the causes of XPS induced 3D growth of Ge on Si(111) –(7×7)

5.1 Introduction

It is known that the incorporation of carbon[81,82] in silicon-germanium based transistors leads to better strain adjustment and hence increased capability for band gap engineering making it possible to build devices with a higher performance. Hence, there has been an interest in the study of the effects carbon incorporation into the silicon-geramnium crystal[81,82] as well the formation of carbon defects in the silicon crystal[83,84]. C_s/C_i defects[83-89] are a type of carbon defect known to be created during an electron irradition of the Si surface at about 1.5-2.5 MeV. During this electron bombardment, the interstitial carbon[83-87] atoms in the bulk gain sufficient energy to move through the silicon matrix. During the journey through the matrix, some of these carbon atoms are captured by the substituitional carbons trapped within the matrix itself, hence forming the substituitional carbon-interstitial carbon pairs. As these carbon atoms are within the bulk of the substrate, to date literature has reported that only hard radiation has generated these defects. Reports by J. Braun et al[11,12] has indicated that these defects may also be generated by soft X-rays and these have influenced the Ge CVD under certain growth conditions.

In this chapter, the result of the investigation that has been carried out to determine if C_s/C_i defects are generated by soft X-rays will be presented. In additional, the results of the experiments that have been carried out to elucidate a possible cause for the change in growth morphology of the three dimensional germanium structures (refer to chapter 4) that are grown by CVD on a Si(111)-(7×7) substrate that has been irradiated by soft X-rays as compared to those grown on a standard Si(111)-(7×7) substrate are also presented.

5.2 Photoluminescence Experiments

5.2.1 Introduction

In a previous work by J. Braun et. al.[11,12], where Ge 3D structures have been grown by CVD on Si(111), PL measurements on the Si(111)-(7×7) substrate have indicated the presence of a 'G'-peak only on the Si(111)-(7×7) substrate (Fig. 5.1a) that have been irradiated for 30 mins by the soft X-rays from a 300 W XPS source. As the 'G'-peak in PL Spectroscopy is

associated with C_s/C_i pair defects[88,89] (Fig. 5.1b), this led to the hypothesis[11,12] that irradiation by X-Rays generates the C_s/C_i pair defects[83-87] (Fig. 5.1b), which led to a relaxation of the strained lattice and hence Ge 3D growth is achieved. Hence PL measurements have been carried out on the standard and irradiated Si(111)-(7×7) substrates to re-confirm the presence of the 'G'-line.

Experiments which have been carried out as part of this project, (refer to Chapter 4) also indicate that 3D growth is observed even on the standard samples even though the Ge 3D structures are markedly different.

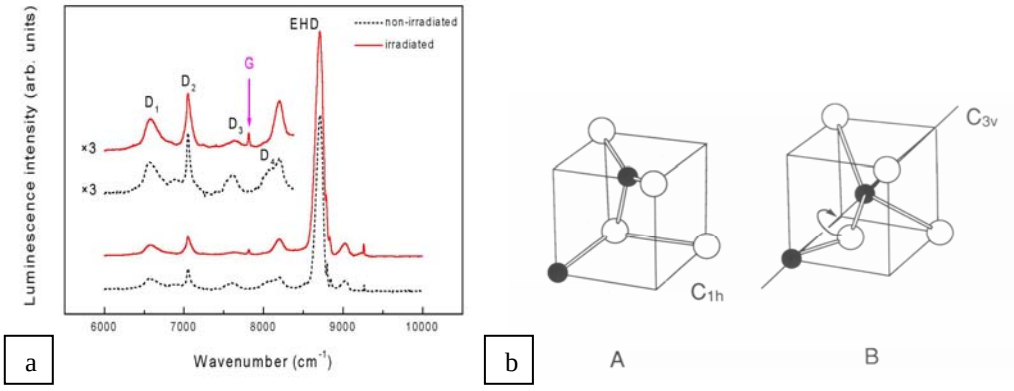

Fig. 5.1 : (a) PL Spectra, (b) C_s/C_i pair defects (both reproduced from Reference [12])

5.2.2 Preparation of samples for PL measurements

The standard and irradiated Si(111)-(7×7) substrates have been prepared as described in 4.2.2. These substrates have been then brought over to the Department of Semiconductor Physics. The PL measurements have been carried out by Michael Haupt.

5.2.3 Results

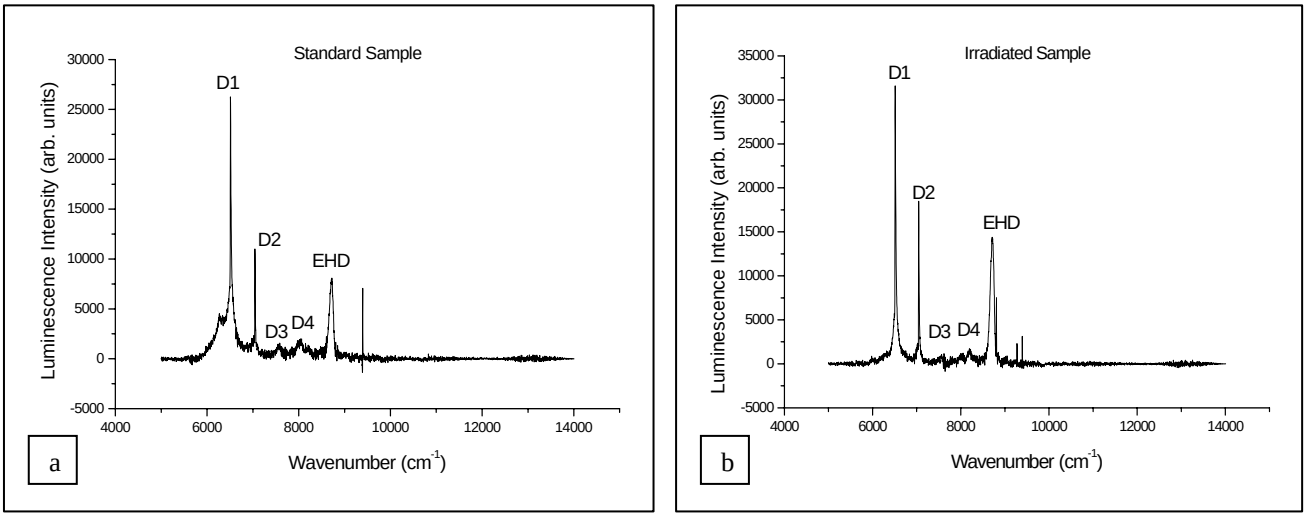

Fig. 5.2 : PL Spectra of (a) Standard Si Substrate, (b) Irradiated Si Substrate

The PL spectra (Fig. 5.2) of both the standard and irradiated substrates show the characteristic D1 to D4 lines associated with reconstructed silicon. The D1 and D2 lines are assigned to be due to relaxation dislocations at the surface and the D3 and D4 lines are due to bulk relaxation dislocations[90]. All 4 lines are typically seen on a reconstructed Si substrate. However, it can be observed that there was no additional 'G'-line[88,89] on the irradiated substrate.

5.2.4 Discussion

The PL spectra (Fig. 5.2) of both standard and irradiated substrates only display the features that are associated with a reconstructed silicon substrate. It is of interest to note that in the PL spectrum of the irradiated substrate the 'G'-line is conspicuously absent even though this experiment has been repeated twice. This leads to the conclusion that irradiation by soft X-Rays did not create C_s/C_i pair defects in the silicon wafer samples that are used for these experiments. However the fact that in spite of the absence of these defects, the exposure to X-Rays still led to the promotion of Ge 3D growth indicates that there is some other mechanism at work that promotes the 3D growth on a Si(111)-(7×7) substrate that has been previously exposed to soft X-Rays. Hence it is of interest to determine the actual cause of the altered growth morphology[91] after the silicon surface has been exposed to XPS prior to deposition[92,93].

5.3 Shielding

5.3.1 Introduction

Since the results of the PL experiments in section 5.2 rule out the creation of C_s/C_i pair defects after exposure the soft X-rays from the XPS, and hence rule out the hypothesis stated in Ref. 14, investigations set out to determine the actual cause of the altered growth morphology naturally focused on the XPS itself as the change in morphology occured after exposure to the XPS. As a start an experiment is envisioned where only half of the sample will be exposed to the XPS. The other half is shielded from the soft X-rays from the XPS source. The whole sample will then be subjected to the same CVD conditions as stated in Chapter 4. If the soft X-rays emanating from the XPS are directly responsible (as in direct creation of defects) for the altered growth morphology, then only on half of the sample (unshielded half) will Ge 3D growth be observed under CVD conditions in Section 4.2. On the other half (shielded), the surface will appear as in Fig 4.1. The shield effect described is schematically represented in Fig. 5.3.

5.3.2 Experimental Procedure

In order to test the effect of irradiation by the AlK_α source of the XPS a shield is designed such that half of the sample will be screened from soft X-rays emanating from the XPS. The shield is cut out of a 50 μm molybdenum sheet, the same material as the sample holder, as Mo is sufficiently non-reactive for the Ge and SiGe CVD processes that are studied.

The thickness of the shield is selected such that more than 99.99% of the AlK_α radiation[94] is absorbed by the Mo sheet and the shield is the same shape and size as the sample holder (Fig. 5.4). As the Ge CVD growth is sensitive to surface contamination (especially metals), the shield has been cleaned by boiling in concentrated HCl for 10 minutes to remove any reactive metallic contamination. It is then rinsed in DI water and then cleaned in acetone followed by

methanol with 15 minutes of sonic agitation each. The shield is introduced into the main chamber via the loadlock. When required the shield has been placed into the clamp of the XPS manipulator prior to irradiation, such that although it shields the sample from the soft X-rays, it is not in contact with the silicon sample. The silicon sample preparation and the Ge CVD are carried out as described in Chapter 4. AFM measurements on both halves of the sample are then carried out ex-situ in air.

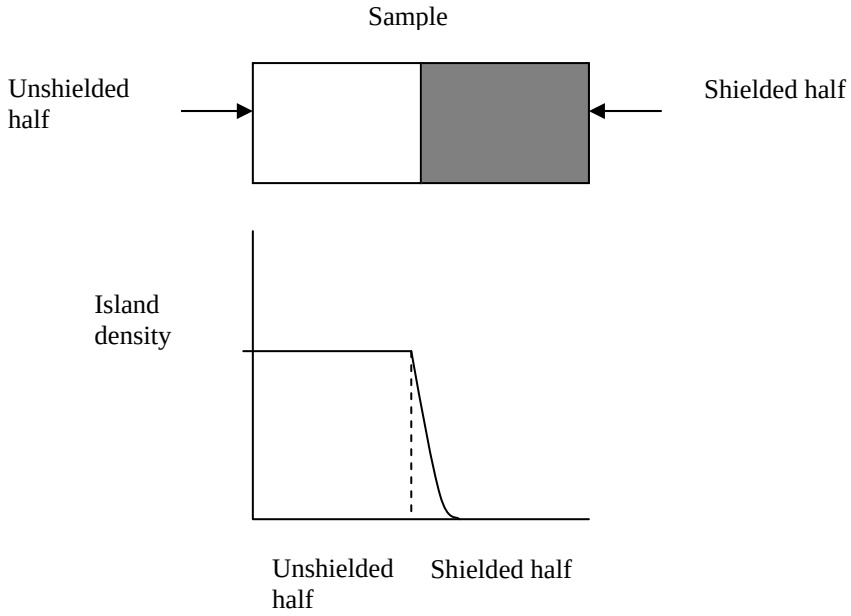

Fig. 5.3 : Schematic Representation of Island Density due to the shielding effect

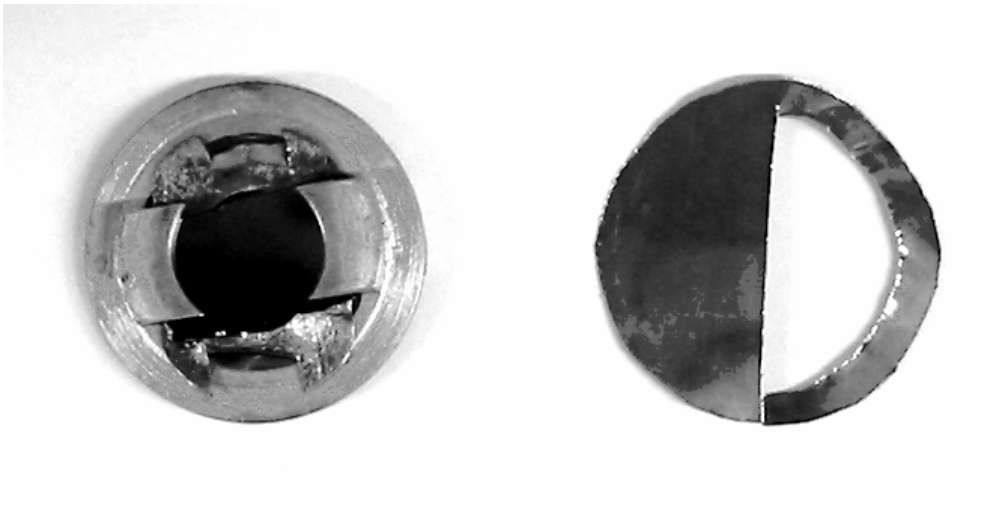

Fig. 5.4 : Mo Shield and Sample

5.3.3 Results

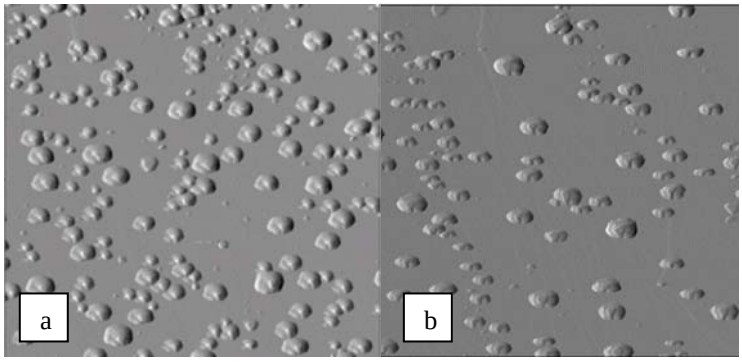

Fig. 5.5 : 5 μm×5 μm AFM images after 30 min Ge CVD at 750 K, 7×10^{-5} mbar
(a) Area exposed to x-rays (b) Area unexposed to x-rays (shielded half)

The AFM images of the surface which has been subject to a germane deposition via CVD for 30 min at 750 K and a deposition pressure of 7×10^{-5} mbar, show the presence of the same type (small strained islands) 3D Ge structures on both halves of the sample. The difference is in the island density. On the unshielded half (Fig. 5.5a), the island density is 5.6 μm^{-2}, whereas the island density on the shielded half is 3.2 μm^{-2}.

5.3.4 Discussion

Although at first sight the results are unexpected, they are not entirely surprising. As stated earlier, if the soft X-rays generate the C_s/C_i defects, then, 3D growth will only be expected to occur on the part of the sample that is exposed to the X-rays and only layer by layer growth with the onset of islanding will be observed on the shielded part. However the results of this experiment show the same type of 3D island growth on both halves with only a difference in island density. This suggests the presence of a gaseous contamination on the surface of the substrate that has been adsorbed on the surface prior to deposition. In order to rule out that the contamination is from the shield itself, the next experiment, the Offset Exposure is carried out.

5.4 Offset Exposure

5.4.1 Introduction

This experiment is designed to test if any outgassing products from the source of the XPS has any influence on the morphology of the island growth and if the influence results in structures which are similar to those described in Chapter 4. Hence the sample (without Mo shielding) is located such that it is not exposed to the x-rays emanating from the XPS but will be exposed to any outgassing from the XPS source.

5.4.2 Experimental Procedure

The sample is prepared by the flash and reconstruction cycle as described in Appendix III. After the sample has cooled down, it is moved into the clamp of the manipulator. The manipulator is then moved such that the sample is not placed in the path of the soft X-rays but in the path of any outgassing products from the XPS source. Hence with reference to Fig. 3.2,

it is placed just above the outlet to the ion pump and the TSP (position 10 in Fig. 3.2). The XPS gun is then turned on and the sample remains in the specified position for 30 min, which is the equivalent exposure time to the 'irradiation' experiment in Chapter 4. After the exposure to the XPS, the sample is moved to the Wehnelt and GeH_4 CVD is carried out for 30 min at a pressure of 7.0×10^{-5} mbar and at a deposition temperature of 750 K. The sample is allowed to cool after which it is removed from the UHV system for ex-situ AFM imaging in air.

5.4.3 Results

The AFM image above (Fig. 5.6) of the sample which has been exposed to the outgassing from the XPS source prior to Ge CVD indicates the growth of small strained Ge 3D islands. These islands are similar in appearance to those islands[91] grown on the 'irradiated' substrate characterised in Chap. 4. The average size of the islands is about 0.5 μm and the island density is about 13.6 islands per μm^2.

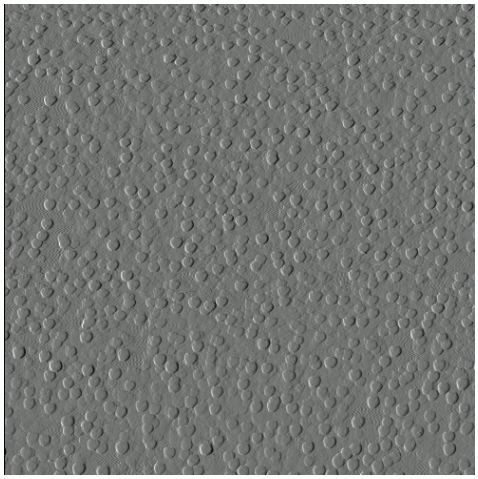

Fig. 5.6 : 20 μm × 20 μm AFM image after exposure to XPS outgassing, followed by 30 min Ge CVD at 750 K, 7×10^{-5} mbar

5.4.4 Discussion

The results of the offset experiment indicate even though the sample is not exposed to soft X-rays, the morphology of the island growth changes when the sample has been placed in close proximity to the XPS gun, when it has been turned on. This suggests that there is an outgas from the XPS gun that adsorbs onto the sample surface and hence influences island growth. Therefore the next set of experiment is set up to investigate the nature of the outgas from the XPS gun.

5.5 QMS of the Outgassing from the XPS

5.5.1 Introduction

As it is suspected that the outgas from the XPS gun influences the growth morphology, the QMS is used to determine the nature of the outgas from the XPS.

5.5.2 Experimental Procedure

In order to identify the products of the outgas, the QMS of the constituents of the UHV chamber are recorded at both high and low gains (baseline MS). The QMS is taken at low gain so as to record the nominal levels of hydrogen in the system, as the high hydrogen background saturates the signal at high gain which is used to record the levels of species which are present at very low concentrations. The QMS is then recorded with the XPS system and the ion getter pump in operation and then with the XPS system in operation but the ion getter pump turned off.

5.5.3 Results

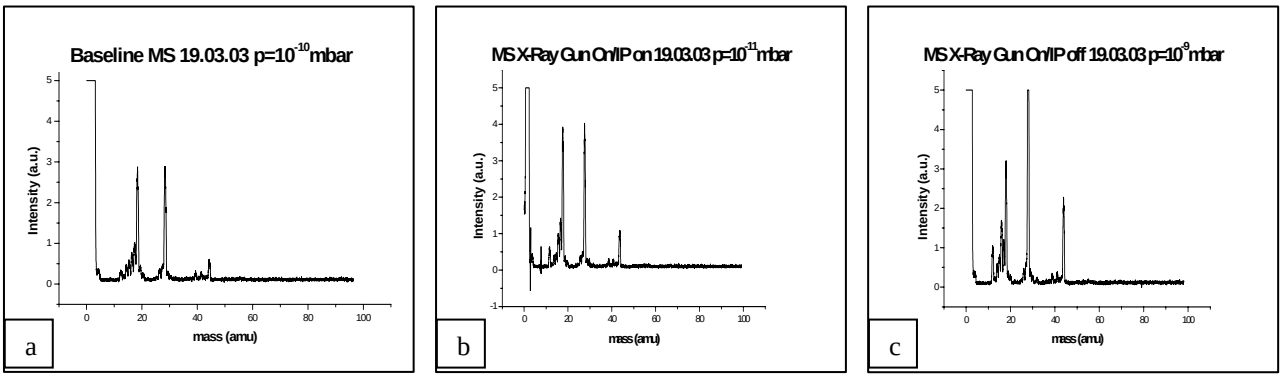

Fig. 5.7 : QMS at high gain (a) Baseline (b) X-Ray gun On/IP on (c) X-Ray gun On/IP off

The QMS (Fig. 5.7 and 5.8) indicates that there is outgassing from the XPS source. This is more clearly seen in the QMS when the ion getter pump is turned off (Fig. 5.7c).

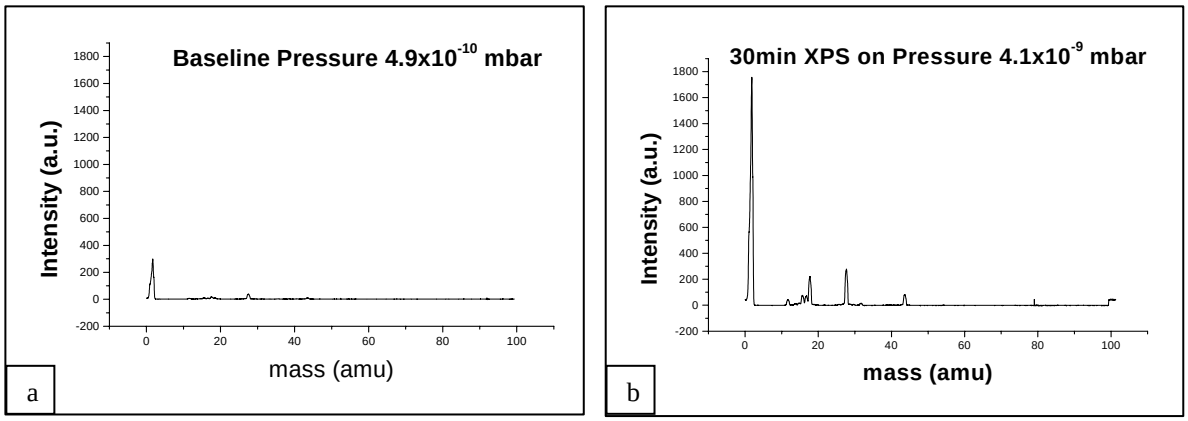

Fig 5.8 : QMS at low gain (a) Baseline (b) XPS gun On for 30 min

The main constituents of the outgas are hydrogen, CO_2 and CO.

5.5.4 Discussion

The results clearly indicate a high level of outgas from the XPS source, even though not only the UHV system is pumped by an ion pump but the XPS source is also pumped by its own ion pump. It is clear that a flash cleaned and reconstructed Si(111)-(7×7) is highly susceptible to re-contamination by adsorption from any outgassing due to the nature of the dangling bonds on the surface of the silicon. Hence if this is the case there will be a difference in the STM images after the surface has been exposed to the outgassing from the XPS. The STM images

will then show dark spots after exposure to the XPS due to the quenching of the dangling bonds.

5.6 GeH_4 CVD at Ambient Temperature

5.6.1 Introduction

In the previous sections, it is established that there is indeed outgassing from the XPS source. This outgassing is detected despite the fact that both the UHV system and the XPS are pumped by ion pumps. It is also clear that the outgassing reaches the surface of the sample and is adsorbed onto the surface. As any species adsorbing onto the silicon surface do so at the dangling bonds, the STM is used to image the surface after the surface has been exposed to the XPS. It is expected that with adsorption, the dangling bonds will appear as dark spots when the appropriate tunnelling voltage is applied. In addition, GeH_4 CVD is carried out on the exposed sample at ambient temperature in order to image the effect of the adsorbed species.

5.6.2 Experimental Procedure

STM images of the Si(111)-(7×7) surfaces are taken at 3 different bias voltages of +1.0V, +2.0V and -2.0V, of the clean substrate, the 'irradiated' substrate and after the substrate has been exposed to 8000 L of GeH_4 at room temperature.

5.6.3 Results

Fig. 5.9 shows the STM images of the silicon surface obtained under different tunnelling voltages. The top row of images are of the clean, reconstructed Si(111)-(7×7), which shows a very low defect density under the three different tunnelling conditions of +1.0V (Fig. 5.9a), +2.0V (Fig. 59b) and -2.0V (Fig. 5.9c). The second row of images (Fig. 5.9d-f) are of the surface after it has been exposed to the XPS for 20 min and tunnelling has been carried out under the same conditions as per the clean sample. Here an increase in defects (dark spots) can be observed at all three tunneling voltages. It is suspected that the dark spots are a consequence of quenching of the surface dangling bonds due to adsorbed species at these sites.

The last row of images are of the surface after Ge CVD is carried out at 300K on the irradiated surface. The image at the tunnelling voltage of +1.0V (Fig. 5.9g), shows areas of dark spots which can be assigned to atoms where the dangling bonds have been quenched due to adsorption at these sites. At +2.0V the dark spots are no longer visible but white diffuse spots appear on top of the Si atoms in Fig. 5.9h are thought to be germane fragments[95]. At -2.0V (Fig. 5.9i), the diffuse white spot can no longer be imaged. Instead a pattern consisting of bright and less bright spots is seen. The interpretation of this image is complicated by the fact that at this tunnelling voltage, half of the Si(111)-(7×7) is darker than the other half due to the presence of a stacking fault on the half of the unit cell which appears darker at this tunnelling voltage. However as the normal pattern of the unit cell is no longer apparent (Fig. 5.9i) in this image, it is likely that the change in the pattern seen may be due to the presence of adsorbed species.

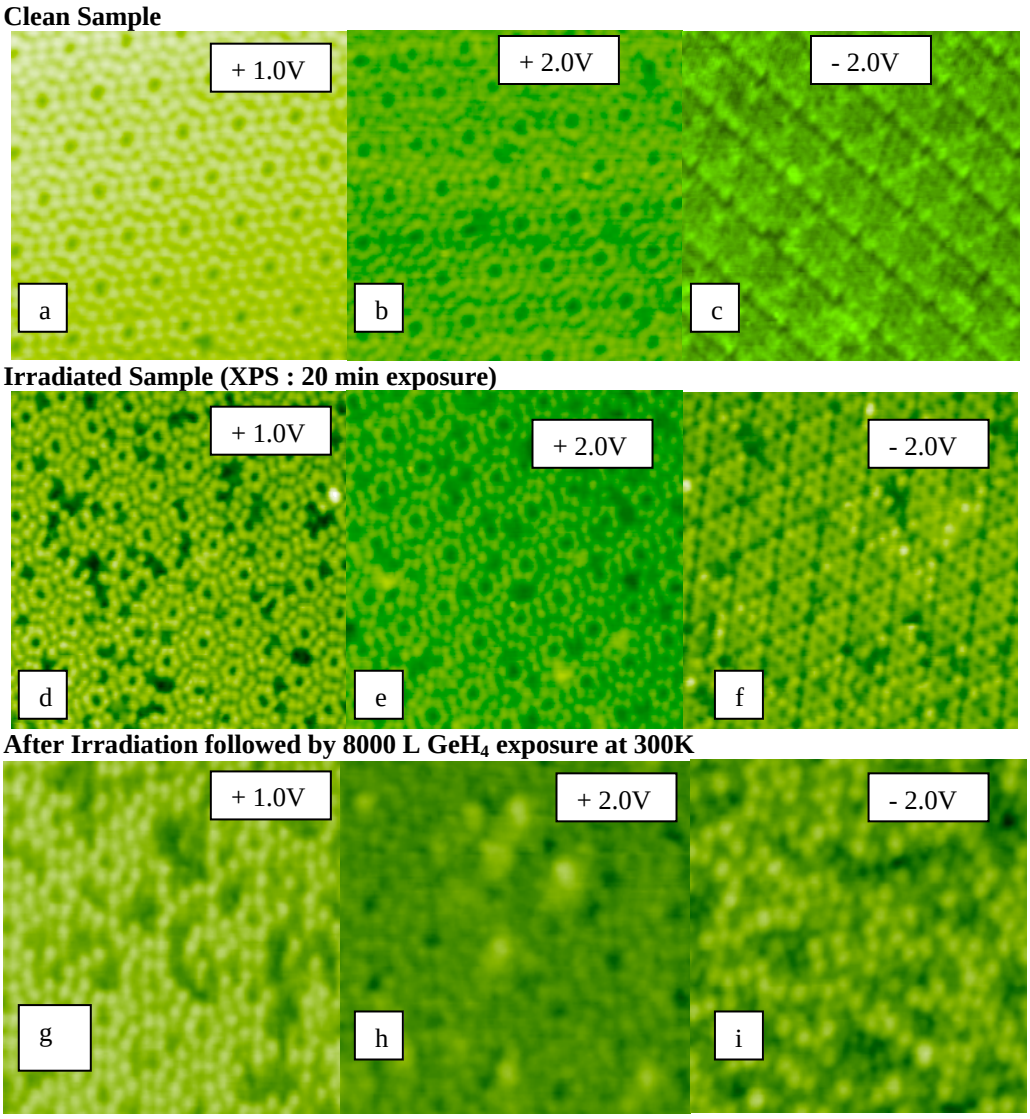

Fig. 5.9 : 58 nm×58 nm STM Images (a)-(c) Clean sample, (d)-(f) Irradiated Si, (g)-(i) surface after irradiation followed by 8000 L GeH_4 exposure at 300K

5.6.4 Discussion

Although it is not possible to tunnel at the same spot after each test, it can be said with confidence that differences are observed on the surface after the surface has been exposed to the XPS. Where the original reconstructed surface has a low defect density, the surface after exposure is imaged to be with a large defect density at all three tunnelling conditions. As the images are of the same spot but at different tunnelling voltages, the contrast indicates that the atoms are not etched off but are quenched (dark spots) under certain tunnelling conditions. This is a clear indicator of an adsorbate at the dangling bonds. This effect is similar to that seen when hydrogen is adsorbed at the dangling bonds.

5.7 Hydrogen Exposure Prior to GeH_4 CVD

5.7.1 Introduction

In Section 5.5, it is established that the main outgassing components are hydrogen, CO_2 and CO. In this section, an experiment is carried out to simulate the outgassing prior to deposition, followed by deposition and to image the structures thus formed via the AFM. Of the 3 major components of the outgas, hydrogen is the major product. From SHG measurements molecular hydrogen is known to have a maximum dissociative sticking probability of less than 10^{-6} on the Si(111)-(7×7) surface[96,97] at 300 K (room temperature). In comparison, from XPS data[92], the other major components of the outgas are not appreciably present on the silicon surface even after the surface has been exposed to the XPS for 4 hours. In order to simulate the effect of outgassing on the CVD grown Ge islands only the major component of the outgas, hydrogen is used. Hence to test the effect of an adsorbate on the silicon surface, the clean substrate is exposed to a hydrogen pressure which is equivalent to the increase of pressure in the system, when the XPS is turned on prior to deposition.

5.7.2 Experimental Procedure

In order to mimic the effects of outgassing from the XPS the substrate is exposed to molecular hydrogen at a pressure of 3.5×10^{-9} mbar for 30 min, after which Ge CVD is carried out for 30 min using the default conditions stated earlier. The hydrogen pressure has been determined in the following way. The QMS is first turned on and the baseline MS of the UHV chamber is recorded at low attenuation. The XPS is then turned on and the MS of the chamber is recorded after the XPS had been in operation for 30 min (Fig. 5.10a). After the XPS has been turned off, the UHV system is allowed to return to baseline conditions after which hydrogen is dosed via the leak valve and the MS of the dosed hydrogen is recorded at different hydrogen fluxes in order to determine a hydrogen pressure which is equivalent to the outgassing from the XPS (Fig. 5.10b) as a function of equivalent counts in the MS. This is taken to be the optimal hydrogen dosing pressure.

5.7.3 Results

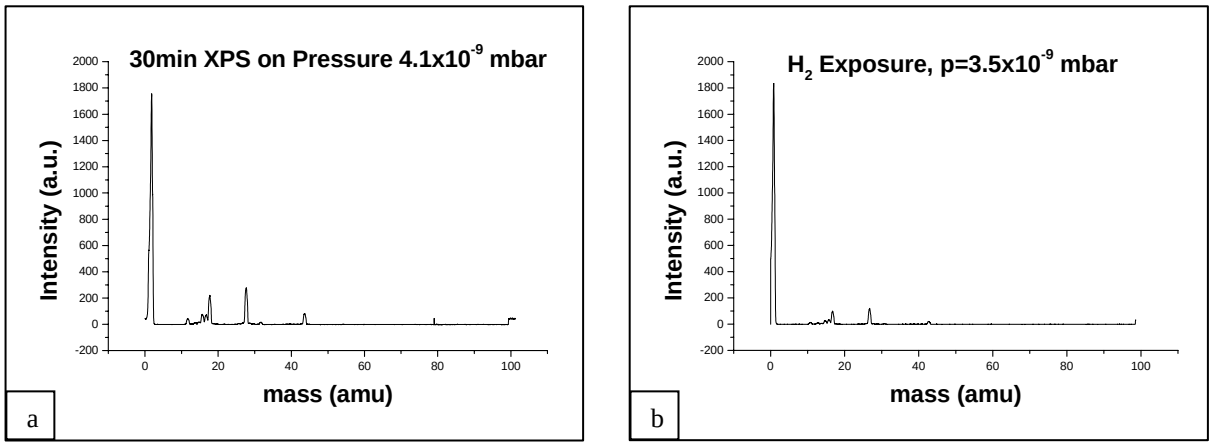

Fig. 5.10 : Determination of H_2 Pressure (a) XPS, 30 min (b) H_2 Dosing

The optimal hydrogen dosing pressure, is determined to be 3.5×10^{-9} mbar (Fig 5.10b).

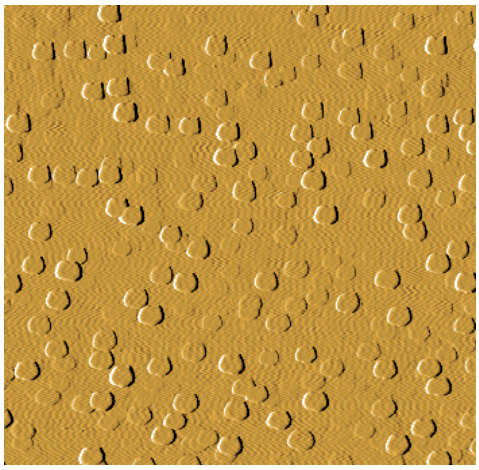

Fig. 5.11 : 20 μm×20 μm AFM image after exposure to atomic hydrogen, followed by 30 min Ge CVD at 750 K, 7×10^{-5} mbar

The AFM image (Fig. 5.11) indicates that the Ge 3D islands are small and rounded like those which have been characterised in Chapter 4 (irradiated sample) and those seen in Fig. 5.6. The island density is about 8.4 islands per μm^2 and the diameter of the average island is about 0.8 μm.

5.7.4 Discussion

The results indicate that the growth morphology of the Ge 3D island growth has changed markedly when the clean reconstructed Si(111)-7×7 has been pre-exposed to hydrogen prior to GeH_4 deposition by CVD. Although the appearance of the 3D islands is not an exact match (island diameter and density) to those seen after the XPS outgas experiment the magnitude of the island density and size, and the shape of these islands is close enough to ascertain that hydrogen has an influence in altering the growth morphology of the 3D islands. The differences can be accounted for by the fact that the actual outgas from the XPS is a mixture of which hydrogen, CO_2, CO and oxygen are the predominant components. As in this experiment, only the main effect of an outgassed component is tested, it is to be expected that the results are not an exact match as the complexities of the influence of the rest of the components of the outgas from the XPS, are not taken into consideration in this experiment.

5.8 Summary

The results for the shielding (Section 5.2.1) experiment show the presence of Ge 3D structures on both halves of the sample. If irradiation is the direct cause of the propagation of the 3D structures, then it is expected that the 3D structures will resemble those in Fig. 4.7a in the shielded (non-exposed) half and Fig. 4.9a in the unshielded (exposed half). Instead the size and shape of the islands on both halves of the sample are identical and the only difference is in the island densities. This leads to the rejection of the hypothesis that irradiation is the direct cause of the propagation of the 3D structures.

However from Fig. 5.9, it is clear that there is some change to the surface after irradiation. The STM images (Fig. 5.9 d-f) of the surface after irradiation show an increased defect density in comparison to the images of the clean sample (Fig. 5.9 a-c). When comparing the surface under the different tunnelling conditions, it can be seen that the atoms are not missing but are in fact quenched. This indicates the presence of an adsorbate on the silicon surface.

The results from Section 5.2.2 and 5.2.3 indicate that the most likely source of these adsorbates is the XPS source itself.

Experiments c to test the effect of the main component (hydrogen) on the growth morphology of the Ge 3D structures, clearly indicate that the growth deviates from the normal growth by CVD which is described in Chapter 4. Furthermore the type of islands formed as well as the island density bear close resemblance to what is seen when the surface is exposed to the XPS prior to deposition. By considering all of the test results, it is clear that irradiation by soft X-Rays did not create the C_s/C_i defects. However the exposure to XPS has an effect, in that the outgassing from the XPS source leads to adsorbates on the surface, which takes up a small amount of active reaction sites at the dangling bonds.

Although the sticking probability of molecular hydrogen at 300 K[96,97] is determined to be less than 10^{-6}, studies have shown that hydrogen[96,97] adsorbs dissociatively on the Si(111)-(7×7) surface at higher temperatures with the sticking coefficient[96,97] increasing to 10^{-7} at 750 K. Hence, under the CVD conditions where the substrate temperature is at 750 K, it is expected that the additional hydrogen from the dissociation of germane competes with the oncoming germane molecules for the vacant dangling bond sites on the silicon surface.

At 750 K the desorption of hydrogen from the Ge(111) surface[98] is higher than from the Si(111) surface[99]. Hence it is more probable to find relatively more vacant dangling bond sites on the Ge islands rather than on the silicon surface. Hence it is more probable that further growth takes place more quickly on the Ge islands rather than on the silicon surface, causing small islands to grow higher rather than wider as is observed on a clean Si(111)-(7×7) surface.

Chapter 6

STM/XPS studies of ultrathin Si_xGe_{1-x} films grown on Si(111)-(7×7) by CVD

6.1 Introduction

SiGe layers have recently gained importance due to new applications such as HFET (**h**eterostructure **f**ield **e**ffect **t**ransistor), etc. It is well known that thin film growth is influenced by various factors such as deposition temperature, gas composition[100] and the off-orientation of the crystal. These factors influence, to varying degrees the morphology of the film growth and the sticking coefficients of the species deposited.

As the precursor gases used in CVD are often hydrated gases, the deposition temperature has an effect on the reactive sticking coefficients due to the effect of the co-adsorbed hydrogen. This also influences the morphology of the islands formed, as temperature effects influence the mobility of the Si and Ge containing species.

As the sticking coefficients for germane and disilane are different, the variations in the ratios of these precursor gases in a gas mixture are expected to effect the sticking probabilities of the Si and Ge containing species in different gas mixtures.

The off-orientation of a crystal influences its terrace width. Wafers with low off-orientations have a large terrace width after reconstruction. This enables the study of CVD behaviour at higher temperatures and low pressures as the data on the mobility of the Si and Ge species as well as information on the growth morphology can be obtained for these conditions.

In a previous work by J. Braun[12,13] the effect of temperature on the coverage at a constant exposure have been studied for two different gas mixtures. The temperature range of 400 K to 760 K has been chosen in this study as the epitaxial growth is known to change from a self limiting to a continous growth in this temperature range[12,13]. The results indicate a low and high temperature regime[12,13] similar to that described for the Si(100) system by Kim et.al[37]. In the follow up Diplom work of M. Holz[14], the coverages over a range of exposures (at a constant deposition pressure), at the two temperatures stated above, have been evaluated.

In this chapter the results of the STM/XPS study on the ultrathin SiGe layers grown by CVD on Si(111) substrates with two different off-orientations, at two different temperatures, 750 K and 850 K with low constant deposition pressure will be presented.

6.2 Experimental Procedure

For this study a gas mixture containing the precursor gases GeH_4 and Si_2H_6 mixed in a 7:3 ratio respectively is used. In order to study the mobility of the Si and Ge species and the progression of island growth, a low deposition pressure of 2.5×10^{-6} mbar is used. To observe the effect of differing terrace widths, wafers with off-orientations of 0.03^o and 0.5^o are used.

The deposition temperatures have been selected after careful consideration of the TPD profiles (Fig. 6.1) of hydrogen from the surfaces of Ge(111) and Si(111).

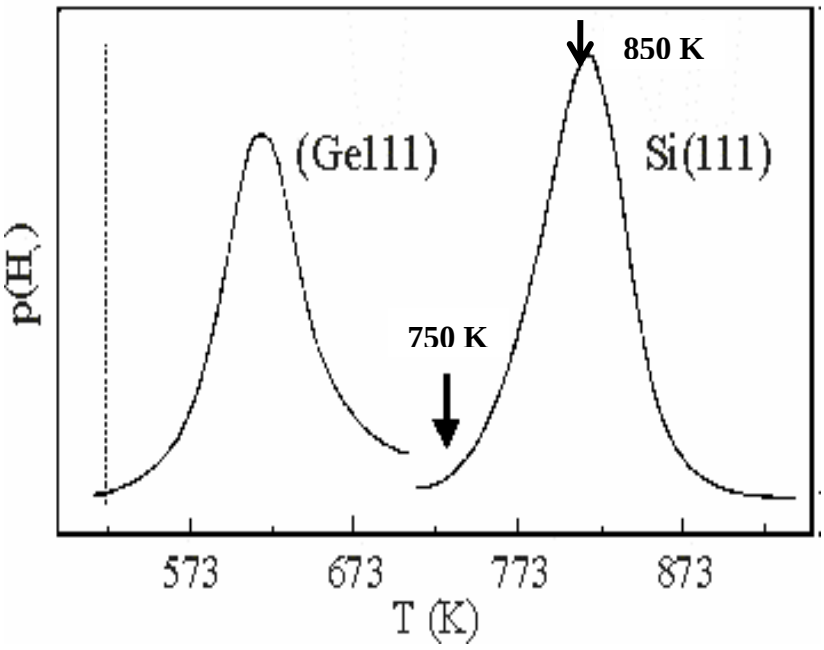

Fig. 6.1 : TPD profile of hydrogen from the Ge(111) and Si(111) surfaces[12]

750 K and 850 K, are the temperatures at which the desorption of hydrogen from the Si(111) begins and is the maximum respectively. These two temperatures have been selected as they are deemed to reflect the effect of co-adsorbed hydrogen on the Si(111) surface.

6.3 Results and Discussion

6.3.1 Calculation of coverage

As germanium is indistinguishable from silicon in STM images, the STM and the XPS are utilised for the calculation of coverages. From the XPS, the calculation of Ge coverage is obtained using the method described in Chap. 4. However, this method cannot be utilised for the Si coverage as XPS does not distinguish between the deposited Si and the bulk Si signal from the substrate. Instead the Si coverage is calculated indirectly from the processed STM images using the IDL software.

Although individual coverages cannot be ascertained from the STM images, total coverages can easily be calculated via IDL. After the images have been leveled via IDL, a slice of the whole image is chosen (Fig. 6.2a) to ascertain the height of the islands in terms of bilayers (BL). This is done by drawing a line from the substrate right across the other islands to the top

of the highest island visible, with the darkest area being the substrate and the brightest being the highest. The profile of the island thickness is then calculated by IDL where each equivalent gain in step height as shown in Fig. 6.2b represents an increment in island height by one BL. Where a step height is twice or three times another step, then the individual step represents a 2 or 3 BL increase respectively. For example, in Fig. 6.2, the dark green area in Fig. 6.2a is the substrate. The green line in the same figure can be seen to cut across three islands whose heights increase with increasing brightness of the image. In Fig. 6.2b, the height profile which represents the heights across the green line in Fig. 6.2a is shown. Three steps of equivalent height can be seen in this figure. The baseline to the right of the figure represents the substrate and each equidistant step an increment of island height by one BL. Hence, the three islands in the slice of STM image in Fig. 6.2a have islands heights of 1, 2 and 3 BL going from the right to the left of the green line in that figure. Using this procedure, the heights of all the islands are mapped out in the whole image.

The next step is to determine the coverage as a function of island height. For this calculation, the whole image (Fig. 6.3a) is selected and the area coverage function in IDL chosen. IDL then produces a graph of percentage coverage as a function of of height (Fig. 6.3b).

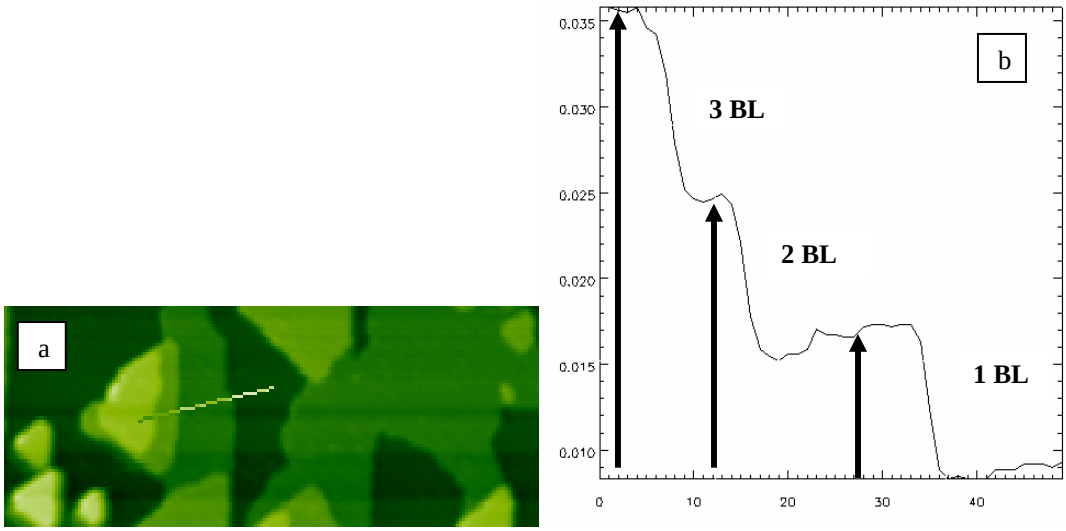

Fig. 6.2 : Calculation of height from the STM Images
(a) Slice of STM Image (2 300 L, 750 K, 0.03°, 1500 nm × 1500 nm), (b) Thickness profile from IDL

In Fig. 6.3b, fives peaks can be seen. The first peak on the left of the figure, represents the area percentage of the substrate, the second, the area percentage of the island with the lowest height, i.e. 1 BL in this figure, and so on. Hence, the total coverage of the Si_xGe_{1-x} alloy at any given exposure can be calculated from the corresponding STM image. For the image in Fig. 6.3, the coverage of the Si_xGe_{1-x} alloy grown at a temperature of 750 K and an exposure of 2300 L is shown below.

Total Coverage = [(1 × 39.6%) + (2 × 14.6%) + (3 × 7.1%) + (4 × 0.9%)] BL
= 0.95 BL

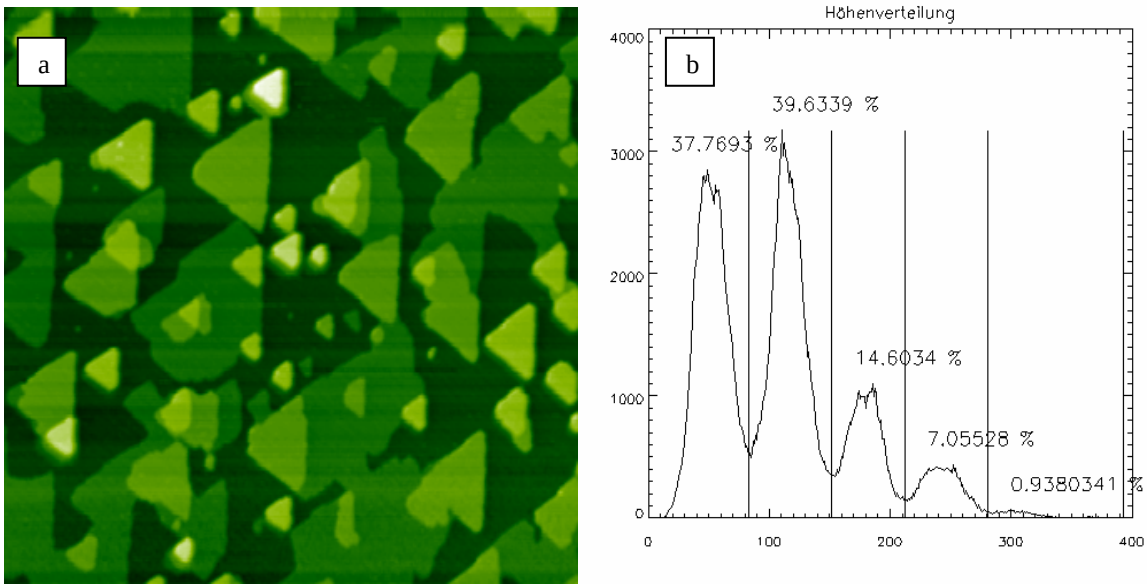

Fig. 6.3 : Calculation of Coverage (a) Whole STM Image from 6.2 (2 300 L, 750 K, off orientation of 0.03° 1500 nm × 1500 nm), (b) Plot of %Coverage vs thickness (from IDL)

6.3.2 Sticking Coefficients

When coverages of Si and Ge containg species are plotted against exposures at 750 K and 850 K (Fig. 6.4), and the integrated sticking coefficients calculated, it is observed that at both temperatures, the sticking coefficients for disilane was greater than that for germane by one order of magnitude. However, there is only a very small difference of sticking coefficients for each species at the different temperatures. In previous work carried out by J. Braun[12,13], it has been reported that the sticking coefficient for Si_2H_6 is 8.5×10^{-5} and that for GeH_4 at room temperature is 1.2×10^{-6} which also shows a difference in magnitude of about one order for the two species.

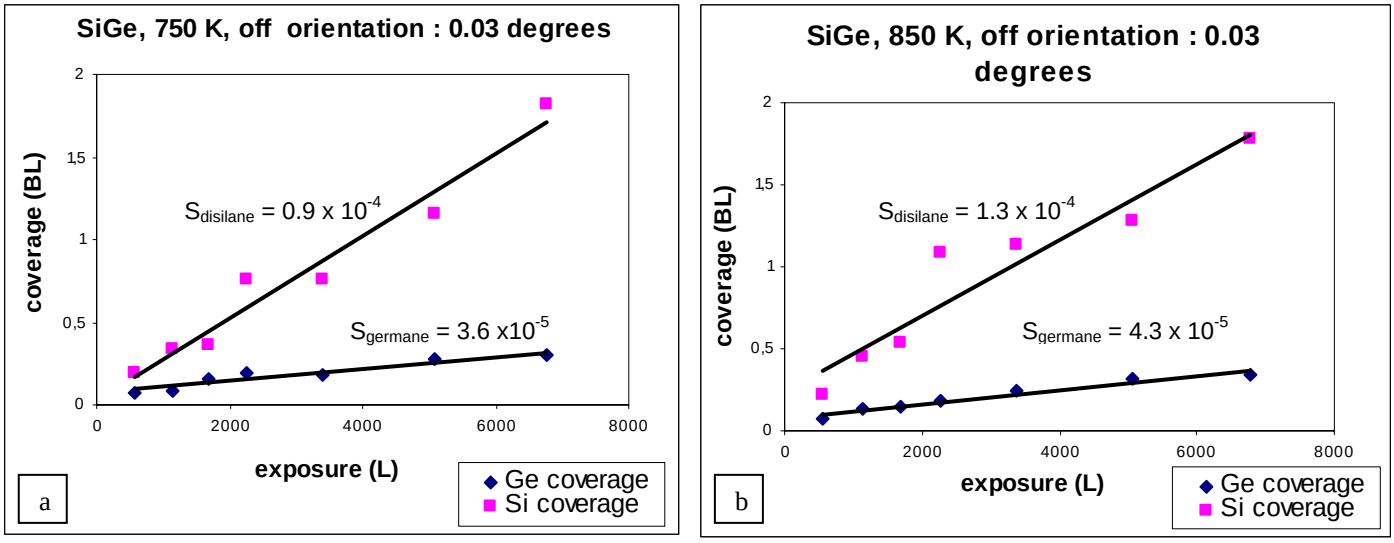

Fig. 6.4 : Plots of coverage vs exposure at (a) 750 K, (b) 850 K

6.3.3 Topography : Effect of Temperature and terrace width

Although, the differences in sticking coefficients at the two different deposition temperatures are minimal, the morphology of the surface after deposition is different at these two temperatures (Fig. 6.5 & 6.6). At 750 K, the SiGe islands tend to nucleate as triangles (Fig. 6.5b & 6.6b). However at the higher temperature there is a greater probability of coalescence of these islands (Fig. 6.5a).

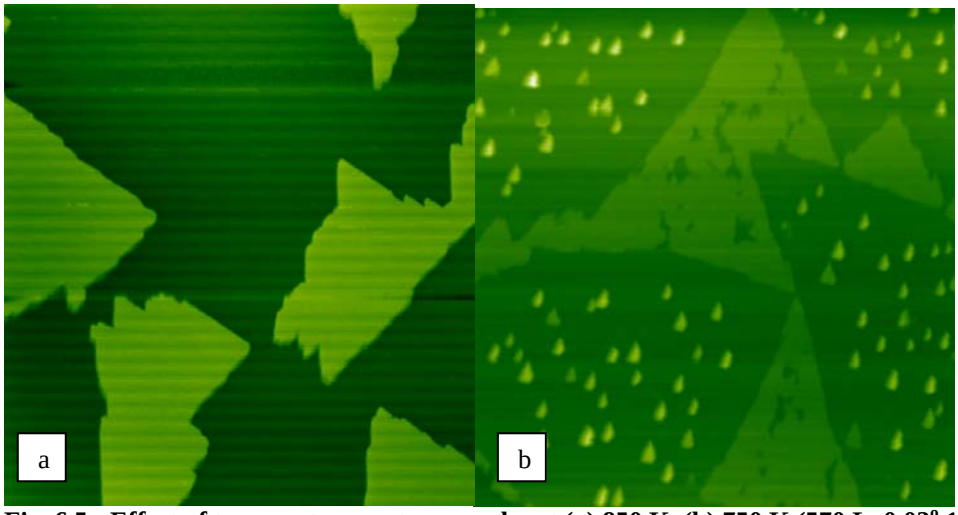

Fig. 6.5 : Effect of temperature on topography at (a) 850 K, (b) 750 K (570 L, 0.03°,1500 nm×1500 nm)

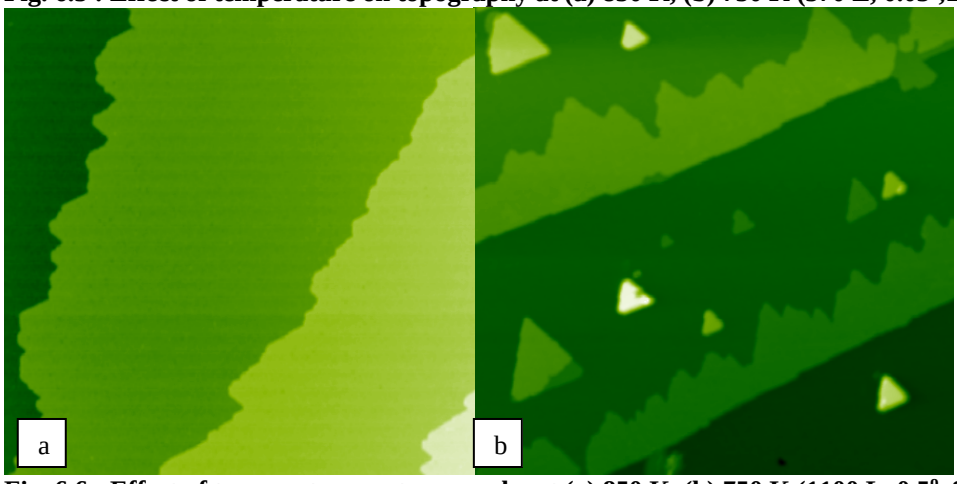

Fig. 6.6 : Effect of temperature on topography at (a) 850 K, (b) 750 K (1100 L, 0.5°, 970 nm×970 nm)

At a larger off orientation of 0.5°, due to the smaller terrace widths the deposited germanium and silicon species nucleate outwards from the step edges at 850 K (Fig 6.6a). However, at 750 K (with wafers having an off orientation of 0.5°), although there is also nucleation at the step edges the nucleation tends to be inwards (Fig. 6.6b). In addition, discrete triangular islands are formed on the terraces. With increasing coverages, the islands growing inwards from the step edges merge with the islands growing at the terraces, forming a 'bridge-like' structure (Fig. 6.7).

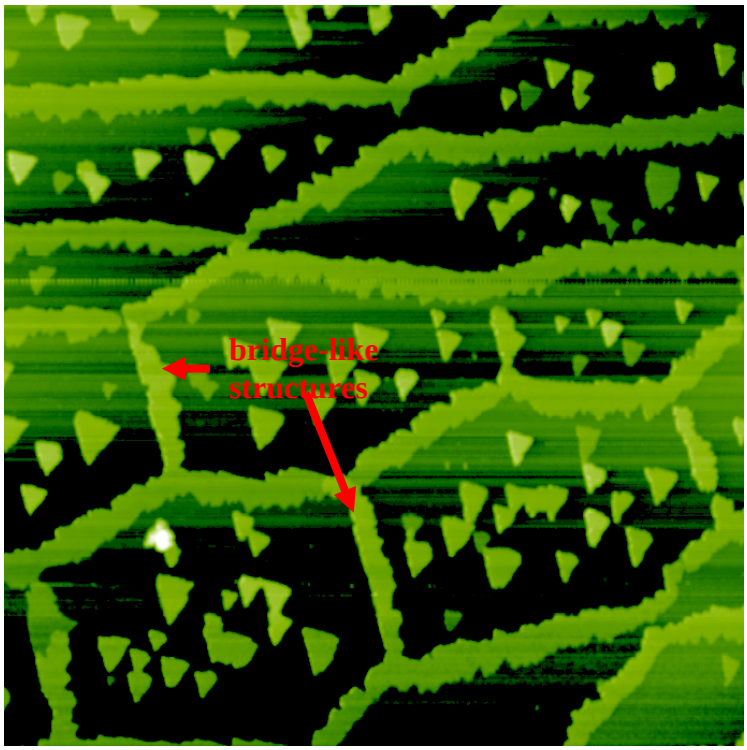

Fig. 6.7 : Topographical image showing 'bridge-like' strucures (750 K 1700 L, 0.5°,1500 nm×1500 nm)

From Fig. 6.8, it is observed that there is an apparent difference in discrete island densities for wafers with different off-orientation, even though the CVD parameters are the same. This difference can be accounted for by the nucleation mechanism for discrete islands on a stepped surface and on a flat surface as illustrated in Fig. 6.9. As shown in Fig. 6.9a, there is a denuded zone bordering each nucleation zone on a stepped surface. Hence the discrete island growth takes place within the nucleation zone in addition to the growth along the step edges. However on a single step surface (Fig. 6.9b), due to the scarcity of terraces the growth consists of predominantly discrete islands, each surrounded with its own nucleation zone. As the number of nucleation zones are less on a stepped surface than on a flat surface, there is a decrease in discrete island densities on a stepped surface.

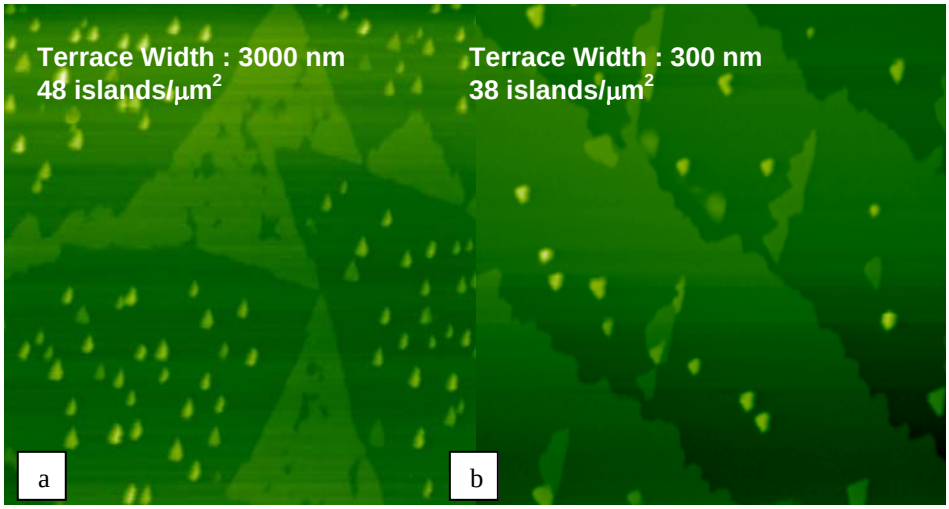

Fig. 6.8 : Effect of terrace width on topography at (a) 0.03°, (b) 0.5° off orientation (570 L, 750 K, 1500 nm × 1500 nm)

However in both cases the coverages remained the same, due to growth along the step edges in the case of a substrate with a larger off orientation.

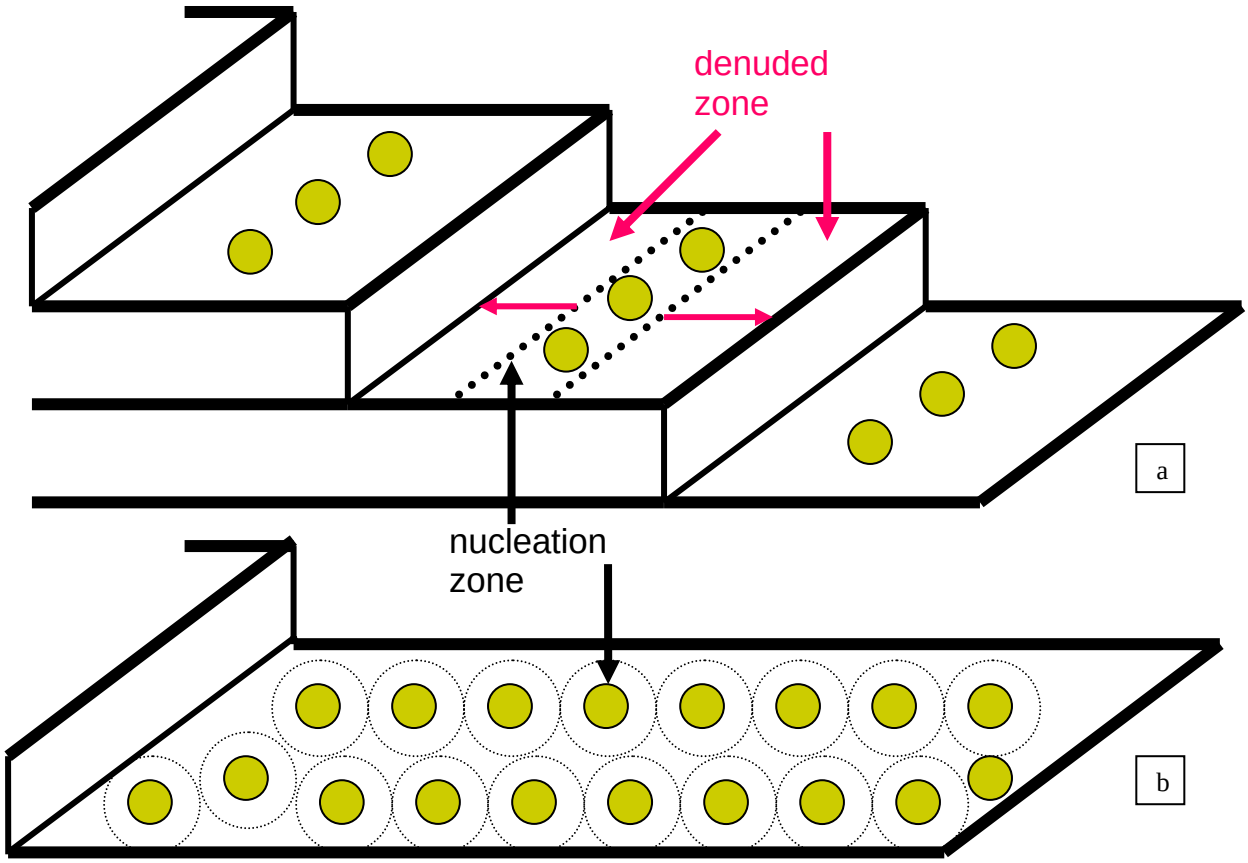

Fig. 6.9 : Nucleation mechanism (a) stepped surface, (b) flat surface

6.3.4 Island Growth at 750 K

At low exposures of 570 L small discrete triangular islands, 1 BL high (Fig. 6.10a) bordered by domain boundaries are formed. At slightly higher coverages of 1100 L (Fig. 6.10b), further growth at the initial triangular islands as well as the nucleation of new islands on top of the older islands are observed. At 3400 L (Fig. 6.10c), there is further increase in island size along with nucleation of new islands on original substrate and on top of older islands. Coalescense of original islands is also observed. At the higher coverages of 5700 L and 10 000 L (Fig. 6.10d,e) the original substrate is mostly covered and the coalescence of larger islands predominates.

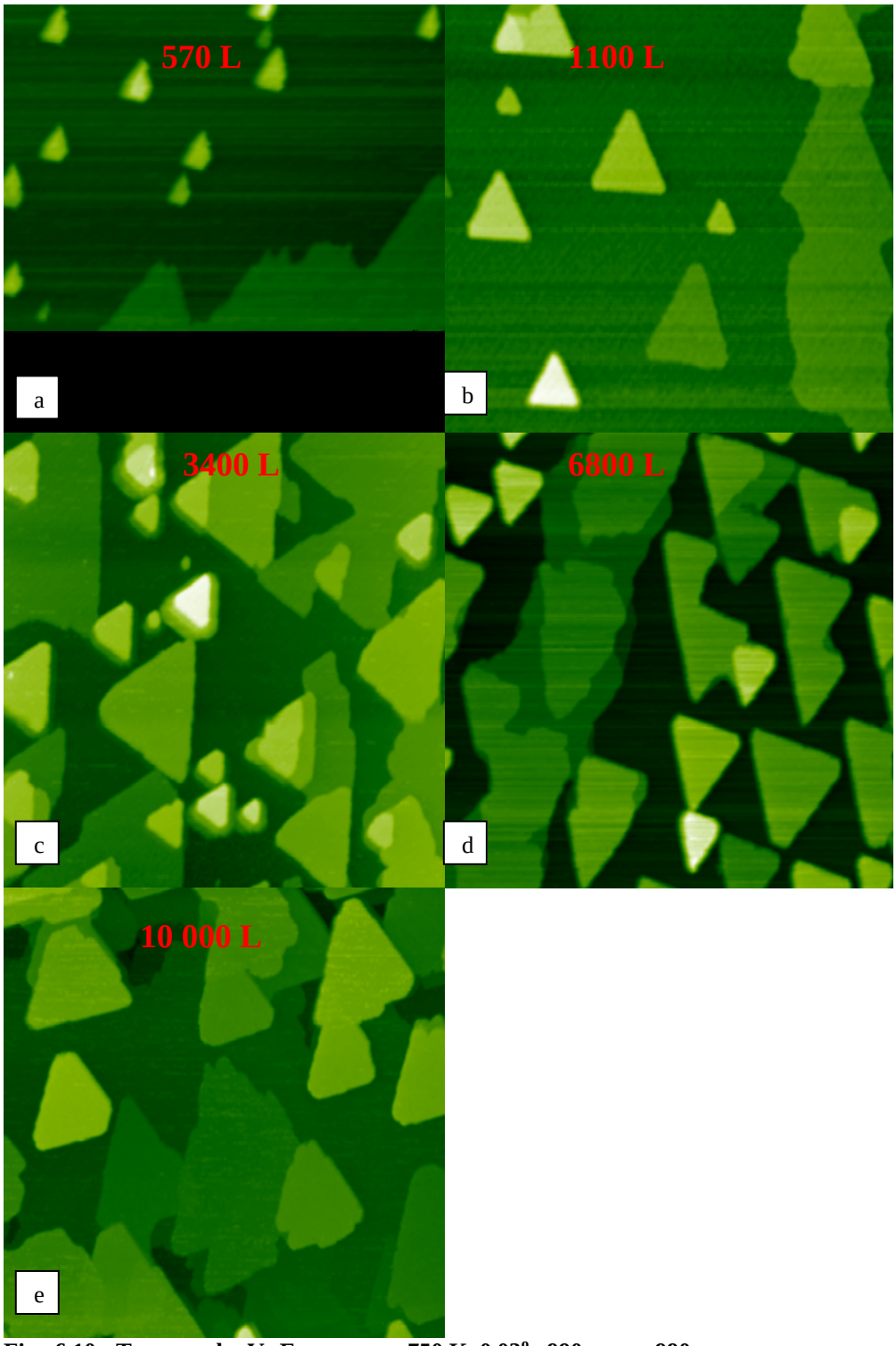

Fig. 6.10 : Topography Vs Exposure at 750 K, 0.03° , 990 nm × 990 nm

The atomically resolved STM images of the SiGe films show that the films are composed of domains of (7×7) and (5×5) DAS structures. The stress from the SiGe lattice mismatch is accommodated at the domain boundaries (Fig. 6.11) where structures such as $(\sqrt{3} \times \sqrt{3})R30^o$ (Fig. 6.11b), (2×1) and semi –(7×7) and (5×5) DAS structures (Fig. 6.11c) are formed.

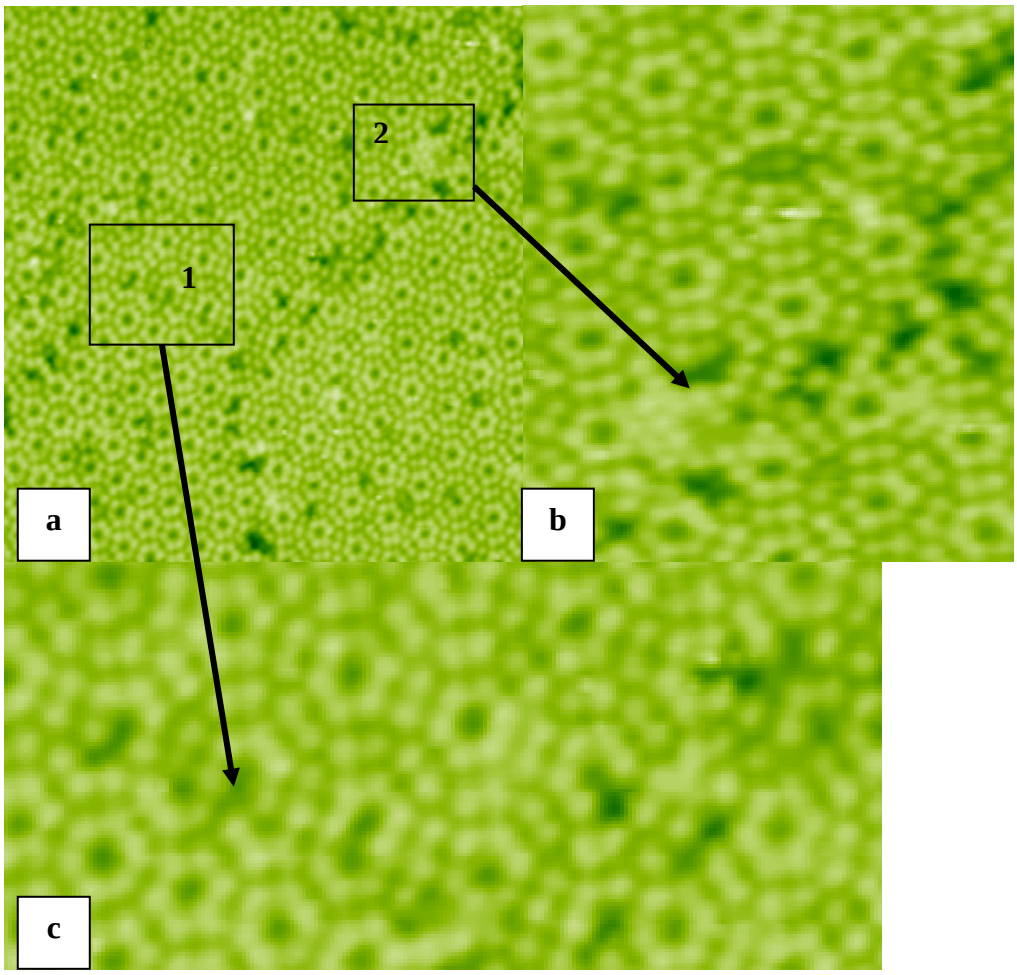

Fig. 6.11 : Effect of strain seen at atomic level (STM image, +1.0V)
(a) 750K, 0.03°, 58nm×58nm, 3400 L, (b) expansion of area 1, (c) expansion of area 2

6.3.5 Island growth at 850K

At 850 K, due to the increase in mobility of the silicon and germanium containg species film formation is favoured over discrete island formation as shown in Fig. 6.12. However, as can be seen in Fig. 6.12, vestiges of triangular islands can be seen at the edges of the films. These suggest that triangular islands may have been initially formed but due to the higher temperature coalescence of islands is achieved.

At the atomic level, in contrast to growth at 750 K, no (5×5) DAS structures are observed on the films grown at 850 K. Bilayer high films grown at exposures of 570 L (Fig. 6.13a) are observed to have only (7×7) DAS structures with missing atoms where the structure cannot be accommodated by the underlaying lattice. At higher exposures (Fig. 6.13b-f), the increasing stress is relieved by the formation of domains of $(\sqrt{3} \times \sqrt{3})R30^o$ and disordered structures (Fig. 6.13b,c,d,f).

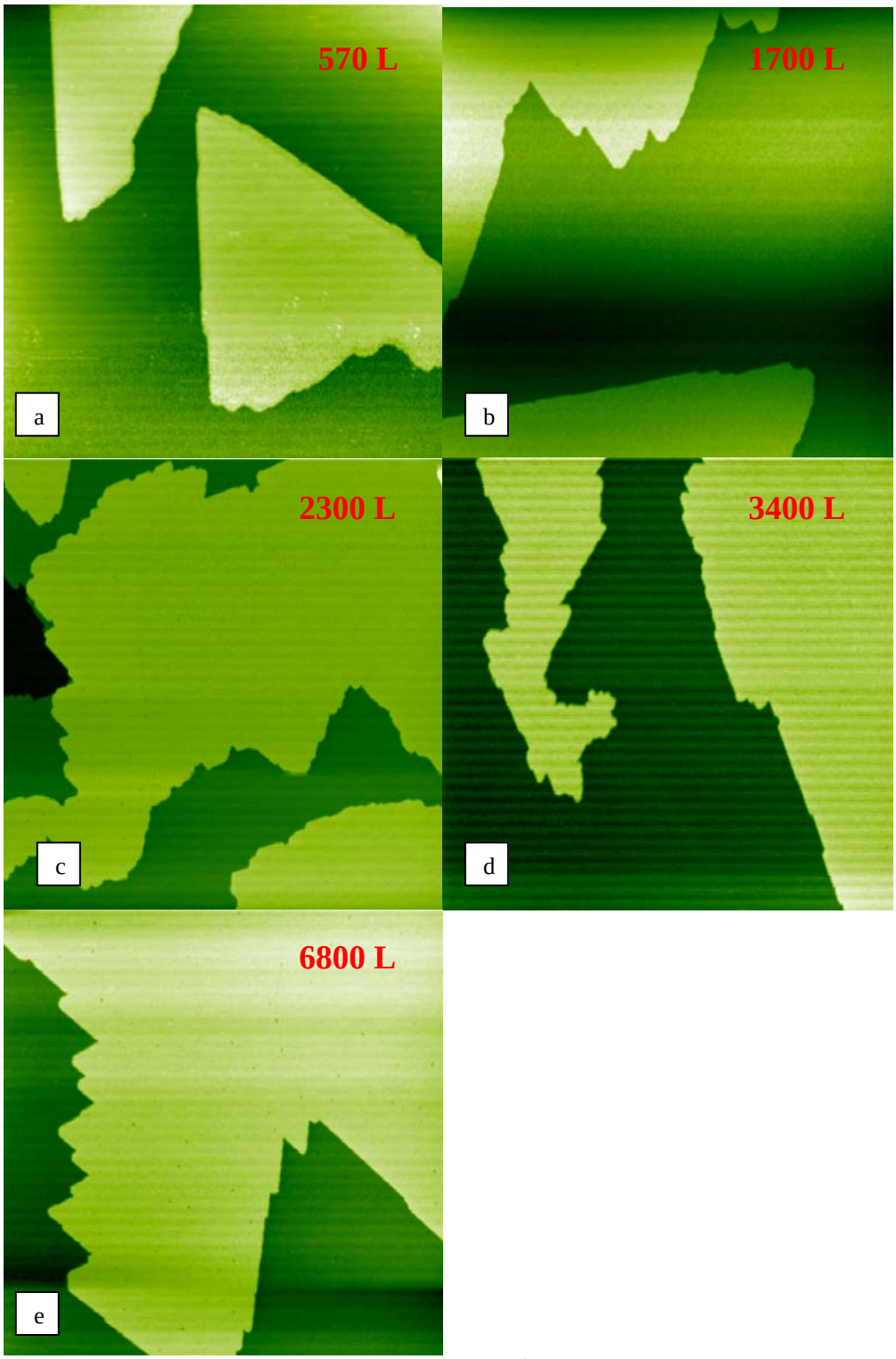

Fig. 6.12 : Topography Vs Exposure at 850 K, 0.03° , 990 nm × 990 nm

In Fig. 6.13e, which is the expansion of area 1 in Fig. 6.13d, the underlayer (darker atoms) can be seen within the black box indicated in the figure. This indicates that the brighter atoms seen on most of this figure are not the atoms from the substrate but are the deposited atoms of the alloy. In the next figure (Fig. 6.13f), which is the expansion of region 2 in Fig. 6.13d, the brighter atoms within the black boxes in this figure are the atoms which are nucleating on top of the alloy layer already deposited on the substrate and can be potential nucleating sites for the next layer.

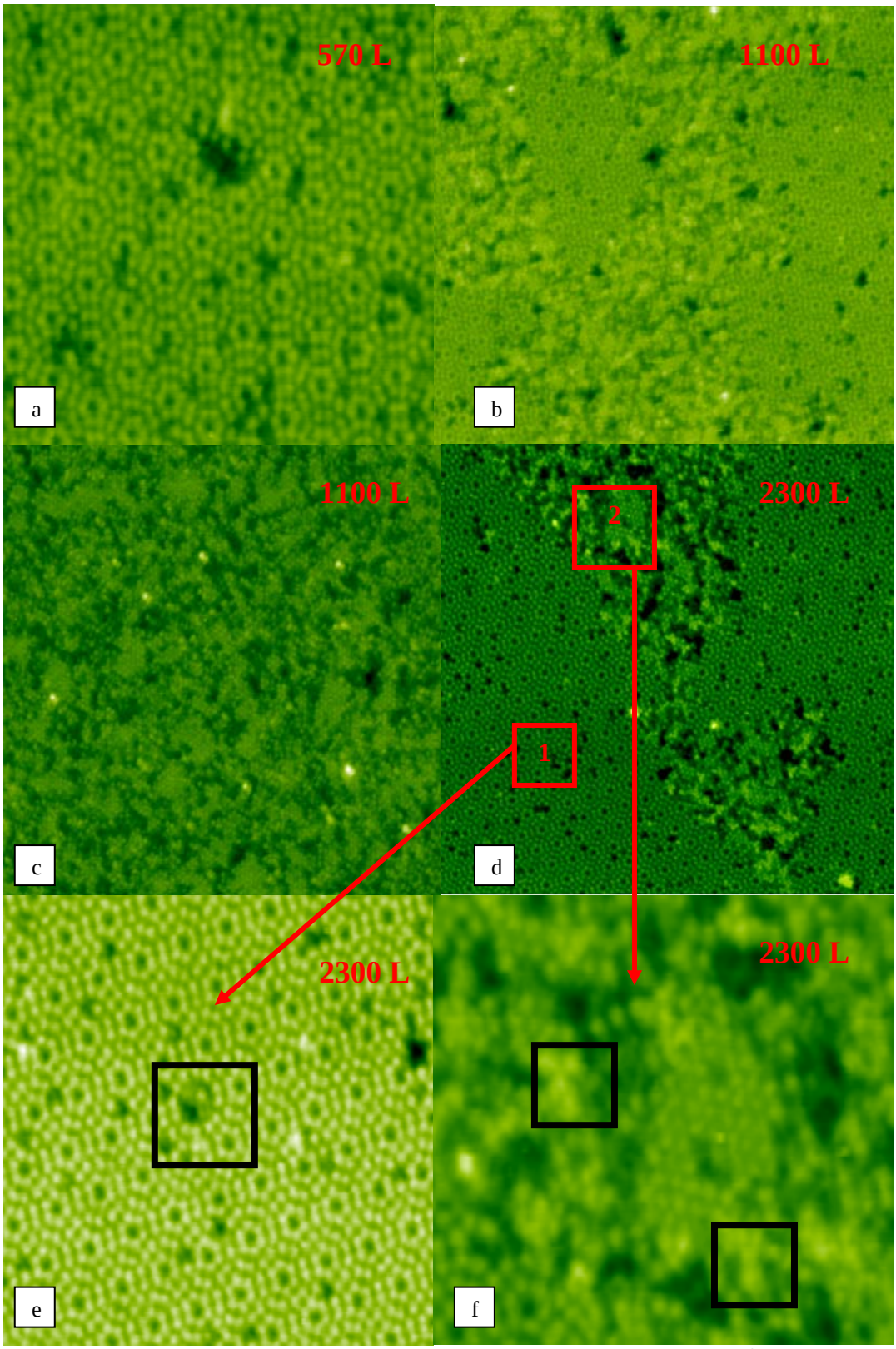

Fig. 6.12 : Effect of strain seen at atomic level (STM image, +1.0V), 850K, 0.03°, 58nm×58nm, (a) expanded image, at 570 L, (b) whole image at 1100 L, (c) whole image at 1100 L, (d) whole image at 2300 L, (e) 2300 L expansion of area 1 from (d), (f) 2300 L, expansion of area 2 from (d).

6.3.6 Deposition Profiles

Experimental deposition rates are calculated as a function of exposure from the experimental coverage values for both temperatures and the resulting plot is as shown in Fig.6.14. Both plots (750 K and 850 K) show two maxima for deposition rates between 570 L and 3000 L, after which the deposition rates appears to plateau. The difference between the two plots is the coverage at which the maximum deposition rate occurs. At 750 K, the maximum growth rate occurs at a coverage of 570 L, while at 850 K, it occurs at a coverage of 2300 L.

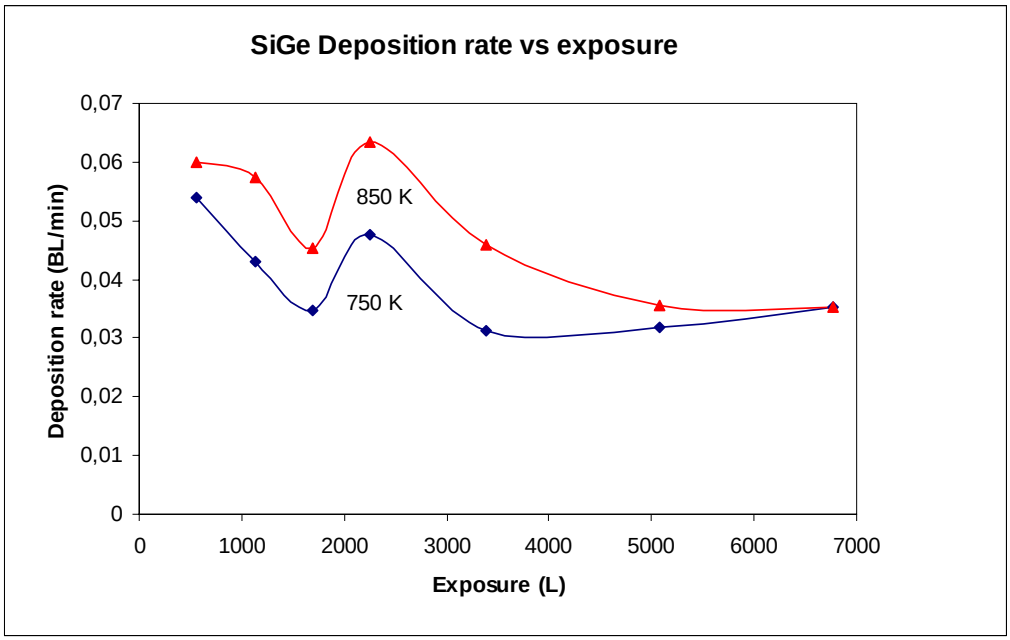

Fig. 6.14 : Experimental Deposition rates as a function of exposure at different temperatures

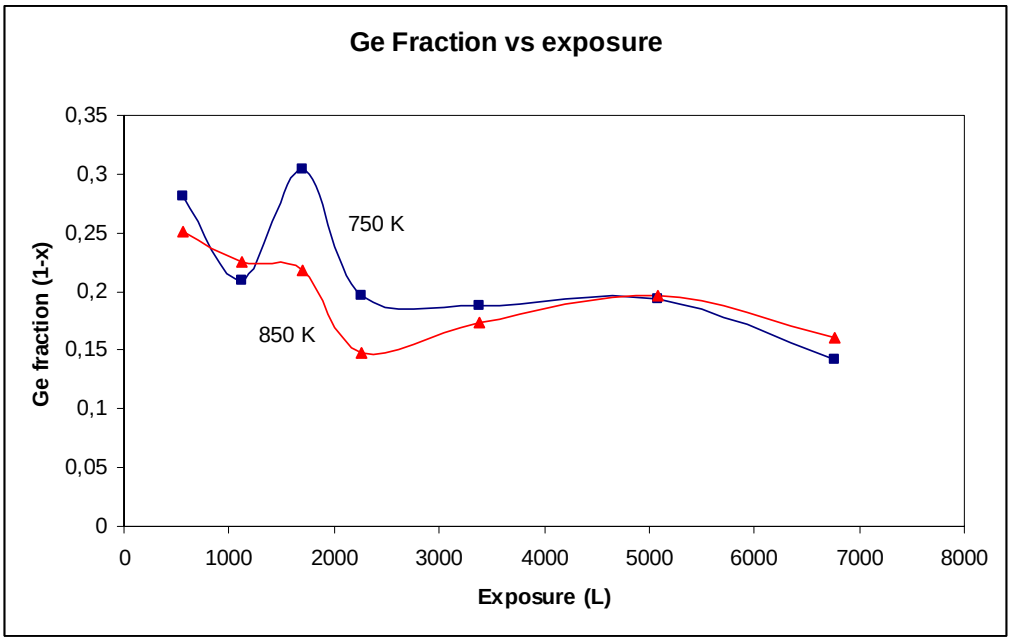

6.15 : Graph of Ge fraction at different exposures for different temperatures

A plot of the germanium fraction in the Si_xGe_{1-x} alloy as a function of coverage (Fig. 6.15) shows two maxima for the germanium fraction at each temperature with the maximum fraction for germanium is at about 2000 L and 570 L at 750 K and 850 K respectively.

As the variation of the germanium fraction in the Si_xGe_{1-x} alloy with respect to coverage is similar to that of the deposition rate, it is possible to relate these two parameters. A plot of the deposition rate as a function of the germanium fraction at 750 K and 850 K is as shown in Fig. 6.16a and 6.16b respectively.

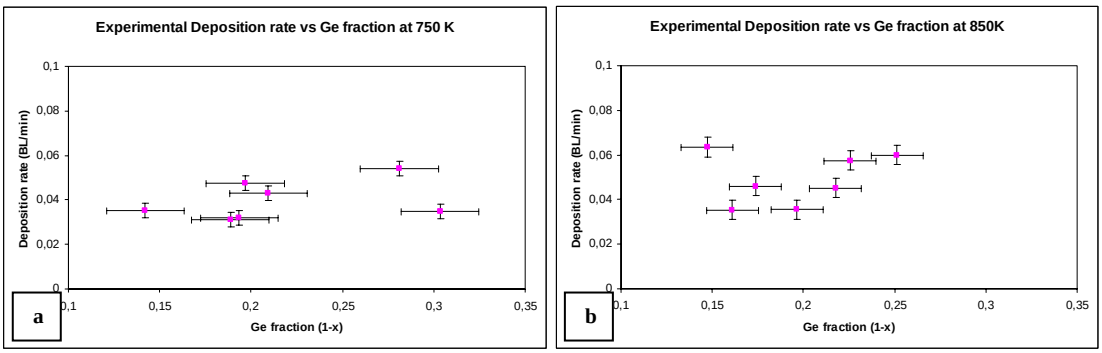

6.16 : Plots of deposition rate as a function Ge fraction at (a) 750 K, (b) 850 K

Jang and Reif[38,39],Robbins et.al.[40] and Malik et.al.[41] have proposed models describing Si_xGe_{1-x} film growth by CVD where the deposition rate is described as a function of the germanium fraction in the alloy. The next section describes two such models which will be used to model the ultrathin Si_xGe_{1-x} film growth that is studied in this work as well as that has been studied by M. Holz in his Diplom thesis[14].

6.3.7 Description of two models of Si_xGe_{1-x} film growth by CVD

The heterogeneous growth model[41] of the Si_xGe_{1-x} film by Malik et. al is given by the following equations describing the disilane and germane adsorption and decomposition, and hydrogen adsorption and desorption.

$$Si_2H_6 + 2VS \underset{k_{-1}}{\overset{k_1}{\leftrightarrow}} 2SiH_3^* \qquad 6.1$$

$$2SiH_3^* \xrightarrow{k_2} 2Si^* + 3H_2(g) \qquad 6.2$$

$$GeH_4 + VS \underset{k_{-3}}{\overset{k_3}{\leftrightarrow}} GeH_4^* \qquad 6.3$$

$$GeH_4^* \xrightarrow{k_4} Ge^* + 2H_2(g) \qquad 6.4$$

$$H_2(g) + 2VS \underset{k_{-5}}{\overset{k_5}{\leftrightarrow}} 2H^* \qquad 6.5$$

where * denotes an activated complex and *VS* a vacant surface site.

As this model assumes that the concentrations of the activated complexes are constant at steady state conditions, the concentrations of the reactive surface intermediates are given by:

$$[SiH_3^*]^2 = \frac{k_1 P_{Si_2H_6} C_{VS}^2}{k_{-1} + k_2} \qquad 6.6$$

$$[GeH_4^*] = \frac{k_3 P_{GeH_4} C_{VS}}{k_{-3} + k_4} \quad 6.7$$

$$[H^*]^2 = \frac{k_5 P_{H_2} C_{VS}^2}{k_{-5}} \quad 6.8$$

and

$$C_{VS} = C_{total} - (C_{SiH_3^*} + C_{GeH_4^*} + C_{H^*}) \quad 6.9$$

where C_{VS} is the concentration of vacant sites on the surface and C_{total} is the total surface site (dangling bond) concentration. C_{VS} can be rearranged in terms of coverage to give:

$$C_{VS} = C_{total}(1 - \theta_{Si} - \theta_{Ge} - \theta_H) \quad 6.10$$

where θ_{Si}, θ_{Ge} and θ_H are the fractional surface coverages of SiH_3*, GeH_4* and H* respectively and are defined as follows:

$$\theta_{Si} = \frac{C_{SiH_3^*}}{C_{total}} \quad 6.11$$

$$\theta_{Ge} = \frac{C_{GeH_3^*}}{C_{total}} \quad 6.12$$

$$\theta_H = \frac{C_{H^*}}{C_{total}} \quad 6.13$$

By substituiting, the terms for coverage, eq. 6.6-6.8 can be rewritten in the following form:

$$[SiH_3^*]^2 = \frac{k_1 P_{Si_2H_6}}{k_{-1} + k_2} \times C_{total}^2 (1 - \theta_{Si} - \theta_{Ge} - \theta_H)^2 \quad 6.14$$

$$[GeH_4^*] = \frac{k_3 P_{GeH}}{k_{-3} + k_4} \times C_{total} (1 - \theta_{Si} - \theta_{Ge} - \theta_H) \quad 6.15$$

$$[H^*]^2 = \frac{k_5 P_{H_2}}{k_{-5}} \times C_{total}^2 (1 - \theta_{Si} - \theta_{Ge} - \theta_H)^2 \quad 6.16$$

The above equations can be expressed in terms of fractional coverage by dividing both sides of eqs. 6.14 and 6.16 by C_{total}^2 and both sides of eq. 6.15 by C_{total}, to obtain the following set of equations:

$$\theta_{Si}^2 = \left[\frac{k_1}{k_{-1} + k_2} \right] \times P_{Si_2H_6} \times \left(1 - \theta_{Si} - \theta_{Ge} - \theta_H \right)^2 \quad 6.17$$

$$\theta_{Ge} = \left[\frac{k_3}{k_{-3}+k_4}\right] \times P_{GeH_4} \times \left(1-\theta_{Si}-\theta_{Ge}-\theta_H\right) \quad 6.18$$

$$\theta_H^2 = \left[\frac{k_5}{k_{-5}}\right] \times P_{H_2} \times \left(1-\theta_{Si}-\theta_{Ge}-\theta_H\right)^2 \quad 6.19$$

By rearranging and solving the above equations, the equations for the silicon and germanium deposition rates are obtained and are as follows:

$$R_{Si} = \frac{k_2 X}{(1+X+Y+Z)} \quad 6.20$$

$$R_{Ge} = \frac{k_4 Y}{(1+X+Y+Z)} \quad 6.21$$

where X,Y and Z are constants which are a combination of the rate constants from the steps 6.1-6.5 and of the partial pressures of disilane and germane and are defined as follows:

$$X = \left(\frac{k_1}{k_{-1}+k_2}\right)^{1/2} \times \left(P_{Si_2H_6}\right)^{1/2} \quad 6.22$$

$$Y = \left(\frac{k_3}{k_{-3}+k_4}\right) \times P_{GeH_4} \quad 6.23$$

$$Z = \left(\frac{k_5}{k_{-5}}\right)^{1/2} \times \left(P_{H_2}\right)^{1/2} \quad 6.24$$

The total deposition rate is a sum of the individual deposition rates of germanium and silicon and is given by:

$$R_{tot} = \frac{k_2 X + k_4 Y}{1+X+Y+Z} \quad 6.25$$

$$k_{-5} = \nu\left\{xe^{\left(\frac{-E_{SiH}}{kT}\right)} + (1-x)e^{\left(\frac{-E_{GeH}}{kT}\right)}\right\} \quad 6.26$$

where ν is the pre-exponential factor, and E_{SiH} and E_{GeH} are the activation energies of hydrogen desorption form the silicon and germanium surface respectively.

The ratio of the germanium to silicon deposition rate is given as follows[38-41]:

$$\frac{R_{Ge}}{R_{Si}}\frac{k_4 Y}{k_2 X} = \frac{x}{1-x} \quad 6.27$$

Substituting 6.26 and 6.27 into 6.25, the following expression for R is obtained:

$$R_{tot} = \frac{mn\sqrt{k_{-5}}}{mx + n\left(q + \sqrt{k_{-5}}\right)(1-x)} \qquad 6.28$$

where m,n and q are constants containing combinations of the partial pressures of disilane, hydrogen and the rate constants, k_1, k_{-1}, k_2, k_4 and k_5. The mathematical expressions for the three constants above are given below:

$$m = k_2 \times \left(\frac{k_1}{k_{-1} + k_2}\right)^{1/2} \times \left(P_{Si_2H_6}\right)^{1/2} \qquad 6.29$$

$$n = k_4 \qquad 6.30$$

$$q = \left(k_5 \times P_{H_2}\right)^{1/2} \qquad 6.31$$

From this model a value for the rate constant for germane decomposition (eq. 6.30) can be obtained when the three constants are solved as a result of a fit of the experimental data.

The plots of the hydrogen desorption rates as a function of the germanium fraction in the alloy at 850 K and 750 K and at 740 K and 620 K are shown in Figs. 6.17a and 6.17b respectively. These plots illustrate the activation of the desorption of hydrogen at the given experimental conditions.

This model assumes a monotonic increase in the hydrogen desorption rate with increasing germanium fraction as is illustrated in Fig. 6.17. The hydrogen desorption from the surface of the alloy has been hypothesised[34] to be catalysed by the incorporation of increasing amount of germanium.

The differences in the desorption rates at different temperatures are due to the differences of desorption rates of hydrogen from the silicon surface. From TPD experiments[34,98,99] (Fig. 6.1) it has been established that at 620 K hydrogen desorbs completely from the surface of germanium but not from the silicon surface and hence there is only a small desorption of hydrogen from the surface of the alloy. At around 740 K, there is an onset of hydrogen desorption on the silicon surface and this is catalysed by the presence of germanium in the alloy lead to a correspondingly large increase from the alloy surface which is about 140 times that at 620 K. At 850 K which is at or close to the maximum desorption rate of hydrogen from the silicon surface, the rate is about 20 times greater than at 750 K and about 3800 times greater than at 620 K.

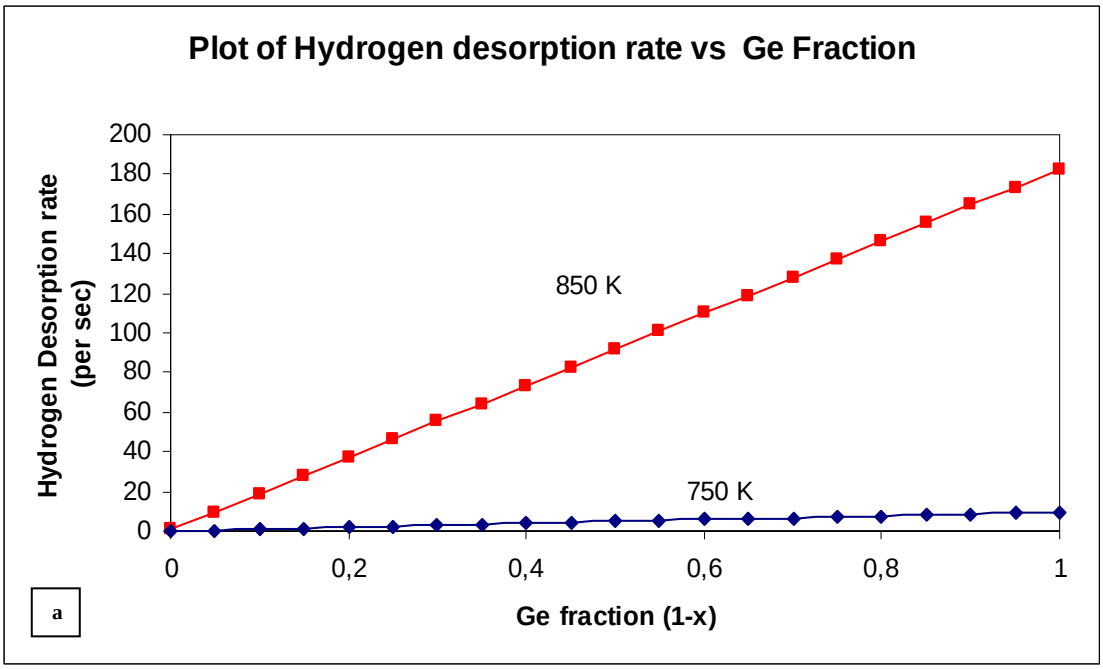

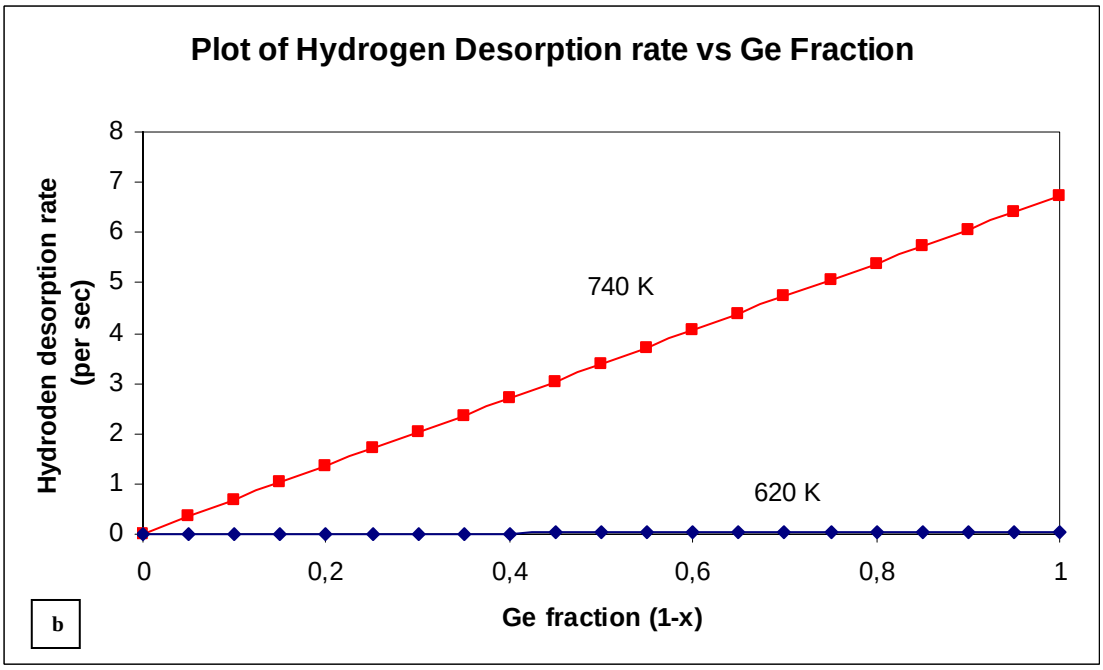

Fig. 6.17: Plot of the predicted hydrogen desorption rate as a function of Ge fraction based on Malik et. al.'s[41], Robbins et.al's[40] and Jang and Reifs[38,39] Model (a) 850 K and 750 K, (b) 740 K and 620 K .

In an alternative model by Robbins et. al[40] and Jang and Reif[38,39], for the silane/germane mixed gas system, the general equations for the growth reactions are given as follows:

$$MH_4(g) \underset{1-r_M}{\overset{k_M}{\leftrightarrow}} (H-MH_3)^* \overset{r_M}{\rightarrow} H(a) + MH_3(a) \qquad 6.32$$

$$H_2(g) \underset{\beta}{\overset{k_a}{\leftrightarrow}} 2H(a) \qquad 6.33$$

where M is either Si or Ge, k_M is defined to be the collision rate per unit surface area and pressure of the gas for the particular species and r_M the probability of dissociative adsorption.

This model introduces a scaling factor to account for the possibility of of the reduction of r_M on the alloy surface with the increasing Ge fraction. This scaling factor is given below:

$$r_M(x) = \frac{r_M(0)}{1+\rho x} \qquad 6.34$$

where the constant ρ is calculated to fit the experimental data. The individual growth rates in terms of M atoms per unit area for each species in this system are given by:

$$R_M(x) = r_M(x) \times k_M P_{MH_4} (1-\theta_H)^2 \qquad 6.35$$

where θ_H is the steady state hydrogen coverage, which can be obtained from the solution to the Langmuir type isotherm for the dissociative adsorption of hydrogen (assuming second order kinetics), which is given below:

$$\frac{\theta_H}{(1-\theta_H)^2} = \frac{2k_a n}{k_\beta} = \frac{1}{2}\nu n\left(\frac{\sigma}{N_S \beta}\right) \qquad 6.36$$

where n is the molecular density, ν the average molecular velocity for hydrogen at 300 K, σ the sticking coefficient of hydrogen and N_S the number of surface sites per unit area. Adapting this model to the disilane/germane system, through substitution, replacement of k_β with its equivalent k_{-5} and rearrangement to a form similar to eq. 6.18, the total growth rate for this model is as given below[41]:

$$R(x) = \frac{m' k_{-5}}{x(n' + \sqrt{k_{-5}})^2 [1+\rho(1-x)]} \qquad 6.37$$

where m' is equivalent to m and n' to q in eq. 6.28.

In both eq. 6.28 and 6.37, the majority of the dependance on temperature is contained in k_{-5}, which can be calculated from eq. 6.26 by estimating the pre-exponential factor to be $8\times10^{11} s^{-1}$, and E_{SiH} and E_{GeH} to be 197 kJ/mol and 157 kJ/mol respectively[41,101].

In essence the equations for the total deposition rate, derived from the two models are similar. In both models, the majority of the rate constants and the constant pressure terms for the partial pressures of germane and disilane are encompassed in the naturally derived constant terms. The bulk of the variation due to the activation of the Si and Ge species, arising at different temperatures is accounted for by the variation in the rate for the dissociation of hydrogen, k_{-5}.

In the model of Malik et. al.[41], three constants (n, m and q) neatly contain all the various constant or nearly constant terms. Robbins et. al.[40] make use of two constants naturally derived (n' and m') and an additional constant (ρ) from the scaling term which is introduced to account for the changes in the growth rate arising from interactions at the surface of the Si_xGe_{1-x} alloy.

6.3.8 Fitting of experimental data to models

The experimental data are fitted in Sigmaplot 2001 using eqn. 6.28 (Malik's model, Model 1) and eq. 6.37 (Robbins's model, Model 2) and the three constants for each model are generated from the resulting curve fits. The resulting curve fits are as shown in Fig, 6.18 and 6.19.

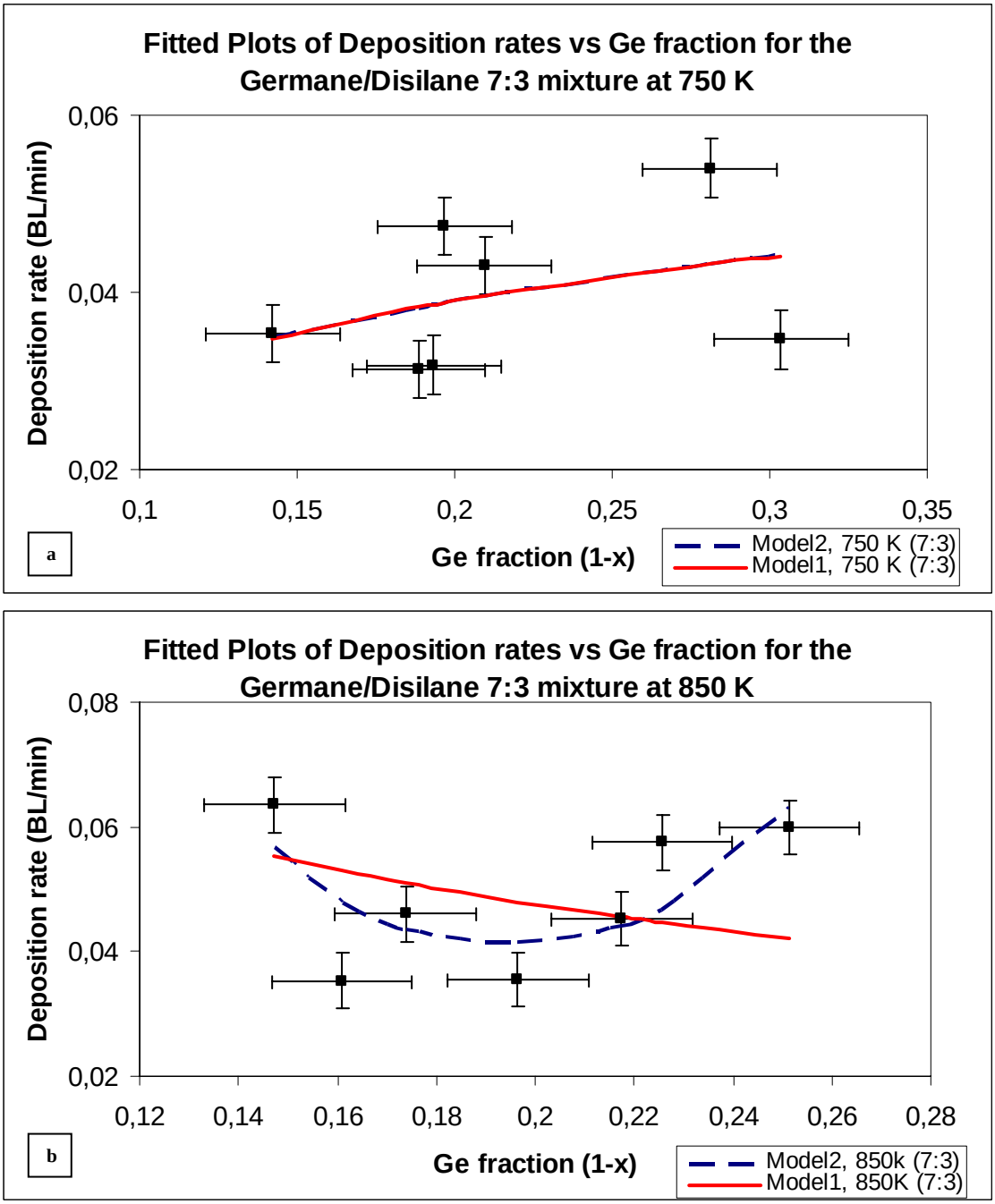

Fig. 6.18: Fitted plots of deposition rate as a function of germanium fraction in the alloy for the 7:3 germane/disilane mixture, p=2.5×10^{-6} mbar, coverage from 570 L to 6800 L at (a) 750 K, (b) 850 K

Fig. 6.18 illustrates the curve fit for the deposition at 750 K and 850 K with the 7:3 germane/disilane gas mixture at a deposition pressure of 2.5×10^{-6} mbar. At 750 K (Fig. 6.18a), both Malik's (Model 1) and Robbins's (Model 2) models give identical fits. Both models fit a slightly bent line or a gentle curve to the experimental data points. The models predict that under the experimental conditions described above, the deposition rate increase with increasing germanium fraction in the alloy for the range of coverages between 570 L to

6800 L. At this range the highest predicted deposition rate occurs at a germanium fraction of 0.3.

However at 850 K a fit is achieved only with Model 2 (Robbins) while a fit is not possible with the model by Malik et.al. (Model 1) as shown in Fig. 6.18b. Malik's model falsely predicts a negative value for the dissociation of the activated germanium complex which implies that dissociation of this complex at 850 K is not probable while Robbins et. al's model predicts a clear minimum for the deposition rate under the conditions stated, at a germanium fraction of about 0.2.

The reason for the identical fits at 750 K and the failure of Malik's model to fit the experimental data at 850 K becomes clear when the assumptions[38-41] on which these models are based on are closely examined. Model 1 (Malik et.al.) assumes steady state conditions and hence the concentrations of the activated complexes are assumed to be constant while Model 2 (Robbins) incorporates a scaling factor to take into account the changes in the growth rate due to the possible reduction of the probability of dissociation at the surface of the alloy as a result of increasing germanium fraction. From Sections 6.3.4 and 6.3.5, it can be seen that at 750 K, the film growth proceeds via island coalescence as well as growth of new layers on top the older layers and hence can be seen as a growth under pseudo steady state conditions while at 850 K, there is no discrete island formation and growth is still layer by layer. Hence at the higher temperature steady state conditions cannot be assumed.

The scaling factor from Model 2 is 4.3 at 750 K and indicates an increasing probability of dissociation with increasing germanium fraction. At 850 K the scaling factor is -3.4 (Table 6.1) which predicts a decreasing probability of dissociation with increasing germanium fraction. However at 850 K, the constant n' has a negative value, which implies that at this temperature the desorption of hydrogen from the surface is highly activated and this partially offsets the reduction in deposition rate from the reduction due to the higher germanium content in the alloy, resulting in a curve with a clear mimum point.

The models are also used to fit M.Holz's experimental data where the deposition has been carried out for two different germane/disilane mixtures of 7:3 and 9:1, with a deposition pressure of 5.0×10^{-6} mbar and deposition temperatures of 620 K and 740 K. The results of the curve fit at 740 K and 620 K are shown in Fig. 6.19a and 6.19b respectively. At 740 K, for both gas mixtures, both models give identical fits, indicating that at these experimental conditions, the pseudo steady state conditions are applicable (Fig. 6.19 a,b).

Deposition Parameters			MODEL 1			MODEL 2		
Gas ratio	Pressure	Temperature	m	n	q	m'	n'	ρ
7:3	2.5×10^{-6}	750 K	-4,0	0,004	-1906,0	0,3	11,6	4,3
7:3	2.5×10^{-6}	850 K	3062,4	-9101,0	15230191,7	0.0012	-31,7	-3,4
7:3	5.0×10^{-6}	740 K	0,4	0,004	-119,7	0,3	18,1	-1,5
7:3	5.0×10^{-6}	620 K	0,5	0,002	-24,1	0,2	7,8	-0,1
9:1	5.0×10^{-6}	740 K	0,01	8721,1	-0,5	0,1	-0,7	64,4
9:1	5.0×10^{-6}	620 K	3,9	0,0003	742,0	2,0	17,9	252,5

Table 6.1 : Tabulation of fitted constants for models 1 and 2.

From Model 1 (Table 6.1) a value for k_4 which is the rate constant for the dissociation of the activated germane complex (eq. 6.4) into germanium and hydrogen, at 740 K can be obtained and is fitted to be 0.004 per min. This rate constant is of the same magnitude at 750 K (Table 6.1) indicating that the decomposition rate of the activated germane complex for a 7:3 germane/disilane gas mixture is constant in the 740-750 K range. The constant q, is negative at both 740 K and 750 K indicating that the probability for hydrogen dissociation in this temperature range is negligible. This model proposes a low value for the constant m at 740 K and a small negative value at 750 K. This indicates (within the errors of the measurements) that the rates of disilane dissociation are low at 740-750 K. This result is in concordance with the TPD profile of hydrogen desorption from the Si(111) surface where the onset of the desorption is around 730-750 K[12,34,99].

Model 2 predicts that for the 7:3 gas mixture, the constants m' (incorporating the rate constants and partial pressure associated with disilane) and n' (the rate constant and the partial pressure associated with hydrogen) are of the same order of magnitude at 740 K and 750 K. This model accounts for the difference in the slopes of the deposition profile with a prediction of variation of alloy composition during deposition.

In contrast to the 7:3 gas mixture, the deposition rate is experimentally determined to decrease with increasing germanium fraction for the 9:1 gas mixture at 740 K. Both models give nearly identical fits this gas mixture at 740 K. As the germanium composition in this mixture is higher than in the 7:3 mixture, the germanium fraction in the alloy has also been determined to be much higher. Hence the constants m (Model 1) and m' (Model 2) which are associated with the rate constants for disilane dissociation and disilane partial pressures are predicted to be small (Table 6.1). The small negative values (Table 6.1) which are obtained for the contants q (Model 1) and n' (Model 2) indicate that at 740 K, the hydrogen desorption from the surface is more probable than the reverse process.

Model 1 predicts that the rate of dissociation of the activated germanium complex, k_4 is 8721 per min for the 9:1 gas mixture at 740 K. Comparing this value for k_4 with that for the 7:3 mixture (Table 6.1) at the same temperature and total pressure, it indicates that with a higher germane ratio in the gas mixture, the rate of dissociation of germane is higher than that of disilane, leading to a larger germanium fraction in the Si_xGe_{1-x} alloy. Model 2 predicts that the scaling factor, ρ for dissociation of the activated germane and disilane complexes to be about 64. Hence the deposition rate decreases with increasing germanium fraction as the probability of dissociation of the activated complex is predicted to decrease with increasing germanium fraction in the alloy.

At 620 K both models show identical curve fits only for the 7:3 germane/disilane mixture (Fig. 6.19b). At this gas mixture, the deposition rate is experimentally determined to increase with increasing germanium fraction. The germanium fraction (Fig. 6.19) in the alloy is higher (0.4-0.7) at 620 K than at 740 K (0.2-0.3) for the same gas mixture (7:3). However the deposition rates are one order of magnitude lower at 620 K than at 740 K. This result is predicted by both models as the hydrogen desorption rate, k_{-5} at 620 K is much lower than at 740 K as shown in Fig. 6.17. The scaling constant (Model 2) is fitted to be slightly negative which indicates that the deposition rate increases with increasing germanium fraction.

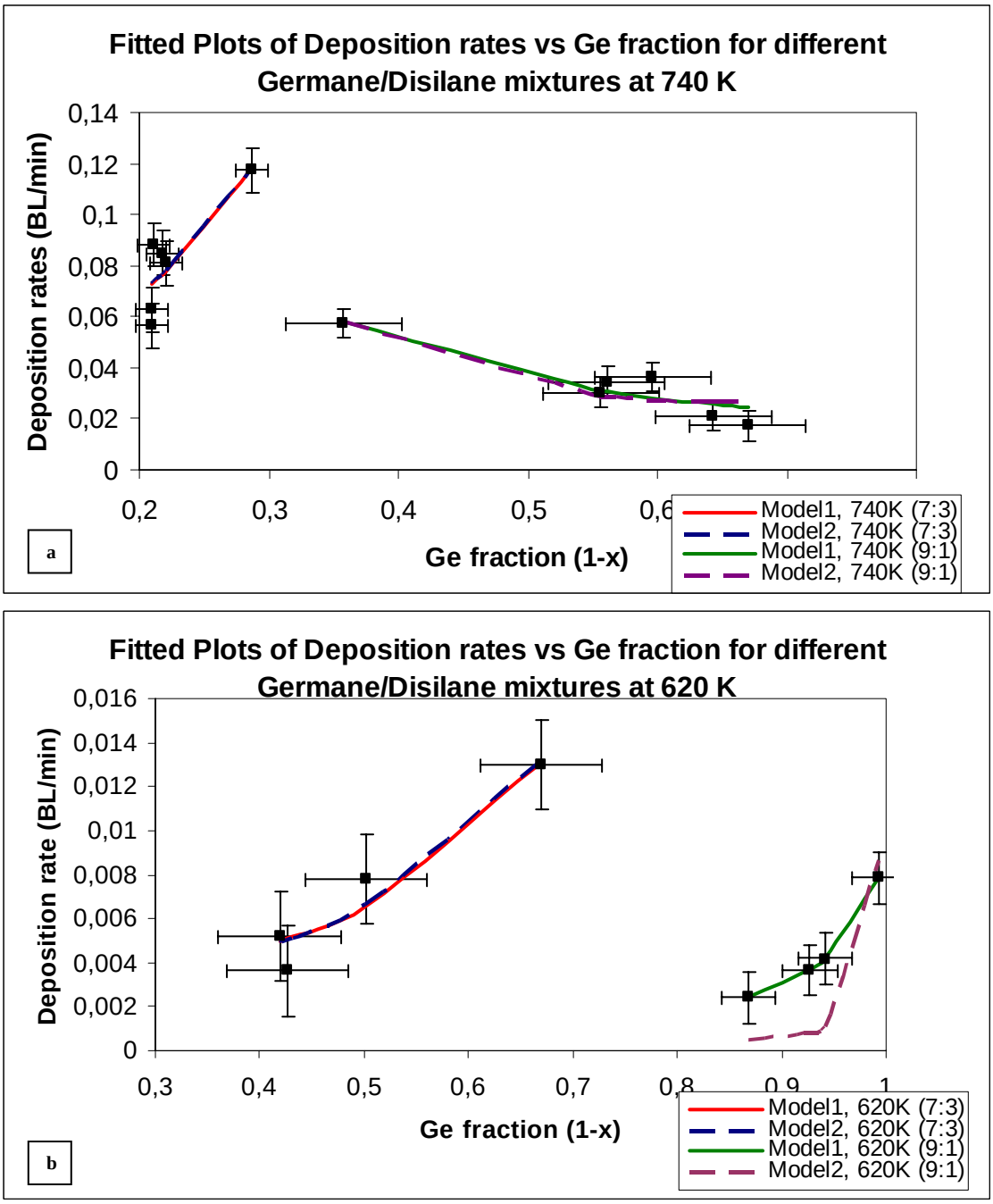

Fig. 6.19: Fitted plots of deposition rate as a function of germanium fraction in the alloy for the 7:3 and 9:1 germane/disilane mixture, p=5.0×10^{-6} mbar, coverage from 1600 L to 9000 L and 1600 L to 27 000 L respectively at (a) 740 K, (b) 620 K (Experimental data from M. Holz's Diplom thesis[14]).

Only one model is able to fit the experimental data for the 9:1 gas mixture at 620 K. The experimental data indicates that the germanium fraction in the alloy under these conditions (Fig. 6.19b) is between 0.85 to 0.99. This indicates that there is very little change in the alloy composition during the deposition. As this implies that the deposition occurs under effectively steady state conditions, model 2 which assumes a change in dissociative probabilities of the activated complexes at the surface of the alloy due to the changes in the alloy composition can no longer be used to fit the experimental data.

6.4 Summary

In summary, the investigation of ultrathin Si_xGe_{1-x} layers indicates that while the sticking coefficients at 750 K and 850 K are of the same order of magnitudes, the reactive sticking coefficients for disilane is observed to be greater than that of germane by one order of magnitude at both temperatures. However a slight increase in the sticking coefficient is observed at the higher temperature. This is in concordance to previous studies carried out by J. Braun et. al[12,13]. Although there is a minimal effect of the temperature on sticking coefficients, there is a marked effect on the morphology of the islands formed. It is observed that the prefered island shape for the SiGe nucleation is a triangle. At the higher temperature, island coalescence is promoted resulting in large islands or growth at the step edges (stepped surface), although vestiges of the triangular islands can still be made out along the edges in both cases.

For the 7:3 germane/disilane gas mixture, a minimum for the deposition rate is predicted at 850 K, while at the 740-750 K range, a monotonic increase in deposition rate with increasing germanium fraction in the alloy is predicted for the given experimental conditions. A similar result is predicted at 620 K, but with lower deposition rates than at the 740-750 K range.

However for the 9:1 germane/disilane gas mixture, a decrease in deposition rate with increasing germanium fraction is predicted at 740 K, while the reverse has been predicted at 620 K. In most cases except for two, both models give identical curve fits indicating that at these conditions, the CVD growth can be likened to a pseudo steady state growth. However, only one model is able to fit (Model 2) for the 7:3 gas mixture at 850 K and the 9:1 gas mixture at 620 K (Model 1). STM images at 850 K indicate a pure layer by layer growth at the stated experimental conditions and since only the initial two or three bilayers grew at these conditions, the composition of the germanium fraction in the alloy is likely to fluctuate with film growth and hence steady state conditions cannot be assumed, leading to the failure of Model 1.

For the 9:1 gas mixture, at 620 K film steady state conditions prevail as the gas mixture consists of predominantly germane and at 620 K (from TPD measurements), the desorption rate of hydrogen from the silicon surface[34,99] is expected to be virtually nil or minimal, leading to a minimal decomposition of the activated disilane complex. These factors ensure that there is minimal variation of the germanium fraction during the growth and hence there is assumed to be little change in the deposition rate due to interactions with the surface of the alloy. As this is an important assumption in the derivation of Robbins Model (Model 2) fails to fit under this set of experimental conditions.

Chapter 7

Summary

This work has shown that under the growth conditions stated in Chapter 4, Ge growth by CVD on a standard Si(111) –(7×7) is not self limiting at 2.5 bilayers but follows the well described S-K growth whereby 3D germanium islands are formed after the layer by layer growth of the initial wetting layer (of about 2 to 2.5 BL).

The mechanism of the formation and ripening of the Ge islands on the standard Si(111) substrate involves the nucleation and coalescence of islands, dislocation formation, intermixing and trench formation. Initially the two dimensional wetting layer grows layer by layer relatively rapidly and is followed by the onset of small 3D islands at about 95 000 L. At higher exposures coalescence of islands takes place when two small islands are in close proximity to form larger strained islands. The strain energy difference between the substrate and the islands causes the diffusion of Si from the substrate into the Ge islands, leading to an erosion of the wetting layer around the islands and at the same time the strained islands undergo selective depletion at their centres to release the strain and form the relaxed atoll structures.

On the irradiated substrate the three dimensional germanium island growth morphology does not follow the same path as that on the standard substrate. Here vertical growth instead of island coalescence predominates, resulting in smaller but higher islands

The STM images of the Si(111) –(7×7) surface after irradiation shows an increased defect density in comparison to the images of the clean sample. STM images under the different tunnelling conditions show that the defects are not due to etched atoms but the atoms are in fact quenched which indicates the presence of an adsorbate on the silicon surface. Other experiments indicate that the most likely source of these adsorbates is likely to be outgassing of the XPS source itself of which hydrogen is the major component.

Experiments to test the effect of hydrogen on the growth morphology of the Ge 3D structures, indicate that the growth deviates from the normal growth by CVD which is described in Chapter 4 and the type of islands which are formed bore close resemblance in terms of island shape, size and density to those on the surface which has been exposed to the XPS prior to deposition.

The investigation of ultrathin Si_xGe_{1-x} layers indicates that there is a slight increase in the sticking coefficients at 850 K in comparison to 750 K. Furthermore the reactive sticking coefficient for disilane is observed to be greater than that of germane by one order of magnitude at both temperatures, in concordance with previous studies.

Even though the variation of sticking coefficients at 750 K and 850 K is small, the morphology of the islands formed at the two different temperatures is observed to be markedly different At the lower temperature the formation of discrete triangular islands predominates while at the higher temperature, island coalescence predominates resulting in the growth of large films. However the vestiges of the triangular islands can still be made out along the edges indicating that the prefered initial shape of island formation is triangular.

The results of the fitting of the experimental data from this work and from M. Holz's Diplom thesis to Malik's (Model 1) and Robbins (Model 2) indicate that for the 7:3 germane/disilane gas mixture, a minimum for the deposition rate is predicted at 850 K, while at the 740-750 K range, a monotonic increase in deposition rate with increasing germanium fraction in the alloy is predicted for the given experimental conditions. A similar result is predicted at 620 K, but with deposition rates, lower than at the 740-750 K range. However for the 9:1 germane/disilane gas mixture, a decrease in deposition rate with increasing geramium fraction is predicted at 740 K, while the reverse is predicted at 620 K.

References

[1] W. Shockley, The path to the conception of the transistor. IEEE *Trans. Electron Devices ED-23(1976) 597.*

[2] J. S. Kilby, Invention of the integrated circuit. IEEE *Trans. Electron Devices ED-23 (1976) 648.*

[3] F. Shimura, "Semiconductor Silicon Crystal Technology", Academic Press Inc., San Diego, California, 1989.

[4] A. Bar-Lev, "Semiconductors and Electronic Devices", 2nd ed. Prentice-Hall, Englewood Cliffs, New Jersey, 1984.

[5] G. K. Teal, Single crystals of germanium and silicon – Basic to the transistor and integrated circuit. IEEE *Trans. Electron Devices ED-23 (1976) 621.*

[6] S. Wolf and R.N. Tauber, "Silicon Processing for the VLSI Era", Vol. 1, Lattice Press, Sunset Beach, California, 1986.

[7] N. Motta, Self-assembling and ordering of Ge/Si(111) quantum dots: scanning microscopy probe studies. *J. Phys.: Condens. Matter 14 (2002) 8353.*

[8] J.R. Arthur, Molecular Beam Epitaxy. *Surface Science 50 (2002) 189* .

[9] B. Meyerson, UHV/CVD Growth of Si and Si:Ge Alloys: Chemistry, Physics and Device *Applications. Proc. of the IEEE 80, (1992) 1592.*

[10] H. Rauscher, The interaction of silanes with silicon single crystal surfaces: microscopic processes and structures. *Surface Science Report*s *42 (2001) 207.*

[11] J. Braun, M. Haupt, K. Thonke, R. Sauer, H. Rauscher and R.J. Behm, Irradiation-induced Ge multilayer growth from GeH_4 on Si(111). *Surf. Sci., 454-456 (2000) 811.*

[12] J. Braun, PhD Thesis 2001 : Untersuchungen zum CVD-Wachstum von Silizium und Germanium auf Si(111).

[13] H. Rauscher, J. Braun, & R.J. Behm, Si_xGe_{1-x} ultrahigh-vacuum chemical vapour deposition on Si(111)-7×7 from GeH_4/Si_2H_6 mixtures. *Appl. Phys. A. 76 (2003) 711.*

[14] M. Holz. Diplom Thesis 2002 : Untersuchungen zur Gasphasenepitaxie von dünnen Si/Ge – Schichten auf Si(111)-(7×7).

[15] G.A. Samorjai, Introduction to Surface Chemistry and Catalysis. Wiley Interscience, (1994).

[16] C.B. Duke, Semiconductor Surface Reconstruction: The structural Chemistry of Two-Dimensional Surface Compounds. *Chem. Rev. (1996) 96, 1237.*

[17] G.P. Srivastava, Theory of semiconductor surface reconstruction. *Rep. Prog. Phys. 60 (1997) 561.*

[18] W. Mönch, *Semiconductor Surfaces and Interfaces,* 2nd ed., Springer Series in Surface Sciences, Springer Verlag, Berlin, Vol 26 (1995) .

[19] K. Takayanagi, Y. Tanishiro, S. Takahashi, M. Takahashi, Structure analysis of Si(111)-7 × 7 reconstructed surface by transmission electron diffraction. *Surf. Sci. 164 (1985) 367.*

[20] M. Needels, Comment on ``Ab initio total-energy calculations for extremely large systems: Application to the Takayanagi reconstruction of Si(111). *Phys. Rev. Lett. 1993, 71, 3612.*

[21] I. Stich, C.M. Payne, R.D. King-Smith, J.S. Lin, L.J. Clarke, K.D. Brommer, J.D. Joannopoulos and B.E. Larson, Ab Initio total-energy calculations for extremely large systems: Application to the Takayanagi reconstruction of Si(111). *Phys. Rev. Lett. 71 (1993) 3613.*

[22] E. Baur, Phenomenological theory of crystal precipitation on surfaces. *Z. Kristallogr. 110 (1958) 372.*

[23] F.C. Frank and J.H. van der Merwe, One-dimensional dislocations I Static Theory. *Proc. Roy. Soc. London A 198 (1949) 205.* F.C. Frank and J.H. van der Merwe, One-dimensional dislocations II. Misfitting monolayers and oriented overgrowth. *Proc. Roy. Soc. 200 (1949) 125.*

[24] M. Vollmer and A. Weber, Keimbildung in übersättigten Gebilden. *Z. Phys. Chem. 119 (1926) 277.*

[25] I.N. Stranski and L. Krastanov, Zur Theorie der orientierten Ausscheidung von ionenkristallen aufeinander. *Akad. Wiss. Lit. Mainz Math.-Natur Kl. Iib 146 (1939) 797.*

[26] C.E. Morosanu, Thin Films by Chemical Vapour Deposition, Thin Films Science and Technology 7, 1990, Elsevier.

[27] J.W. Matthews, Accommodation of misfit across the interface between single-crystal films of various face-centered cubic metals. *Philos Mag. 13 (1966) 1207.*

[28] D.W. Pashley, M.J. Stowell, M.H. Jacobs and T.J. Law, *Philos. Mag. 10 (1964) 127.*

[29] B. Elman, E.S. Koteles, P. Melman, C. Jagannath, J. Lee and D. Dugger, In situ measurements of critical layer thickness and studies of InGaAs quantum wells grown on GaAs substrates. *Appl. Phys. Lett. 55 (1989) 1659.*

[30] B. Voigtländer, Fundamental processes in Si/Si and Ge/Si epitaxy studied by scanning tunneling microscopy during growth. *Surf. Sci. Rep. 43 (2001) 127.*

[31] J.H.G. Owen, K. Miki, C.M. Goringe and I. Goldfarb, Gas-source growth of group IV semiconductors: II. Growth regimes and the effect of hydrogen. *Surf. Sci. 394 (1997) 91.*

[32] I. Goldfarb, J.H.G. Owen, P.T. Hayden, D.R. Bowler, K. Miki and G.A.D. Briggs, Gas-source growth of group IV semiconductors: III. Nucleation and growth of Ge/Si(001). *Surf. Sci. 394 (1997) 105.*

[33] M. Tomitori, K. Watanabe, M. Kobayashi and O. Nishikawa, STM study of the Ge growth mode on Si(001). *Appl. Surf. Sci. 76-77 (1994) 328.*

[34] J. Wintterlin and Ph. Avouris, Scanning tunneling microscopy (STM) studies of chemical vapour deposition of Ge on Si(111) from Ge hydrides and a comparison with molecular beam epitaxy. *J. Chem. Phys. 100 (1994) 687-704.*

[35] T.I. Kamins, G. Medeiros-Ribeiro, D.A.A. Ohkberg and R.S. Williams, Evolution of Ge islands on Si(001) during annealing. *J. Appl. Phys. 85 (1999) 1159.*

[36] P.M. Garone, J.C. Sturm and P.V. Schwartz, Silicon vapor phase epitaxial growth catalysis by the presence of germane. *Appl. Phys. Lett. 56 (1990) 1275.*

[37] K.J. Kim, M. Suemitsu, M Yamanaka and N. Miyamoto, Effects of mixing germane in silane gas-source molecular beam epitaxy. *Appl. Phys. Lett. 62 (1993) 3461*.

[38] S.M. Jang and R. Reif, Temperature dependence of $Si_{1-x}Ge_x$ epitaxial growth using low pressure chemical vapor deposition. *Appl. Phys. Lett. 59 (1991) 3162.*

[39] S.M. Jang and R. Reif, Effects of hydrogen and deposition pressure on $Si_{1-x}Ge_x$ growth rate. *Appl. Phys. Lett. 60 (1992) 707.*

[40] D.J. Robbins, J.L. Glasper, A.G. Cullis and W.Y. Leong, A model for heterogeneous growth of $Si_{1-x}Ge_x$ films from hydrides. *J. Appl. Phys. 69 (1991) 3729* .

[41] R. Malik, E. Gulari, S.H. Li. And P. Bhattacharya, Modeling growth of $Si_{1-x}Ge_x$ epitaxial films from disilane and germane. *J. Appl. Phys. 73 (1993) 5193* .

[42] K.Y. Suh, H.H. Lee, Ge composition in $Si_{1-x}Ge_x$ films grown from SiH_2Cl_2/GeH_4 precursors. *J. Appl. Phys. 88 (2000) 4044.*

[43] D. Briggs and M.P. Seah, Practical Surface Analysis, Vol. 1 Auger and X-ray Photoelectron Spectroscopy. 2nd Ed. (1996) Wiley

[44] K. Yates, A. Barrie and F.J. Street, A double-anode X-ray source for photoelectron spectroscopy. *J. Phys. E: Sci. Inst. 6 (1973)130.*

[45] J.E. Castle and A.M. Salvi, The Characterization and use of intrinsic background in XPS. *Analy. Sci. 17 (2001) il47.*

[46] P.W. Atkins, Physical Chemistry. 6th Ed. Wiley.

[47] R. Wiesendanger, Scanning Probe Microscopy and Spectroscopy. Cambridge University Press 1994.

[48] J. Tersoff and D. R. Hamann, Theory and Application for the Scanning Tunneling Microscope. *Phys. Rev. Lett. 50 (1983) 1998.*

[49) J. Tersoff and D. R. Hamann, Theory of the scanning tunneling microscope. *Phys. Rev. B 31 (1985) 805.*

[50] J. Bardeen, Tunnelling from a Many-Particle Point of View. *Phys. Rev. Lett 6 (1961) 57.*

[51] D. Drakova, Theoretical modelling of scanning tunneling microscopy, scanning tunnelling spectroscopy and atomic force microscopy. *Rep. Prog. Phys. 64 (2001) 205.*

[52] H. Neddermeyer, Scanning tunnelling microscopy of semiconductor surfaces. *Rep. Prog. Phys. 59 (1996) 701.*

[53] J.A. Kubby and J.J. Boland, Scanning tunnelling microscopy of semiconductor surfaces. *Surf. Sci. Rep. 26 (1996) 61.*

[54] G. Binnig, H. Rohrer, Ch. Gerber, and E. Weibel, 7×7 Reconstruction on Si(111) Resolved in Real Space. *Phys. Rev. Lett. 50 (1983) 120.*

[55] R. J. Hamers, R. M. Tromp, and J. E. Demuth, Surface Electronic Structure of Si (111)-(7×7) Resolved in Real Space. *Phys. Rev. Lett. 56 (1986) 1972.*

[56] K. Takayanagi, Y. Tanishiro, S. Takahashi, M. Takahashi, Structural analysis of Si(111)-(7×7) by UHV-transmission electron diffraction and microscopy. *J. Vac. Sci. Technol. A 3 (1985) 1502.*

[57] K. Besocke, An easily operable scanning tunneling microscope. *Surf. Sci. 181 (1987) 145.*

[58] J. Frohn, J.F. Wolf, K. Besocke and Teske, Coarse Tipp distance and positioner for a scanning tunneling microscope. *Rev. Sci. Instrum. 60 (1989) 1200.*

[59] N. Petaya, K.-F. Braun and K.-H Rieder, On the stability of Besocke-type scanners. *Rev. Sci. Instrum. 75 (2004) 2608.*

[60] K. Prabhakarana, T. Ogino, R. Hull, J.C. Bean and L.J. Peticolas, An efficient method for cleaning Ge(100) surface. *Surface Science 316 (1994) L1031.*

[61] D.A. Shirley, High-Resolution X-Ray Photoemission Spectrum of the Valence Bands of Gold. *Phys. Rev. B 5(12) (1972) 4709.*

[62] J.E. Castle and A.M. Salvi, Interpretation of the Shirley background in x-ray photoelectron spectroscopy analysis. *J. Vac. Sci. Technol. A 19(4) (2001) 1170.*

[63] N. Motta, A. Sgarlata, R. Calarco, Q. Nguyen, J. Castro Cal, F. Patella, A. Balzarotti, M. De Crescenzi, Growth of Ge-Si(111) epitaxial layers : intermixing, strain relaxation and island formation. *Surf. Sci. 406 (1998) 254.*

[64] G. Capellini, N. Motta, A. Sgarlata, R. Calarco, Evolution of Strained Ge islands grown on Si(111): a scanning probe microscopy study. *S.S. Comm. 112 (1999) 145.*

[65] H.-J. Gossmann, J.C. Bean, L.C. Feldman, E.G. McRae and I.K. Robinson, 7×7 Reconstruction of Ge(111) Surfaces under Compressive Strain. *Phys. Rev. Lett. 55 (1985) 1106.*

[66] H.-J. Gossmann, J.C. Bean, L.C. Feldman, E.G. McRae and I.K. Robinson, Summary Abstract : Observation and Properties of the Ge(111)-7×7 surface from Si(111)/Ge structures. *J. Vac. Technol. A 3 (1985) 1633.*

[67] V. Cherepanov, B. Voigtländer, Influence of strain on diffusion at Ge(111) surfaces. *Appl. Phys. Lett. 81(25) (2002) 4745.*

[68] F.K. LeGouges, M. Hammer, M.C. Reuter, R.M. Tromp, In situ TEM study of the growth of Ge on Si(111). *Surf. Sci. 349 (1996) 249.*

[69] S.A. Chaparro, Y. Zhang, J. Drucker, Strain relief via trench formation in Ge/Si(100) islands. *Appl. Phys. Lett. 76(24) (2000) 3534.*

[70] U. Denker, O.G. Schmidt, N.Y. Jin-Philipp, K. Eberl, Trench formation around and between self-assembled Ge islands on Si. *Appl. Phys. Lett. 78(23) (2001) 3723.*

[71] X.Z. Liao, J. Zou, D.J.H. Cockayne, J. Wan, Z.M. Jiang, G. Jin, K.L. Wang, Alloying, elemental enrichment and interdiffusion during the growth of Ge(Si)/Si(001) quantum dots. *Phys. Rev. B 65 (2002) 153306-1.*

[72] F. Boscherini, G. Capellini, L. Di Gaspare, F. Rosei, N. Motta, S. Mobilio, Ge-Si intermixing in Ge quantum dots on Si(001) and Si(111). *App. Phys. Lett. 76 (2000) 682.*

[73] J. Zou, X.Z. Liao, D.J.H. Cockayne, Z.M. Jiang, Strain relaxation in self-assembled Ge(Si)/Si quantum dots, Presentated at 8th International Conference on Electronic Materials (IUMRS-ICEM 2002, Xi'an China 10-14 June 2002).

[74] T.I. Kamins, E.C. Carr, R.S. Williams, S.J. Rosner, Deposition of three-dimensional Ge islands on Si(001) by chemical vapour deposition at atmospheric and reduced pressures. *J. Appl. Phys. 81 (1997) 211.*

[75] M. Himmerlich, W. Yang, R.J. Nemanich, J.A. Schaefer, Growth Dynamics of Ge islands on high index Si Surfaces, Presented at Frühjarstagungs der DPG, Regensburg 2004.

[76] A.L. Barabasi, Self-assembled island formation in heteroepitaxial growth. *Appl. Phys. Lett. 70 (1997) 2565.*

[77] F.K. LeGouges, M.C. Reuter, J. Tersoff, M. Hammer, R.M. Tromp, Cyclic Growth of Strain-Relaxed Islands. *Phys. Rev.Lett. 73 (1994) 300.*

[78] J. Tersoff, Enhanced Nucleation and Enrichment of Strained-Alloy Quantum Dots. *Phys. Rev.Lett. 81 (1998) 3183.*

[79] B.J. Spencer, J. Tersoff, Stresses and first-order dislocation energetics in equilibrium Stranski-Krastanov islands. *Phys. Rev. B 63 (2001) 205424-1.*

[80] J. Tersoff, Instability Wavelength in Strained-Alloy Epitaxy *Phys. Rev.Lett. 85 (2000) 2843.*

[81] R.W. Price, E.S. Tok, N.J. Woods and J. Zhang, Growth dynamics of $Si_{1-y}C_y$ and $Si_{1-x-y}Ge_xC_y$ on Si(001) surface from disilane, germane and methylsilane. *Appl. Phys. Lett. 81 (2002) 3780.*

[82] K. Kanzawa, N. Nozawa, T. Saitoh and M. Kubo, Dependence of substituitional C incorporation on Ge content for $Si_{1-x-y}Ge_xC_y$ crystals grown by ultrahigh vacuum chemical vapor deposition. *Appl. Phys. Lett. 77 (2000) 3962.*

[83] G.D Watkins and K.L. Brower, EPR Observation of the Isolated Interstitial Carbon Atom in Silicon. *Phys. Rev. Letts. 36 (1976) 1329.*

[84] L.W. Song, X.D. Zhan, B.W. Benson and G.D. Watkins, Bistable interstitial-carbon–substitutional-carbon pair in silicon. *Phy. Rev. B, 42 (1990) 5765.*

[85] R.B. Capaz, A. Dal Pino Jr. And J.D. Joannopoulos, Identification of the migration path of intersitial carbon in silicon. *Phys. Rev. B 50 (1994) 7439.*

[86] P. Leary and R. Jones, S. Öberg and V.J.B. Torres, Dynamic properties of intersitial carbon and carcon-carbon pair defects in silicon. *Phys. Rev. B 55 (1997) 2188.*

[87] E.V. Lavrov, L. Hoffmann and B. Bech Nielsen, Local vibrational modes of the metastable dicarbon center (C_s-C_i) in silicon. *Phys. Rev. B 60 (1999) 8081.*

[88] R. Sauer. *Photoluminescence properties of impurities and defects, in: M. Schultz (Ed), Impurities and defects in group IV elements and III-V compounds, Landolt-Börnstein New Series, Group III, Vol. 22b, p. 338, chapter 4.2.5 . Springer, Berlin, 1989.*

[89] J. Weber and M. Singh, New method to determine the carbon concentration in silicon. *Appl. Phys. Lett. 49 (23) (1986) 1617.*

[90] R. Sauer, J. Weber and J. Stolz, Dislocation-Related Photoluminescence in Silicon. *Appl. Phys. A 36 (1985) 1.*

[91] S. Gopalakrishnan, F. Banhardt, H. Rauscher and R.J. Behm, An STM, AFM and TEM study of Ge 3D structures grown by CVD on Si(111) –(7×7). In preparation.

[92] K. Seemann, Studienarbeit 2003: Determination of the Mechanism of X-radiation induced 3D Growth of CVD Deposited Ge on Si(111)-7×7 using Atomic Force Microscopy and Scanning Tunneling Microscopy.

[93] S. Gopalakrishnan and K. Seemann,
H. Rauscher, and R.J. Behm**,** Identification of causes of X-ray induced 3D growth of Ge on Si(111)-7×7. In Preparation.

[94] Mass Attenuation Coeffcients – Table 1,
http:// physics.nist.gov/PhysRefData/XrayMassCoef/chap2.html

[95] J.Braun. H. Rauscher and R.J. Behm, Mechanism of GeH_4 dissociation on Si(111)-7×7. *Surf. Sci 531 (2003) 265.*

[96] P. Bratu and U. Höfer, Phonon-Assisted Sticking of Molecular Hydrogen on Si(111)-7×7. *Phys. Rev. Letts. 74 (1995) 1625.*

[97] P. Bratu, W. Brenig, A. Groß, M. Hartmann, U. Höfer, P. Kratzer and R. Russ, Reaction dynamics of molecular hydrogen on silicon surfaces. *Phy. Rev. B, 54 (1996) 5978.*

[98] L. Surnev and M. Tikhov, Comparative study of hydrogen adsorption on Ge(100) and Ge(111) surfaces. *Surf. Sci. 138 (1984) 40.*

[99] G. Schulze and M. Henzler, Adsorption of atomic hydrogen on clean cleaved silicon (111). *Surf. Sci. 124 (1983) 336.*

[100] J.W. Sharp and G. Eres, Kinetics of hydrogen desorption in surface-limited thin-film growth of SiGe alloys. *Appl. Phys. Lett. 62 (1993) 2807.*

[101] K, Sinniah, M.G. Shermann, L.B. Lewis, W.H. Weinberg, J.T. Yates, Jt., and K.C. Janda. *Phys. Rev. Lett. 62 (1989) 567.*

[102] T. Hager, STM to Statistics : Installation and Handling of FSTM, XVSTM, IDL. Version 1.0 Dec. 2002.

[103] Millenias IPGC Ionization Gauge Instruction Manual

[104] MKS Spinning Rotor Gauge Instruction Manual

[105] MKS Baratron Instruction Manual

Appendix 1

Computer Controlled Reconstruction and STM Data Conversion

1.1 Computer Controlled Reconstruction

In order to ensure that the Si(111)-(7×7) has a surface which is nearly defect free and to obtain a nearly reproducible surface for every deposition in terms of defect counts, a PCI 6024 E computer interface card from National Instruments has been newly installed for this work and a program has been written to automatically control the flash and reconstruction cycle.

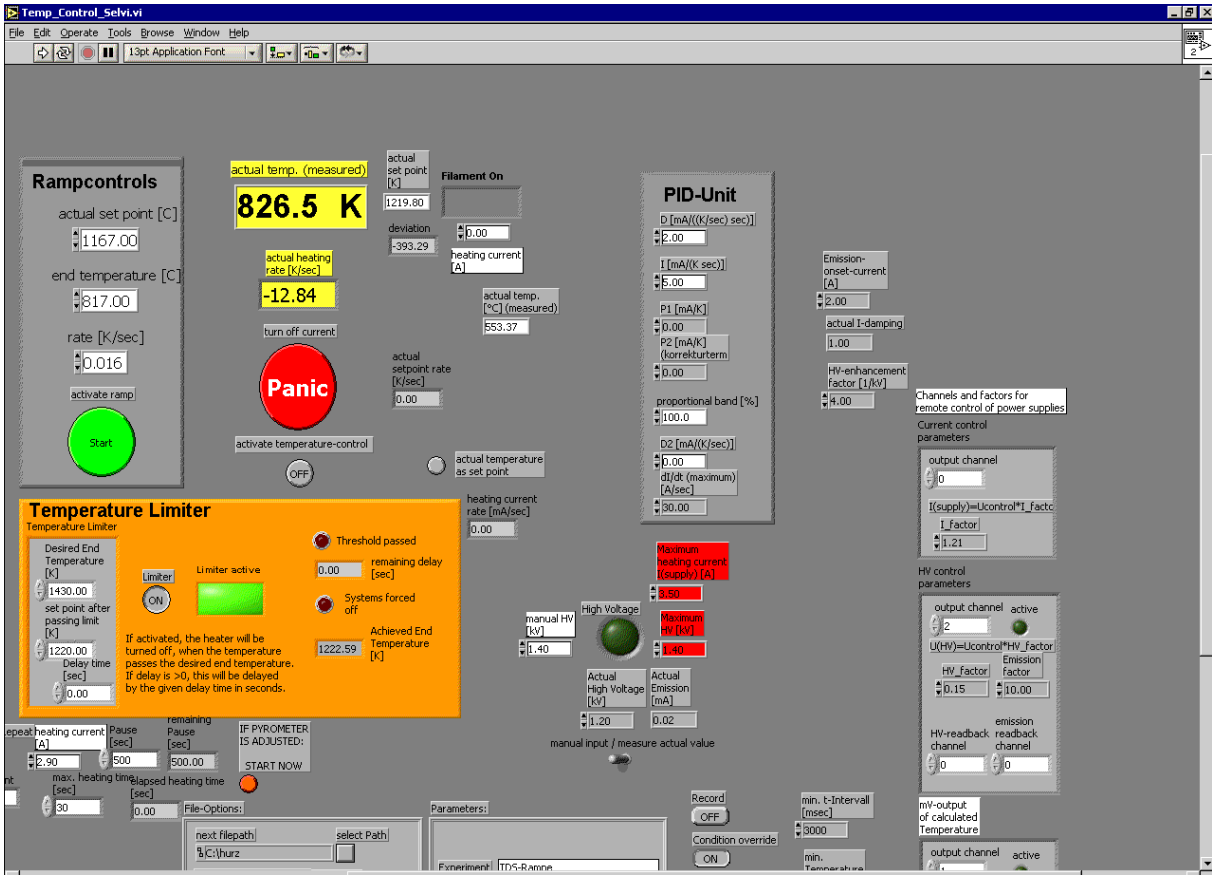

Fig. 1.1 : Initial Window of Temp_Control_Selvi.vi

The program to control the reconstruction cycle is written in Labview Version 6.1 by Dr. H. Hoster and has been saved under the name, **Temp_Control_Selvi.vi.**

Once the optical pyrometer and the computer controls to the power supply connection have been set up and connected, the program **Temp_Control_Selvi.vi** is clicked open under the **`open.vi`** menu in Labview and the screen as in Fig. 1.1. To start the program, the small red button at the top of the Menu bar has to be pressed.

To carry out the short flashes to remove the surface impurities such as oxides, the temperature limit at the **Temperature Limiter** which is located at the middle left of the window is set to 1220 K and the **limiter** button is set to **ON**. The green **Start** button at the **Rampcontrols** is then to be pressed. The program then causes the substrate to be rapidly heated up to 1430 K. As soon as the temperature reading at the **actual temp. (measured)** display reaches 1430 K, the red **Panic** button must be pressed immediately. The **limiter** button is then reset to **ON** and the **actual set point (^{o}C)** to **1167 ^{o}C** for the next flash sequence. The flashing procedure is to be re-commenced once the substrate has cooled down to 826 K and is to be repeated until there is no appreciable pressure (immediately after flashing) increase as measured by the ionisation gauge. This usually takes between 10 to 15 short flashes.

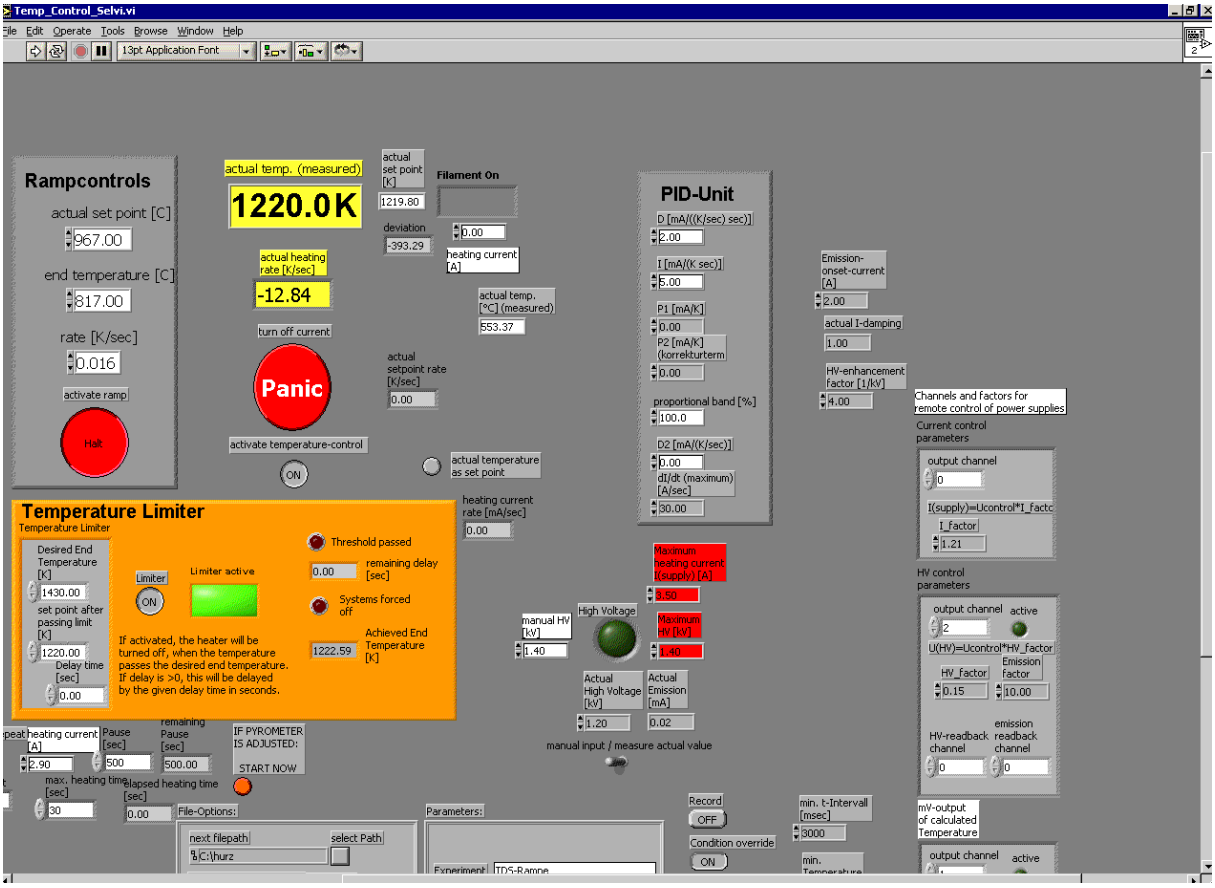

Fig. 1.2: Final Countdown window of Temp_Control_Selvi.vi

For the reconstruction step, the temperature limit in the **Temperature Limiter** is set to 1220 K. Once the green **Start** button at the **Rampcontrols** is pressed, the program is directed to rapidly heat the substrate up to a temperature of 1430 K but cut the heating ramp once this temperature is reached such that the sample cools down rapidly until it reaches a temperature of 1220 K. Once a temperature of 1220 K is reached, the green **Start** button at the **Rampcontrols** is again pressed whereby the slow cooling ramp of 1 K/min is initiated as shown in Fig. 1.2. The program ends once the lower set limit of 1100 K is reached. Once this

temperature is reached, the red **Panic** button must be pressed in order to ensure a rapid cool down to room temperature.

1.2 STM Data Conversion

The STM images are collected in the DOS mode using the FSTM software. The raw data files are then converted to **pgm** files in the Linux mode using the XVSTM software as described in Ref. [102].

The actual STM images processing and calculation of coverages and heights is carried out in **IDL31**. As **IDL** uses a different file format (**spd**) the **pgm** files are converted to **spd** files using the file converter option in **IDL**[102].

Appendix 2

Vacuum Requirements and Pressure Measurements

1.0 Pumps for UHV Requirements

1.1 Introduction

As the starting point for the all the work carried out here, is an atomically clean substrate surface, ultra high vacuum (UHV) conditions of pressures less than 10^{-9} mbar or better are required to maintain a 'contamination' free (< 1% of a monolayer) surface for the duration of the experiments. This is achieved by a combination of the pumps. A mechanical pre-pump is used to bring the system from atmosphere to pre-vacuum and to pump away ejected gases into the exhaust . The combination of the diffusion pump, turbomolecular pump, ion pump and the titanium sublimation pump (TSP) is then used to achieve UHV conditions of 10^{-10} mbar or better.

1.2 Diffusion pump

The diffusion pump[43] can be operated over a wide range of vacuum conditions. It is designed to work with fluids which have a vapour pressure at room temperature in the range of 10^{-10} mbar and which have a high resistance to degrade into volatile components. The fluid used in this pump is a perfluoro ether. In this type of pump, the fluid, at the base of the pump is heated externally and the resulting vapour passes up through the central structure of the pump. The pump is designed such that the vapour exits at supersonic velocities at three escape jets. These jets are directed such that the vapours issuing from then traverse in a downard direction towards the bottom of the pump. The pump is cooled by water such that the vapour is condensed soon after it emerges from the jets. When the molecules in the vapour strike other gas molecules, they impart their high kinetic energy to these gas molecules. Most of the imparted energy is directed in the direction through which the vapour molecules have been travelling before impact, which is downwards towards the pump. Hence, the gas molecules are effectively swept to the exit port at the lower part of the pump, where they are pumped off by the mechanical pre-pump. The main advantage of the diffusion pump is that it is able to pump any gas, as long as it does not react with the fluid used.

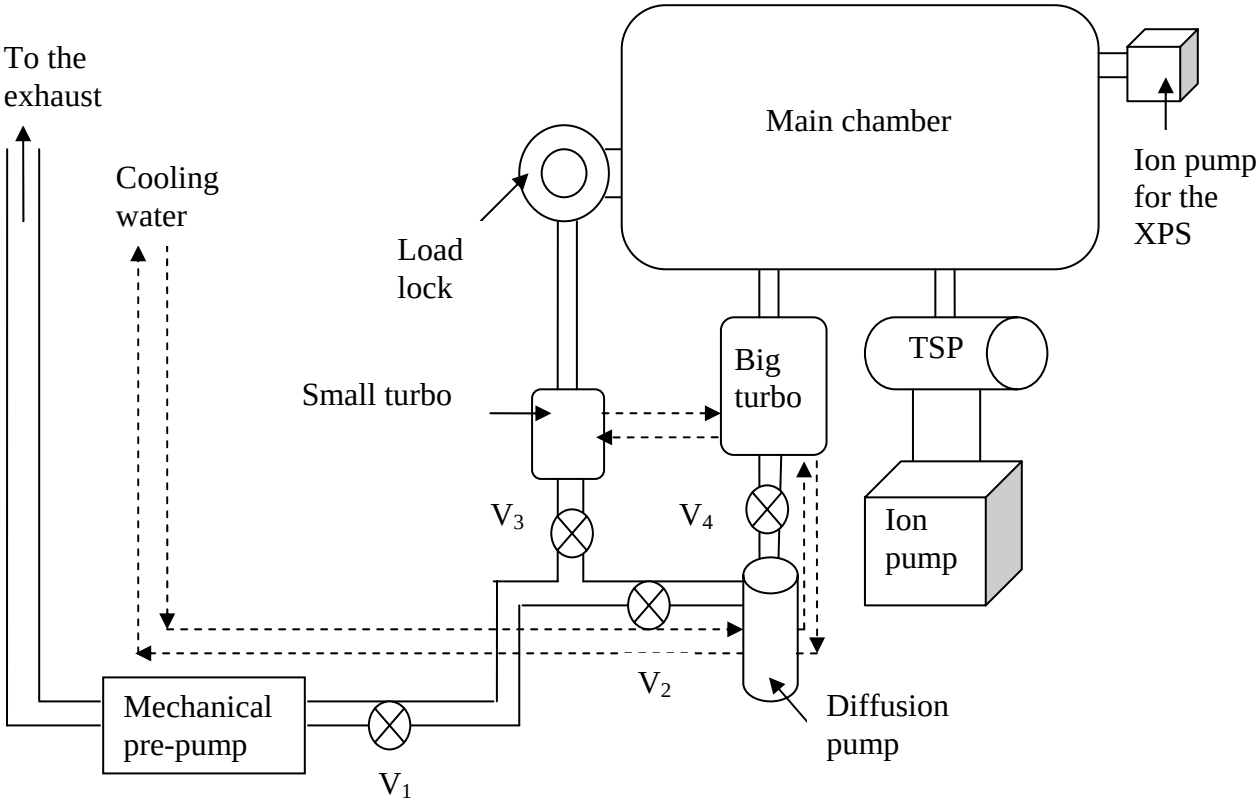

Fig. 1.1 : Schematic diagram of the pumping system of the STM V

Hence, it is effective in efficient removal of hydrogen which is otherwise difficult to remove with a turbomolecular pump. As the precursor gases for the CVD work in this study are hydrated species, it is imperative that the hydrogen which is a by-product of the CVD process be efficiently removed.

The disadvantages with the use of this pump are that a special fluid is needed for the operation of this pump and that it can only be operated in the vertical position.

1.3 Turbomolecular pump

The main components of a turbomolecular pump[43] are the rotor and a stator which are two sets of precisely shaped and machined circular blades, with the set of rotor blades fitting into the set of stator blades. The motor of the pump which is water cooled, enabling the rotor to rotate at very high speeds in the 20 000 to 50 000 rpm range. Any gas molecules striking the rotor blades gain large increases of velocity in the direction of the rotating blades. Due to the design and arrangement of the blades in the pump, the molecules are repeatedly driven in the downward direction, towards the exit from the pump. In the STM V system, the ejected gases are pumped out to the exhaust via the diffusion pump and the mechanical pre-pump.

As the kinetic energy is a function of the mass of a molecule, the heavier gas molecules are pumped more efficiently than ligher molecules. Hence hydrogen is not pumped out efficiently

by the turbomolecular pump. Therefore in this system the diffusion pump has been used in series with the turbomolecular pump.

1.4 Ion pump

The ion pump[43], like the diffusion pumps can be used over a wide range of vacuum conditions. Their advantages are that unlike the diffusion pump, they do not require cooling water and do not use special fluids. They can be connected directly to the chamber without the requirements for any traps and theoretically can be mounted in any orientation. Their main disadvantage is that because of the operational principles, they cannot remove hydrogen or low molecular weight gaseous hydrocarbons. However these species are efficiently pumped by the diffusion pump. A more serious disadvantage is the memory effect associated with this type of pump since the gas is trapped in the pump and is pumped out of the system via the exhaust. These pumps also have strong magnetic fields, need high voltages (about 7 kV in this system) and tend to be very heavy because of the large magnets in the larger pumps. As high voltages are associated with these pumps they can only be switched on once an operational vacuum is achieved.

This pump consists of an anode which is a honeycombed structure made up of many cells, and a cathode. The cathode, which is made of titanium, is usually fixed to the wall of the pump and is earthed, while a high positive voltage is applied at the anode. A strong magnetic field is applied across these two electrodes. When the pressure in the pump is low enough (about 10^{-4} mbar), the combined effects of the high voltage and the magnetic field cause a discharge to be set up in the anode. This causes the gas molecules in the system to be ionized. The gradient in the electrostatic field causes these ionized species to move towards the cathode which they strike with high energy, causing sputtering. As titanium is a highly reactive metal the sputtered titanium ion or clusters react with the gas molecules to form involatile titanium compounds, hence removing them from the system. However as the noble gases do not react with titanium, they are pumped by burial underneath the condensing titanium atoms or clusters. Hydrogen is pumped by dissolution of titanium which leads to the formation of a range of hydrides. These can reappear by diffusion and hence escape to and from the surface. Hence the main component in a system pumped by ion pumps is usually hydrogen.

1.5 Titanium sublimation pump (TSP)

The TSP[43] acts in conjunction with the other pumps described above. It is usually operated under UHV conditions, although it can be operated in higher pressures of up to 10^{-6} mbar. If the normal base pressure of the system is 10^{-10} mbar, with regular use of a well degassed TSP, pressures in the range of 10^{-11} mbar can be achieved.

The TSP consists of three filaments made of titanium or a titanium alloy. A voltage source is connected to one of these filaments. When a current (about 40 A) passes through this filament, it causes the filament to heat to the point at which the titanium sublimes. The sublimate combines with the active gases in the system. The titanium clusters thus formed are pumped by condensing on a cooled surface.

2.0 Pressure Measurements

2.1 Introduction

The STM V uses different type of gauges for the various pressure measurements. Two ion gauges, one in the load lock and the other in the main chamber are used to monitor the pressures in the respective chambers. In addition, the ion gauge in the main chamber is used to monitor the flux of the CVD precursor gases for deposition pressures in the low pressure range (10^{-9} to 10^{-6} mbar range). For deposition in the 10^{-5} mbar range, a spinning rotor gauge is used. A baratron is used to control the gas ratios for mixed gas CVD.

2.2 Ionization Gauge

This is the typical type of gauge used for pressure measurements in UHV. It is also known as the Bayard-Alpert ionization gauge[103]. It consists (of two spirals of thoria coated iridium filaments, (one of which is a spare when the other is burnt out) mounted on a circular support. A grid (anode) is mounted the two filaments. The filaments and the grid are set at a potential difference of 150 V. A collector wire, set at -40 V is mounted at the centre. When the ion gauge is in use, the electrons from on the filament which is heated are accelerated towards the grid. At the grid, these electrons ionize any gas molecules which are contained within the volume of the grid (anode). As these are positively charged, they are attracted towards the collector. The current of these positive ions is directly proportional to the pressure of the molecules, within the anode.

$$\mathbf{I_+ = I_e \,.\, S \,.\, p}$$

where I_+ is the current of positive ions
I_e is the emission current (electrons)
S is the gauge sensitivity and
p is the pressure

As I_e and S are set constants, the pressure in the system is obtained from the I_+.

This gauge has a higher operating limit of 10^{-3} mbars, where there is high probability of the generation of multiple ions per electrons and filament burnout and a lower operating (X-Ray limit) limit of 10^{-11} mbar. This limit is set by the low current induced by the ejection of photoelectrons from the collector. These result from the bombardment of the soft X-rays produced when electrons strike the anode or the supports.

From the above equation, it can be seen that as the pressure is dependent on I_+, and hence on the type of gas present in the system. Hence in order to use the ion gauge to measure the gas flux during CVD, the pressure readout has to be multiplied by a gas calibration factor (Table 2.1) , to obtain the true pressure :

True gas pressure = pressure reading at ion gauge x gas calibration factor

Gas	calibration factors
Nitrogen	1.0
Oxygen	0.94
Hygrogen	3.1
Carbon dioxide	0.71
Carbon monoxide	0.9
Methane	0.71

Table 2.1 : Some gas calibration factors for the ionization gauge

2.3 Spinning Rotor Gauge (SRG)

The Spinning rotor gauge[104] or SRG is used for CVD experiments in the lower pressure range. This type of gauge is accurate in the 10^{-2} to 10^{-6} mbar range.

The main component of the SRG is the sensing unit which is connected to the UHV system. The sensing unit contains a magnetically levitated stainless steel ball. This ball is suspended and rotated by an external electronics. When in operation the external electronics bring the ball up to a certain rotational speed, after which the ball is allowed to rotate freely. The gas molecules in the UHV system collide with the stainless steel ball causing a deceleration in its rotational speed. The sensing coils inside the unit measure this deceleration which is used to calculate the pressure inside the UHV system using an algorithm which takes into account the sampling time and the calibration factors for the gases present in the system. The calibration of the system is carried out by a preset program prior to commencement of any CVD experiments. The main disadvantage of the SRG is the relatively slow reponse time to pressure as compared to the ion gauge and the capacitance manometer.

2.4 Capacitance Manometer (MKS Baratron)

The capacitance manometer[105], unlike other pressure gauges such as the ion gauge reads the true pressure of the gas as given by the relation :

$$\text{pressure} = \text{force} \div \text{unit area}$$

The capacitance manometer is essentially a transducer which requires a 15V power supply and operates in the 0 to 10 V range. The heart of the manometer is a sensor capsule (Fig. 2.1) which consists of a diaphram and a ceramic on metal electrode system. The reverse (reference) side of the diaphram is maintained at a very high vacuum by an internal getter pump. The metal diaphram is radially tensioned and has a low hysteresis, ensuring high reproducibility, a fast response and the ability to measure at low pressures. These properties are ideal for the use of the manometer to produce CVD gas mixtures with the required gas ratios.

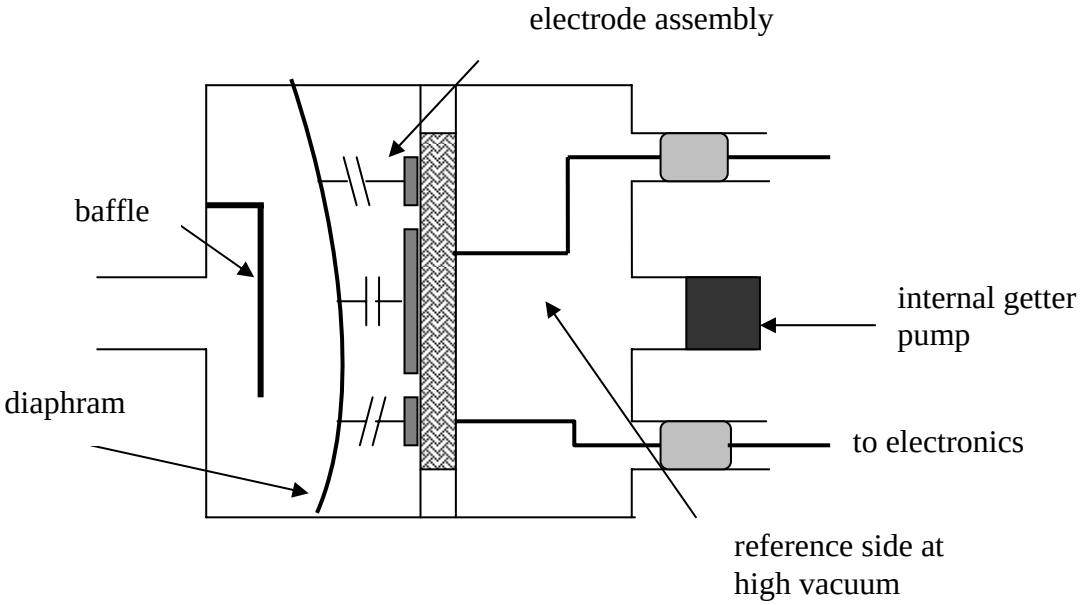

Fig. 2.1 : Capacitance Manometer[15]

Pressure is determined when there is a change in capacitance between the diaphram and the electrode. This produces a signal which is directly proportional to the pressure experienced at the diaphram. The design of the manometer ensures that at high over-pressures the diaphragm flattens out against the surface of the electrode, which prevents any damage to the sensor itself.